The Pennsylvania State University
The Graduate School
College of Engineering

STORED CHEMICAL ENERGY PROPULSION SYSTEM (SCEPS) REACTOR INJECTOR PERFORMANCE PREDICTION MODELING WITH EXPERIMENTAL VALIDATION

A Thesis in
Mechanical Engineering
by
Michael E. Crouse, Jr.

Submitted in Partial Fulfillment
of the Requirements
for the Degree of

Master of Science

December 2017

The thesis of Michael E. Crouse, Jr. was reviewed and approved* by the following:

Laura L. Pauley
Professor of Mechanical Engineering
Thesis Advisor

Stephen P. Lynch
Assistant Professor of Mechanical Engineering

Karen A. Thole
Professor of Mechanical Engineering
Head of the Department of Mechanical and Nuclear Engineering

*Signatures are on file in the Graduate School.

Abstract

A quasi one-dimensional compressible-flow model has been developed to characterize the thermodynamic state of gas injectors within stored chemical energy propulsion systems (SCEPS). SCEPS take the form of a batch reactor with a metal fuel and gaseous oxidant. The result is a high-heat, molten metal bath with a reacting gas jet under vacuum pressure conditions. The developed model incorporates the combined effects of Fanno (frictional) and Rayleigh (heat) flow, including entropic predictions of sonic flow conditions. Constant, converging, and diverging-area, Reynolds-scaled nozzle profiles were exercised to demonstrate the capability of the model in forecasting varied flow regimes that may occur in SCEPS injectors. Physical nozzles, with identical geometric profiles to those of the model cases, were then tested for these nozzle conditions in order that the fidelity of the model could be evaluated. The test results validated the model's static pressure prediction for each nozzle case by producing the same distribution of pressures on the same order of magnitude. The order of temperature values was also validated, although greater divergence from the model predictions occurred toward the latter half of each nozzle. Overall, the model proved to be capable of approximating the same general flow characteristics as those measured in the nozzles of the same case. The model also confirmed that a combined Fanno-Rayleigh entropy curve was instructive in determining sonic flow conditions in each nozzle case. The results of this study demonstrate that the developed model is a feasible tool for fundamental analysis of SCEPS injectors.

Table of Contents

List of Figures

List of Tables

Nomenclature

Alphabetical

A	Cross-section of channel
A_s	Surface area
c_p	Fluid specific heat at constant pressure
D	Diameter
f	Friction factor
h	Convective heat transfer coefficient
k_f	Fluid conductive heat transfer coefficient
L	Channel length
M	Mach Number
$\dot{m}$	Mass flow rate
P	Pressure
Pr	Prandtl Number
q	Heat transfer rate
q"	Heat flux
Re	Reynolds Number
s	Entropy
T	Temperature
V	Channel Mean Velocity
X	Drag force
x	Axial length variable
y	Ratio of forward component of velocity of injected fluid to velocity of fluid

Greek Symbols

ρ	Density
τ_w	Wall shear stress
γ	Ratio of specific heats
ε	Absolute roughness

Subscripts

1	Inlet condition
0	Stagnation properties
j	Iteration identifier
i	Node identifier

Acknowledgements

The author desires to express his genuine gratitude to Dr. Laura Pauley, Professor of Mechanical Engineering and thesis advisor, for her assistance in the final stages of this project. Her guidance in the formal presentation of this research is greatly appreciated. The instruction received from Dr. Stephen Lynch regarding the experimental analysis and presentation of results for this work has been highly valued. And, for the conception and primary assistance for the greater part of this work, a great debt of gratitude is owed to Dr. Timothy Miller. It has been an honor to work with these individuals as it has demonstrated the great quality of the faculty in Mechanical Engineering at the Pennsylvania State University.

The author also wishes to communicate his deep thankfulness for the steadfast support provided by his family. Without their love and encouragement, this accomplishment would not have been possible.

Above all, the author desires to acknowledge his Creator and Savior, the Lord Jesus Christ. It has been the greatest honor to bear His image in this world, while exploring just a small part of His magnificent creation. To Him be the glory, both in this work and in all things, forever.

Thus says the Lord: “Let not the wise man glory in his wisdom, let not the mighty man glory in his might, nor let the rich man glory in his riches; but let him who glories glory in this, that he understands and knows Me, that I am the Lord, exercising lovingkindness, judgement, and righteousness in the earth. For in these I delight,” says the Lord.

~ Jeremiah 9:23-24

Chapter 1. Introduction

1.1 Motivation

Stored chemical energy propulsion systems (SCEPS) surfaced as the leading technology for undersea applications in the latter half of the twentieth century. SCEPS promised many improvements over the current monopropellant propulsion systems of the day; most notably that of a closed-cycle reaction in which the products require less volume than the reactants. Such a system is appropriate for underwater applications, since the reaction has little dependence upon ambient conditions, such as hydrostatic pressure due to submerged distance, whereas monopropellant systems are more dependent upon ambient (exhaust) pressure and experience reduced performance at large operational depths [1].

While monopropellant systems exhaust reaction products from the combustion chamber, SCEPS is a batch reactor in which an oxidizer is injected to react with molten fuel, and the products remain in the reactor. The standard SCEPS reaction involving molten lithium fuel combustion due to injection of gaseous sulfur hexafluoride is given by Equation (1.1).

$$8Li + SF_6 \rightarrow 6LiF + Li_2S + heat \tag{1.1}$$

Both lithium fluoride and lithium sulfide are solid-state products, with the bulk of the generated heat being produced by the exothermic formation of lithium fluoride. This heat is employed by a working fluid (water) to generate steam at high pressure, which then drives a turbine to produce shaft work in the torpedo drivetrain. Monopropellant systems, however, waste a portion of the reaction-generated heat via exhaustion of reaction products. In contrast, SCEPS enables greater utilization of thermal energy in the system. A basic system schematic is demonstrated by Figure 1.

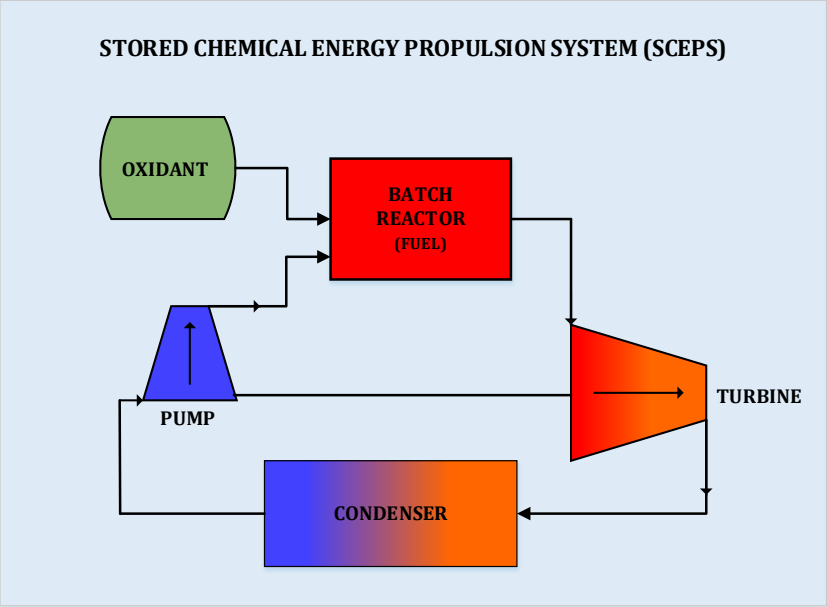

Figure 1: SCEPS System Diagram

Granted SCEPS has functional superiority over monopropellant systems in several underwater applications (such as deep sea diving), new challenges arise due to its dissimilar system configuration. In monopropellant systems, such as those which use Otto Fuel II, combustion is initiated via a fire igniter, and thermodynamic expansion of the reacting gases produces power by expansion in rotary, piston-style engines [3]. In other words, the volume and mass of reactants/products changes significantly during each power cycle. In SCEPS, however, the reactants and products remain in the combustion chamber and form an anisotropic, liquid metal bath. A characterization of the injection flow regime, then, becomes that of a reacting gas jet in a liquid bath, rather than flame propagation of combusting liquid fuel injection with monopropellants. This type of system configuration is displayed in Figure 2.

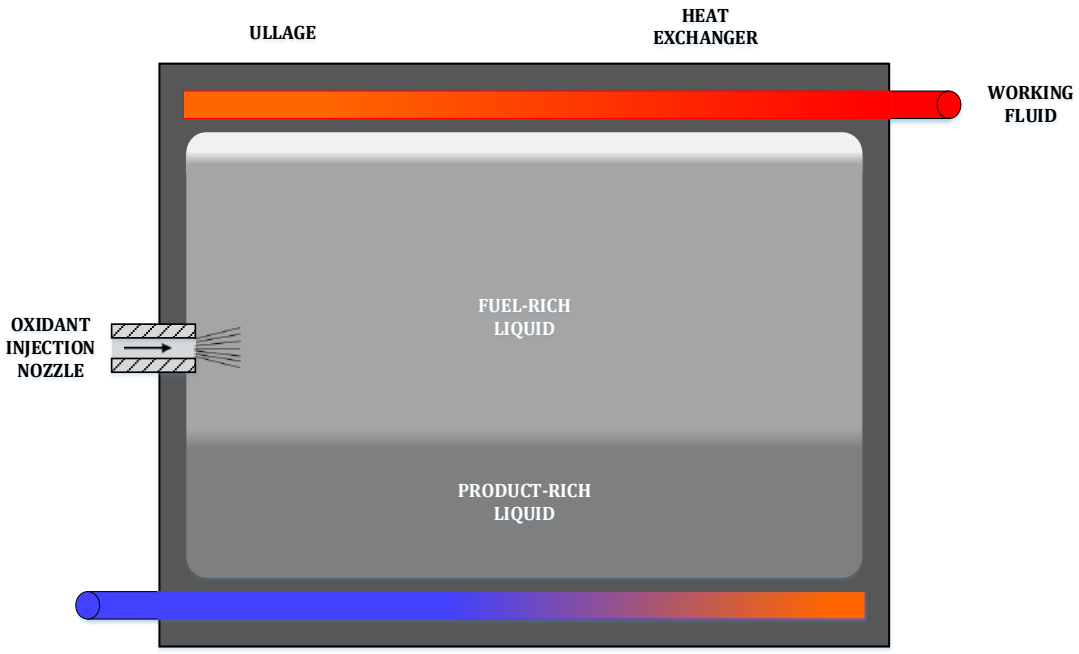

Figure 2: SCEPS Batch Reactor Schematic

With the given combustion configuration in SCEPS, operation of oxidant injectors becomes a critical subject of study, and gaining a better understanding of their performance and impact of design is the main objective of this project. The conditions within the combustion chamber directly impact injector performance, and certain circumstances may even cause malfunction. Due to the complex, transient nature of the combustion reaction, multiple phenomena may occur that can cause degradation of injector operation that eventually lead to failure. The following section provides more detailed descriptions of these phenomena and their resulting impact on injector geometry and performance.

1.2 Problem Description

Gas injection into a liquid bath presents complex physical and chemical formations due to non-uniform mixing of the reactants. Unlike piston-type reactors, where fuel injection may be initiated at consistent chamber pressures, the pressure of the SCEPS combustion chamber is not easily predicted or measured. This is due to the fact that the pressure is dependent upon the rate of chemical reaction which, in turn, is dependent upon the rate of mixing (or turbulence of the gas jet) of the reactants. Since the rate of mixing is not easily determined with precision, the bath pressure is likewise challenging to quantify. Supposing the pressure in the combustion chamber rises above the design back pressure for the injector, reacting products in the bath may wick up into the tungsten injector bore. If this phenomenon takes place, the bore area may be narrowed or plugged by bath material, causing a reduction in the working flow profile. Such an incident radically alters the gas dynamics in the injector, subsequently modifying the mixing conditions of the liquid bath, and negatively affecting system performance.

Another potential event that may lead to injector malfunction is material degradation due to reaction of the oxidant with the bore of the injector. This reaction can take place when the temperature of the injector bore reaches the limit at which sulfur hexafluoride dissociates into sulfur and fluorine ions. This becomes a feasible prospect given that the combustion chamber in SCEPS serves as the heat sink for the exothermic reaction. Since the injectors are mounted directly to the reactor wall, significant amounts of heat may be conducted from the interior of the chamber, through the injector housing, and into the bore. As a result, the incoming sulfur hexafluoride may rapidly heat up to the point of dissociation near the wall of the injector.

As material dissolves from the bore surface, the roughness (friction) may significantly increase, and the resulting flow area will expand. Comparable to the material wicking phenomenon, these

consequential changes alter the gas dynamics of the injected oxidant, and may lead to malfunction or even failure. Therefore, the heat transfer characteristic of the injector module becomes a critical topic of study for determining the occurrence of material degradation.

1.3 Related Work

Study of research that closely relates to the given subject aides understanding of associated challenges and potential solutions. In addition, the resulting analysis of this project may augment such research and lead to improvement of related applications. Similar studies to this project assist the reader in grasping the key components of such research while, in return, the results produced, herein, further the knowledge base of the same area of study.

One such enterprise closely associated to the subject of this thesis is NASA's Generalized Fluid System Simulation Program (GFSSP) [4]. This ongoing program started in 1994 in order to provide a general model solver that could evaluate fluid systems with various characteristics, including compressibility effects. In a technical report prepared by Bandyopadhyay and Mjumdar for the 2007 Thermal Fluid Analysis Workshop (TFAWS) [5], GFSSP was demonstrated by modeling a constant-area nozzle with combined friction and heat transfer effects. This example of GFSSP used the nozzle geometry of Figure 3, which included a constant friction factor, $f = 0.002$, and a uniform heat rate, $Q = 555$ BTU/s.

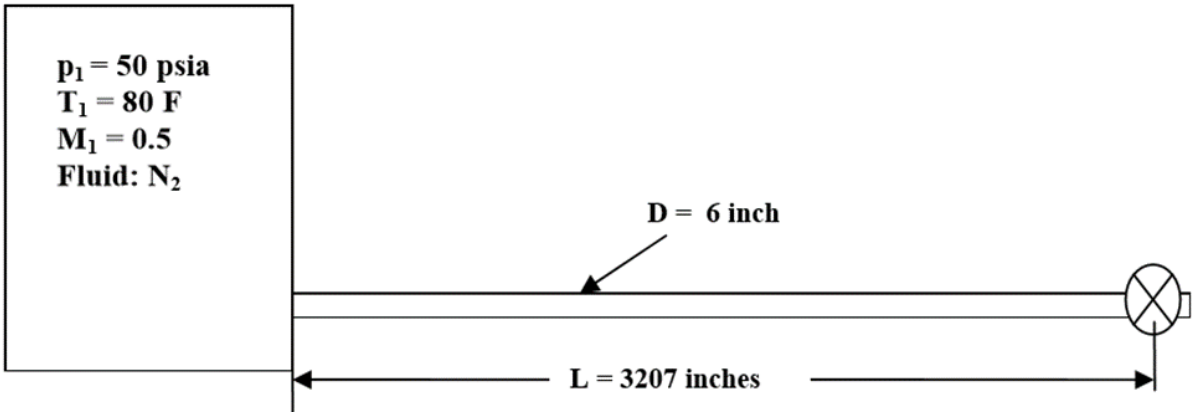

Figure 3: Constant-Area Nozzle Example of GFSSP [5]

The key fluid parameters that were then calculated were the resulting Mach number and static temperatures and pressures through the nozzle. These parameters were then compared to a general numerical solution of the governing gas dynamics equation of the following form:

$$\frac{dM}{dx} = \frac{M\left(1+\frac{\gamma-1}{2}M^2\right)}{(1-M^2)}\left[\gamma M^2 \frac{f}{D} + \frac{(1+\gamma M^2)}{2T_0}\frac{dT_0}{dx} - \gamma M^2 \frac{1}{A}\frac{dA}{dx}\right] \quad (1.2)$$

The general solution of this equation then served as the analytical solution. With the three primary characteristics, a substantial comparison of GFSSP's solution to the analytical solution could be evaluated, and the validity of the program could be established.

The latest update of GFSSP (version 6) was released in 2012, and included a revised demonstration of a converging-diverging (C-D) nozzle simulation [6]. This example focused on determination of the choked mass flow through the nozzle for varying back pressures, and it employed the nozzle geometry given in Figure 4, below. The primary objective of this example was to demonstrate the ability of GFSSP to model compressibility effects and determine the point at which nozzle flow chokes and the mass flow rate becomes independent of back pressure conditions.

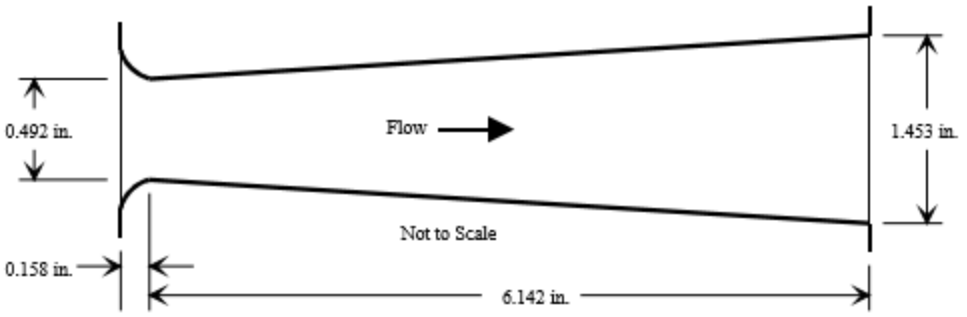

Figure 4: C-D Nozzle Example of GFSSP [6]

The same basic form of Mach number derivation used as the theoretical solution by GFSSP in modeling nozzles serves as the governing equation in this work; Equation 1.2, above. While GFSSP utilizes a finite-volume solution approach to accommodate fluid conservation equations [6], the model developed in this work numerically solves the governing Mach number equation and the corresponding temperature and pressure relationships. Additionally, the C-D nozzle case of GFSSP only demonstrated subsonic flow conditions, with promise of future supersonic development. The model created, here, however, includes the capability of the supersonic nozzle case. In short, the model developed in this work employs a simplified solution method as compared to GFSSP, yet it is capable of modeling similar nozzle cases and even extending the analysis scope of each.

Another related study, by Khunger [7], looked at the compressible flow resulting from propulsion systems known as pulse detonation engines, or PDE's. The primary analysis was to model the Fanno and Rayleigh flow cases of the resulting flow from the initial engine detonation, commonly referred to as "bleed flow." This resulting flow is essentially compressible nozzle flow which, in this case, was in a constant-area geometry followed by converging-area section. This nozzle form is displayed in Figure 5, for reference.

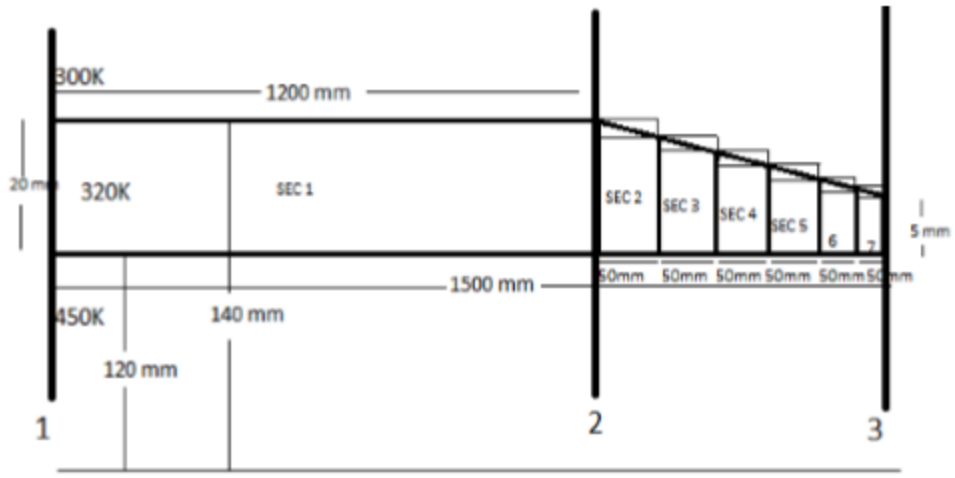

Figure 5: Post-Detonation Nozzle Geometry of a PDE [7]

In short, this study performed isolated Fanno flow and Rayleigh flow analyses and compared the associated pressure drop of each. Major conclusions included a significantly greater pressure drop resulting from Fanno flow as well as through the converging nozzle section as compared to the constant-area region. No combined Fanno-Rayleigh analysis was performed in this study.

The work of Hsieh [8] closely aligns with the present project in that it is a development of the combined effects of Fanno-line friction effects and Rayleigh-line heat transfer in a steady, one-dimensional gas flow. This work presented a comprehensive governing equation for these combined effects and evaluated several different nozzle cases: an applied constant heat flux, a constant wall temperature condition, and a constant wall temperature to total temperature ratio. While this study advanced the analysis of constant-area nozzles with combined friction and heat transfer effects, it did not extend this application to other nozzle geometries.

Chapter 2. Theoretical Establishment

Preceding a demonstration of the developed analytical and physical models for this project, a fundamental understanding of the gas dynamics involved must be established. Particularly, to understand the full physical characterization of the gas injectors under consideration, it is necessary to discuss the individual compressible flow phenomena that serve as constituents of the whole model. In compressible flow, and particularly in SCEPS injectors, four primary elements determine the resulting gas dynamics; the cross-sectional area of the internal duct, friction of the flow boundary (wall), heat transfer into the flow regime, and additional mass injection into the flow. Each of these components will be discussed, separately, so that their independent effects on the resulting flow may be understood.

2.1 Effects of Area Variation

Certainly the most fundamental study performed in gas dynamics is that of isentropic flow; flow in which the entropic state of a system is unchanged. Given that changes in cross-sectional area of the flow have no effect on system entropy; constant-mass, adiabatic, frictionless compressible flow within a variable-area channel may be considered an isentropic flow. While the entropy of such a system remains constant, the characteristics of the flow are significantly affected by changes in channel area.

For example, decreasing area generates an increase in flow velocity and a corresponding decrease in static temperature and pressure for a subsonic flow, whereas reduced velocity and increased static properties result from an increase in flow area. Likewise, reverse effects occur for area changes in supersonic flows as those resulting from subsonic flows. Area increases produce a rise in flow velocity and a reduction in static properties, while inverse properties result

from decreasing area. Figure 6 gives a summary of the effects of area change in subsonic and supersonic compressible flow.

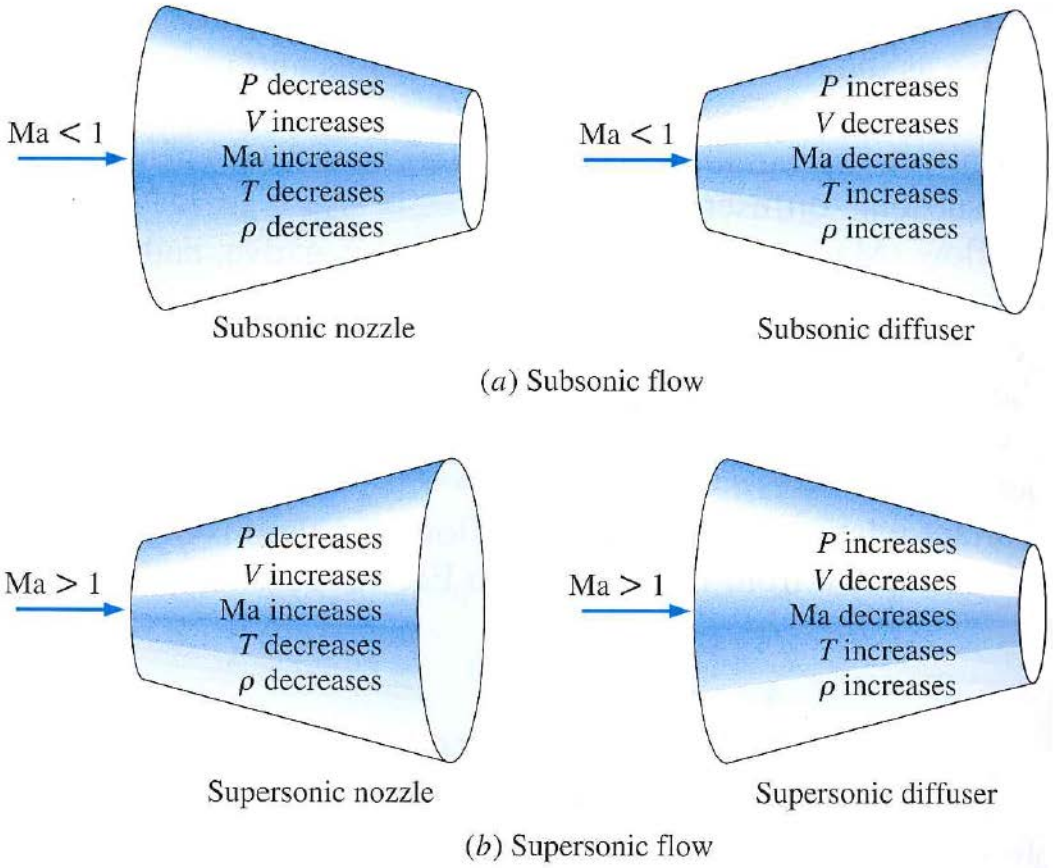

Figure 6: Flow Property Variation due to Area Changes [9]

2.2 Frictional Effects - Fanno Line Flow

The next contribution to be discussed is that of frictional effects due to the interaction of the compressible flow regime with the material characterization of the wall of the flow channel. A simple system involving steady, adiabatic, compressible flow of an ideal gas having constant specific heats and no added work in a frictional duct of uniform cross-sectional area is used to demonstrate the fundamental effects of friction in the resulting gas dynamics. A system with such characteristics produces a flow regime known as Fanno Line flow, or simply Fanno flow. The derivation of Fanno flow comes from a momentum balance on a control volume with the above conditions. Such a control volume is given in Figure 7, for clarity.

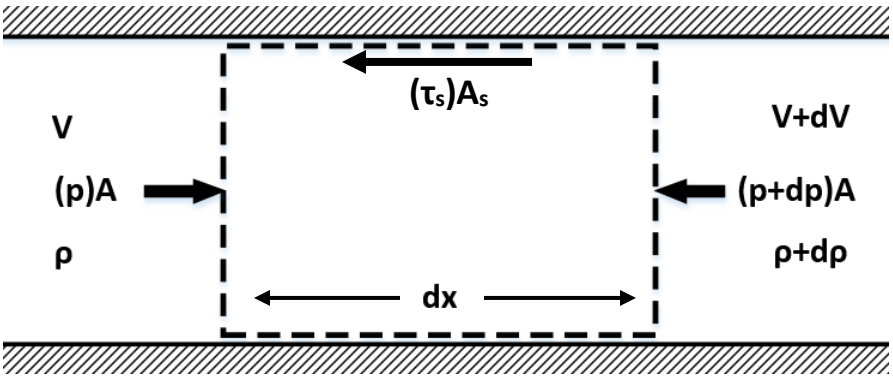

Figure 7: Fanno Flow Control Volume

A balance of the forces acting upon the control volume and the change in momentum of steady flow over a differential length, dx, serves as the starting point for the Fanno flow derivation.

$$\sum F_x = V_x(\rho V \cdot dA) \tag{2.1}$$

$$pA - \tau_s A_s - (p + dp)A = \rho A V dV \tag{2.2}$$

Where τ_s is the shear stress on the channel wall due to friction and A_s is the channel surface area in contact with the flow over the differential length. The same definition for the friction coefficient in compressible flow is also given here.

$$f = \frac{4\tau_s}{\frac{1}{2}\rho V^2} \tag{2.3}$$

Where *f* depends upon the roughness of the channel wall and Reynolds number through the nozzle. With this substitution of *f*, the exchange of the surface area definition in terms of a circular channel, and substitution of the definition of Mach number, Equation (2.2) is reproduced in the following form.

$$\frac{dp}{p} + \frac{1}{2}\gamma M^2 f \frac{dx}{D} + \gamma M^2 \frac{dV}{V} = 0 \tag{2.4}$$

With the ideal gas law and the definition of Mach number for the adiabatic case, Equation (2.4) may be further manipulated to the desired form of Equation (2.5).

$$\frac{dM}{dx} = \frac{M\left(1+\frac{\gamma-1}{2}M^2\right)}{1-M^2}\left[\gamma M^2 \frac{f}{D}\right] \tag{2.5}$$

This serves as the governing equation for Fanno flow, from which the Mach number may be determined for each differential location along the channel. This is the primary equation of interest in Fanno flow because it allows the determination of the relative static and stagnation properties, together representing a more complete thermodynamic state of the flow through the channel. A complete derivation of Equation (2.5), with intermediate steps, may be found in Chapter 9 of Reference [10], as well as many other compressible flow texts, including Reference [11].

When solving Equation (2.5), determination of the friction coefficient, *f*, is of primary interest. The most common substitution for this parameter is the Darcy friction factor, whose relationship to the coefficient is provided in Equation (2.6).

$$f_{Darcy} = \frac{1}{4} f \tag{2.6}$$

Much of the related research involving calculation of the Darcy friction factor is presented in the context of incompressible flow or, at a minimum, makes no mention of the compressibility of the fluid being studied. In such research, the evaluation of said factor is done primarily on the basis of Reynolds number distribution of an internal channel flow. Chen [12] includes a summary of a number of well-known correlations (Wood, Churchill, etc.) that apply this form of analysis, while presenting their own explicit correlation. However, none of the correlations in this summary account for combressiblity. In fact, to the author's knowledge, Peiyi and Little [13] are among the few to express the need to account for the effects of compressibility when determining f_{Darcy}. However, even their consideration of compressibility is only on the basis of density change and pressure drop over a total channel length being considered. Specifically, their formulation determines the Darcy friction factor as a constant value for a given frictional channel length. The author has yet to find a correlation that is developed for local, discrete values of Reynold's number along a channel, while accurately accounting for the effects of compressibility. The analysis chosen for this work is detailed in the proceeding chapter.

In addition to the governing Mach number equation, the energy equation for Fanno flow may be produced from the energy and continuity equations for the stated conditions, as follows:

$$\frac{s-s_1}{c_v} = \ln\left(\frac{T}{T_1}\right) + \frac{\gamma-1}{2}\ln\left(\frac{T_0-T}{T_0-T_1}\right) \tag{2.6}$$

Equation 2.6 produces the subsequent T-s diagram in Figure 8, known as the Fanno line. This represents the arrangement of states that can be obtained under the assumptions of Fanno flow for a fixed mass and total enthalpy. A complete derivation of Equation (2.6) may also be found in Chapter 9 of Reference [10].

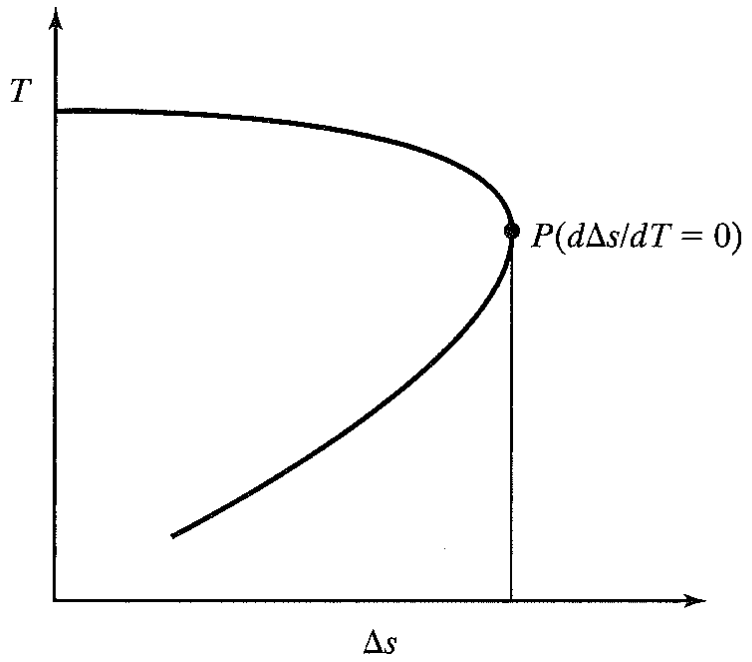

Figure 8: Fanno Line (T-s) [10]

Increasing friction, in the form of extending channel length, drives subsonic and supersonic conditioned flow to unity. For example, if fully subsonic flow under Fanno conditions exists in a channel of finite length, extension of said channel will eventually result in a Mach=1 state at the exit plane of the channel for a given mass flow. This critical length of the channel is referred to as L_{max} and is dependent upon the mass flow and the wall friction in the passage. Comparably, fully supersonic flow under Fanno conditions will be reduced to an exit Mach number equal to unity for a determined L_{max} with specific channel characteristics. Figure 9 illustrates the relationship of flow regimes based upon Mach number for a constant flow rate.

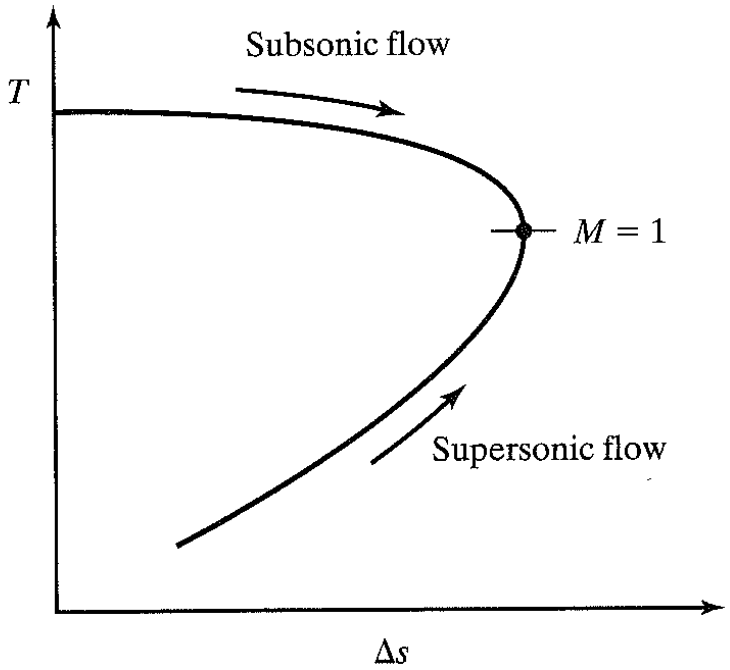

Figure 9: Mach Number Influence in Fanno Flow [10]

While subsonic and supersonic flow react similarly to increasing duct friction up to an L_{max} configuration, varying phenomena result for each flow when extension of the channel exceeds this condition. In the case of subsonic flow, added friction forces a reduction of mass flow in the channel when the length of the duct surpasses L_{max}. This is due to the thermodynamic constraint that a reduction of entropy is necessary for acceleration of the flow beyond Mach=1. And, due to the adiabatic condition in Fanno flow, a reduction of entropy cannot be achieved by temperature change, but must come about by means of a mass flow reduction. In other words, increasing the frictional length of a duct with subsonic flow beyond L_{max} induces a decrease in mass flow, thereby generating a new Fanno flow regime and corresponding Fanno line. Figure 10 shows a Fanno line shift due to channel extension beyond L_{max} ,where L_2 is greater than L_{max} (Note: $L_{max} = L_1$ for $\dot{m}_1$).

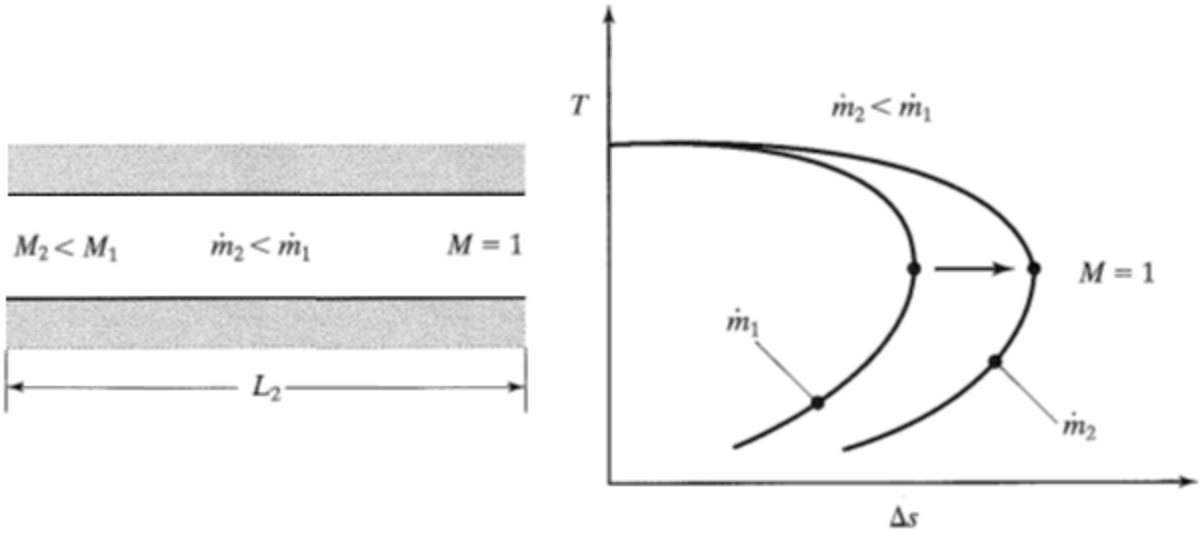

Figure 10: Fanno Line Shift due to Increasing Friction of Lengthening Duct [10]

Dissimilar to subsonic flow, supersonic flow reacts to an extended frictional duct length by way of a normal shock in the channel, yielding subsonic flow in the remainder of the length to the exit plane. The location of this shock is dependent upon the pressure at the exit plane (back pressure) and the length of the channel extension. Determination of this location will not be presented here, but may be found in Chapter 9 of reference [10].

Note: A derivation of the primary governing equations for Fanno flow can also be found in Chapter 9 of reference [10].

2.3 Effects of Heat Addition - Rayleigh Line Flow

The prior case of Fanno flow included the major assumption of an adiabatic system. Now studied is a flow regime that is diabatic (non-adiabatic), but considered to be in a frictionless channel. All other conditions of Fanno flow (1-D, steady, duct area, etc.) remain unchanged. Flow under such conditions is known as Rayleigh Line flow, or simply Rayleigh flow. Similar to Fanno flow, derivation of the governing equation of Rayleigh flow comes from an energy

balance of a differential control volume. Such a control volume, with the given conditions, above, is presented Figure 11.

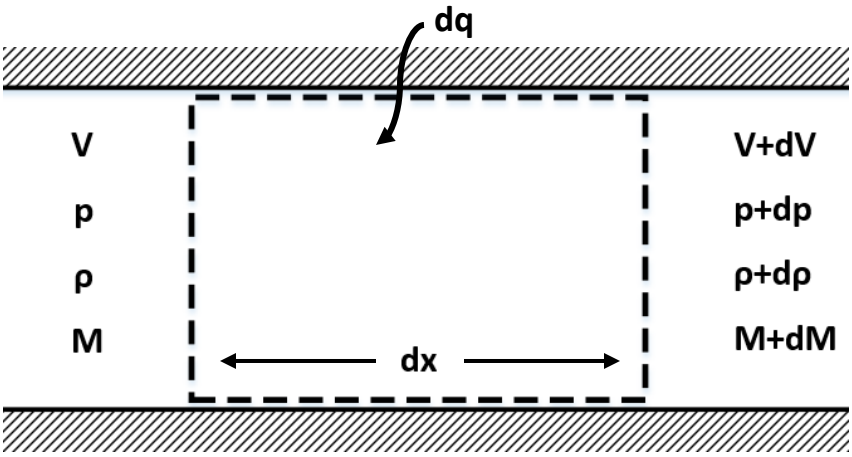

Figure 11: Rayleigh Flow Control Volume

Such derivation leads to a comparable form of the governing Mach number equation presented for Fanno flow (Equation (2.5)). For the Rayleigh condition, however, the change in Mach number per differential length of channel is related to the change in stagnation temperature over the same control volume. The governing equation for Rayleigh flow is given in Equation (2.7), below.

$$\frac{dM}{dx} = \frac{M\left(1+\frac{\gamma-1}{2}M^2\right)}{1-M^2}\left[\frac{1+\gamma M^2}{2T_0}\frac{dT_0}{dx}\right] \tag{2.7}$$

Similar to Fanno flow, Equation (2.7) serves to determine the distribution of Mach number through a given channel with heat addition or loss. Additionally, the effect of heat transfer on the temperature and pressure conditions through the channel may be subsequently determined. Rather than show a complete origination of this equation here, a detailed derivation of equations of similar form to Equation (2.7) may be found in References [10] and [11].

When calculating the Mach number distribution by means of Equation (2.7), calculation of the stagnation temperature gradient is of primary concern. This term is determined by the following relationship of heat transfer per differential flow mass.

$$\frac{dT_0}{dx} = \frac{q}{\dot{m} c_p A_s} \tag{2.8}$$

The standard heat rate equation is employed for convective heat transfer between the channel wall and the flow, given by Equation (2.9).

$$q = hA_s(T_{wall} - T) \tag{2.9}$$

Given the prior relationships for determining heat addition to the flow, determination of the heat transfer coefficient, h, becomes the parameter of importance. Subsequently, correlations for h are numerical approximations that are primarily functions of the local Reynolds number and Prandtl number of the working fluid. Such correlations are heavily dependent upon the experimental methods employed to determine them.

One well-known experimental study, by Back et.al. [14], looks at the convective heat transfer in a convergent-divergent nozzle with substantial pressure gradient effects. This investigation predicted significantly larger convective heat transfer near the nozzle throat as compared with the converging and diverging sections. Additionally, a noteworthy reduction in h occurred for lower stagnation pressures, when the nozzle has a lower driving pressure. An earlier experimental analysis by, Saunders and Calder [15], studied the convective heat transfer for high subsonic and supersonic compressible flows. Both a converging-diverging nozzle and a constant-area nozzle were used to experimentally measure heat transfer and surmise the relationship between Reynolds number and convective heat transfer. Although this relationship

was evaluated graphically for both nozzle geometries and conditions, no comprehensive correlation was produced by this study.

In summary, it is difficult to employ one comprehensive correlation for the convective heat transfer coefficient for every nozzle condition, including those of the present work. In light of this, the author has chosen to employ a more general correlation for turbulent flow in circular ducts; namely, the well-known Dittus-Boelter equation. A more detailed description of this selection is given in the following chapter, where it is applied in the developed model.

Just as with the Fanno case, the entropic state through the channel is of interest for the Rayleigh case, as well. From the continuity, momentum, and energy equations for the differential control volume, given above, the energy equation for Rayleigh flow is determined, as follows:

$$\frac{s-s_1}{c_p} = \ln\frac{T}{T_1} - \frac{\gamma-1}{\gamma}\ln\left[\frac{\left(\left(1+\gamma M_1^2\right)\pm\sqrt{\left(1+\gamma M_1^2\right)^2-4\gamma M_1^2\left(\frac{T}{T_1}\right)}\right)}{2}\right] \tag{2.8}$$

Where the subscript 1 denotes a reference state in the flow.

Figure 12 displays a plot of the curve produced by Equation 2.8, known as the Rayleigh line. Similar to the Fanno line, point A represents the location at which the change in entropy is constant with respect to temperature, yielding a Mach=1 condition. Point B simply represents the tangential instance where T/T_1 is not changing with respect to changes in entropy. It is also the boundary location for the ± sign in the second log term of Equation 2.8; the (+) term plots the curve left of point B, whereas, the (–) term charts the remainder of the curve.

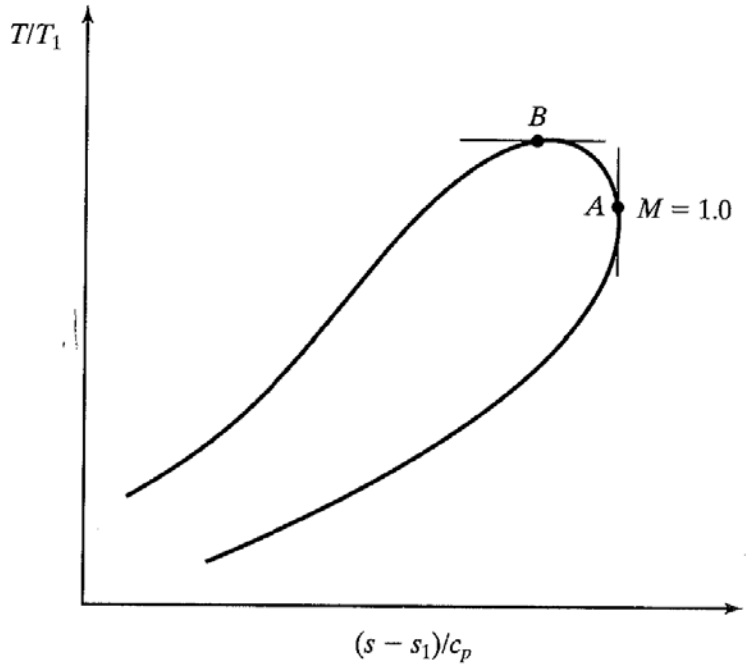

Figure 12: Rayleigh Line (T-s) [10]

A relationship analog to friction addition in Fanno flow exists for heat addition in Rayleigh Flow. In the case of fully subsonic Rayleigh flow in a finite-length channel, heat addition along the entire channel causes the flow velocity to increase to a maximum boundary of Mach=1. If this maximum condition is attained, the flow will be choked at the exit plane of the duct. This incident is represented by tracking the Rayleigh line in Figure 13 from location (a) to point A. Fully supersonic Rayleigh flow in a finite-length channel will experience the inverse effect of flow reduction with a lower boundary of Mach=1. Similarly, tracing the Rayleigh line from location (b) to point A represents this case in Figure 13.

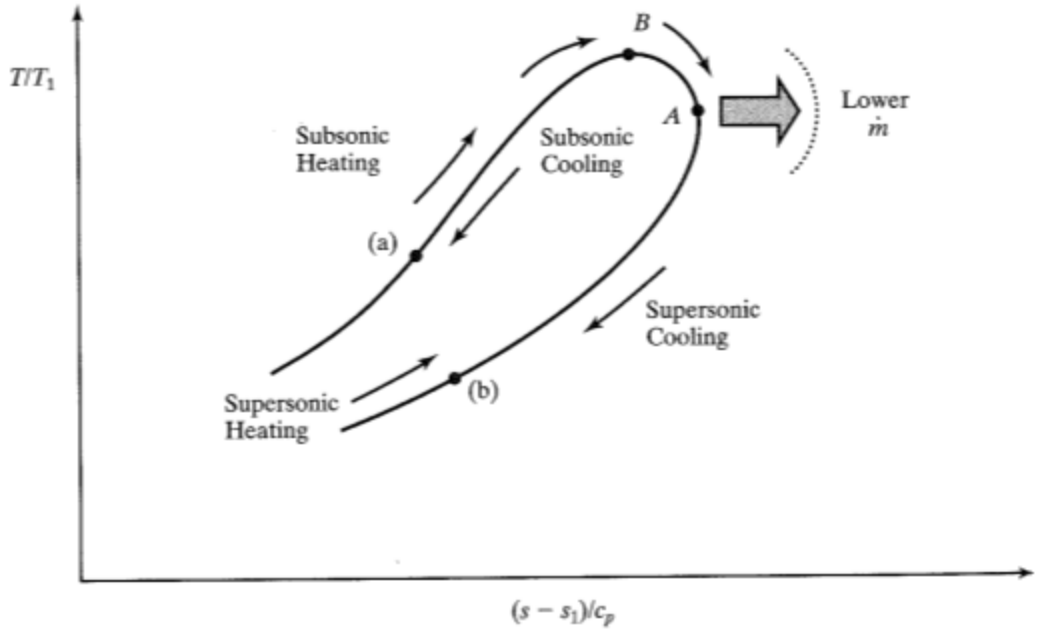

Figure 13: Mach Number Influence in Rayleigh Flow [10]

In either case of Rayleigh flow, a choked condition will exist at the exit plane of the channel for the maximum allowable heat addition for a given mass flow rate.

2.4 Effects of Mass Flow Variation

Mass injection and ejection through porous walls are common practices in many fluid flow applications. Injection of cooling fluid in rocket nozzles, film cooling in gas turbine blading, and boundary layer bleeding in supersonic wind tunnels are just a few examples of mass flux in an internal compressible flow. Analogous to the properties previously discussed, mass addition and removal have opposite effects on flow characteristics as well as inverse results in subsonic and supersonic flow. Mass addition always induces an increase in flow velocity in a subsonic flow, whereas, mass removal reduces the flow velocity. And, the opposite effects result for supersonic flows. While understanding the effect of mass changes in the flow is important, this phenomenon will not be discussed in further detail, as it is not included in the developed model of this project.

Chapter 3. Analytical Model Development

Now that a fundamental understanding of the gas dynamics within SCEPS injectors has been established, analytical models accounting for each contribution may be acquired. Several different models will be developed that include different combinations of the physical phenomena just discussed. In order to accomplish this, it is necessary to define a quasi-one dimensional control volume within an internal channel with a compressible flow. Figure 14 presents said system which accounts for boundary friction, heat addition, mass injection, and area variation.

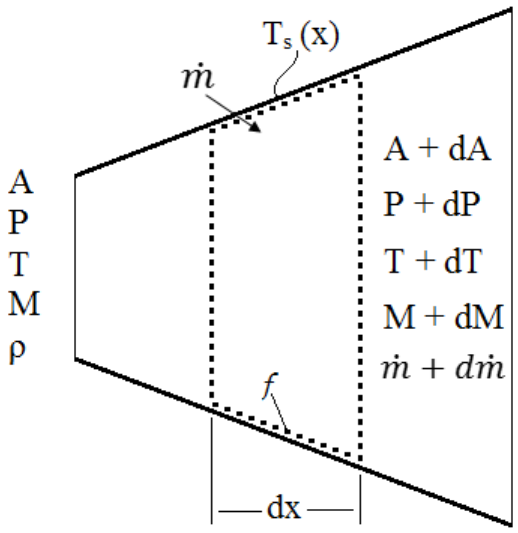

Figure 14: Quasi-1D Control Volume

From this control volume, a relationship for the Mach number of the resulting flow may be determined from the combined contribution of each physical component. Shapiro [11] developed such a correlation that has been well accepted as defining the full thermodynamic state of the given system. This Mach number relationship is given in Equation 3.1.

$$\frac{dM^2}{M^2} = -\frac{2\left(1+\frac{\gamma-1}{2}M^2\right)}{1-M^2}\frac{dA}{A} + \frac{\left(1+\gamma M^2\right)\left(1+\frac{\gamma-1}{2}M^2\right)}{1-M^2}\frac{dT_0}{T_0} + \frac{\left(\gamma M^2\right)\left(1+\frac{\gamma-1}{2}M^2\right)}{1-M^2}\left(4f\frac{dx}{D} + \frac{dX}{\frac{1}{2}\gamma pAM^2} - 2y\frac{d\dot{m}}{\dot{m}}\right) + \frac{2\left(1+\gamma M^2\right)\left(1+\frac{\gamma-1}{2}M^2\right)}{1-M^2}\frac{d\dot{m}}{\dot{m}} \quad (3.1)$$

Further manipulation of this formula was done in order to obtain the desired Mach number gradient in the axial coordinate of the injector; namely applying the Mach term derivative on the left hand side, dividing by dx, and factoring out common terms on the right hand side. The Darcy friction factor relationship was also substituted for the generic fiction factor of Equation (3.1).

$$f_{Darcy} = \frac{1}{4}f \quad (3.2)$$

After simplification, the preferred form of the governing equation is given in Equation (3.3). Individual terms have been labeled for convenient referencing.

$$\frac{dM}{dx} = \overbrace{\frac{M\left(1+\frac{\gamma-1}{2}M^2\right)}{1-M^2}}^{\text{A}}\left[\overbrace{\frac{\left(1+\gamma M^2\right)}{2T_0}\frac{dT_0}{dx}}^{\text{B}} + \overbrace{\left(\gamma M^2\frac{f_{Darcy}}{2D} + \frac{dX}{\frac{1}{2}\gamma pAM^2} - 2y\frac{d\dot{m}}{\dot{m}}\right)}^{\text{C}} - \overbrace{\frac{1}{A}\frac{dA}{dx}}^{\text{D}} + \overbrace{\frac{\left(1+\gamma M^2\right)}{\dot{m}}\frac{d\dot{m}}{dx}}^{\text{E}}\right] \quad (3.3)$$

Distinct terms in Equation (3.3) (B-G) denote the individual influence of each physical component represented in the quasi-1D control volume. Term A, in particular, is the common factor of each of these terms, and it governs the relative impact of the calculated Mach number. Take note of the denominator in this term, as a singularity occurs at the sonic point (M=1). At this point, the value for the Mach gradient is undefined, and the sign of the term reverses from positive to negative when passing from subsonic to supersonic flow, thereby reversing the effect

of each distinct term. How this critical point is handled in the analytical models will be discussed for each individual case. A summary of each term of Equation (3.3), and its influence, is given in Table 1.

Table 1: Reference of Governing Equation Terms

Reference	Term	Description	Influence on Mach Number			
			Subsonic		Supersonic	
			(+)	(-)	(+)	(-)
A	$\frac{M\left(1+\frac{\gamma-1}{2}M^2\right)}{(1-M^2)}$	Subsonic/Supersonic Multiplier	Positive (+)		Negative (-)	
B	$\frac{(1+\gamma M^2)}{2T_0}\frac{dT_0}{dx}$	Heat transfer into control volume (Rayleigh term)	Velocity Increase	Velocity Decrease	Velocity Decrease	Velocity Increase
C	$\gamma M^2 \frac{f_{Darcy}}{2D}$	Momentum change due to flow boundary (wall) friction (Fanno term)	Velocity Increase	N/A	Velocity Decrease	N/A
D	$\frac{dX}{\frac{1}{2}\gamma pAM^2}$	Momentum change due to shear forces in the flow	Velocity Increase	N/A	Velocity Decrease	N/A
E	$2y\frac{d\dot{m}}{\dot{m}}$	Momentum change due to relative velocity of mass flux to axial flow	Velocity Decrease	Velocity Increase	Velocity Increase	Velocity Decrease
F	$\frac{1}{A}\frac{dA}{dx}$	Cross-sectional area variation of the internal flow passage	Velocity Decrease	Velocity Increase	Velocity Increase	Velocity Decrease
G	$\frac{(1+\gamma M^2)}{\dot{m}}\frac{d\dot{m}}{dx}$	Mass flux through the control volume boundary (injection/ejection)	Velocity Increase	Velocity Decrease	Velocity Increase	Velocity Decrease

Once the governing equation is solved, the corresponding static and stagnation pressure and temperature may be subsequently calculated via the following relationships:

$$\frac{T(x)}{T(0)} = \frac{T_0(x)}{T_0(0)}\frac{1+\frac{\gamma-1}{2}(M(0)^2)}{1+\frac{\gamma-1}{2}(M(x)^2)} \tag{3.4}$$

$$\frac{P(x)}{P(0)} = \frac{A(0)}{A(x)} \frac{M(0)}{M(x)} \sqrt{\frac{T(x)}{T(0)}} \tag{3.5}$$

With these equations, the thermodynamic state of the injector model may be defined.

Three analytical models were developed in MATLAB to demonstrate the various phenomena that may be occurring in SCEPS injectors. The basic structure of each model code remained the same, with special treatment being applied wherever sonic conditions take place. Whenever the Mach number reaches unity in the injector, the governing equation is undefined, and therefore, becomes a critical location. At this point, special specification was necessary, which became the starting point of subsequent calculations. A chart of the fundamental procedure for all models is given in Figure 15. More thorough descriptions of the development of each individual model and their predictions will be detailed in the following sections.

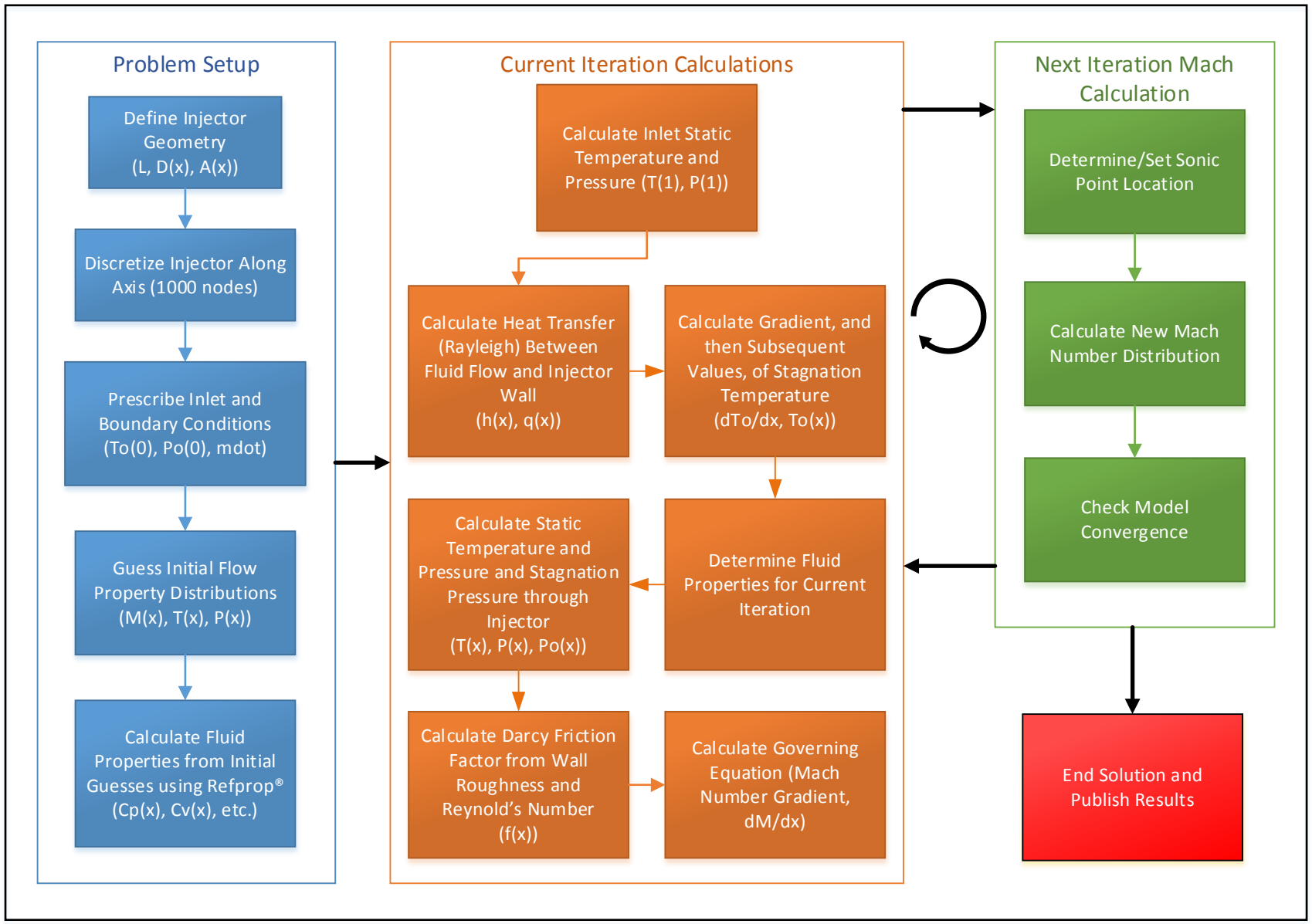

Figure 15: Analytical Model Logic Diagram

3.1 Friction Determination

As previously stated, the Darcy friction factor is used to determine the effect of wall friction on the resulting flow dynamics in the injector. This factor may be computed by the Colebrook-White equation [16], which relates the wall roughness and Reynolds number for flow in circular pipes. This correlation has many approximations that have since been developed, each of which may apply for specific ranges of Reynolds number and the relative wall roughness ε/D. Likely the most commonly utilized approximations for the Colebrook-White equation are the Swamee-Jain [17] and Haaland [18] equations, given below.

$$f_{Swamee-Jain} = \frac{1}{4}\left(\log\left(\frac{\varepsilon/D}{3.7} + \frac{5.74}{Re^{0.9}}\right)^{-2}\right) \tag{3.7}$$

$$f_{Haaland} = \left(-1.8\ \log\left(\left(\frac{\varepsilon/D}{3.7}\right)^{1.11} + \frac{6.9}{Re^{0.9}}\right)\right)^{-2} \tag{3.8}$$

Both of these approximations were selected because of their applicability to the given models' roughness and Reynolds number ranges. The Swamee-Jain and Haaland equations calculate the Darcy friction factor each iteration of the model, and the average of their values is then used in the subsequent calculation of the governing equation.

3.2 Heat Transfer Component

In order to accurately predict the mean flow temperature of the gas through the injector, an appropriate heat transfer methodology must be employed. In the presented model, a uniform heat flux is applied as a boundary condition at the injector wall. With this input parameter, the heat transfer to the gas is assumed constant along the injector. This simplifying assumption

allows for a basic demonstration of the presented model, permitting a more noticeable comparison to the effect of wall friction. With this simple approach, the heat addition to the gas flow along the injector is determined by the following equation.

$$q = q"\pi D \Delta x \tag{3.9}$$

Subsequently, the axial gradient of stagnation temperature is calculated and utilized in the governing equation.

$$\frac{dT_0}{dx} = \frac{q}{\dot{m} c_p \Delta x} \tag{3.10}$$

If the wall temperature is specified rather than a uniform heat flux, a suitable correlation must be selected to account for the heat transfer from the wall to the gas flow. As was highlighted in the previous chapter, a comprehensive correlation for convective heat transfer for every nozzle case is not readily obtained. For this reason, the Dittus-Boelter correlation for fully developed, turbulent flow in circular pipes was implemented because it applies for the conditions in each nozzle case. a Reynolds number range of $1x10^4 < Re < 1.2x10^5$, Prandtl number values ranging from 0.7 to 120, which satisfy the order of values of the Prandtl and Reynolds numbers calculated for this experiment. This correlation only applies for fully developed, turbulent flow, which occurs for pipes that meet the criterion, $\frac{L}{D} \gtrsim 10$. Since each of the nozzle geometries studied, here, meet these requirement, the Dittus-Boelter correlation is appropriately applied.

$$h = 0.023 \mathrm{Pr}^{0.4} Re^{0.8} \frac{k_f}{D} \tag{3.11}$$

Once determined, the heat transfer coefficient is employed by the standard equation for heat transfer in a circular duct.

$$q = h\pi D \Delta x (T_{wall} - T) \tag{3.12}$$

Finally, the calculated heat rate is then employed by Equation (3.13), which gives the gradient of stagnation temperature at each discretized location in the nozzle.

$$\frac{dT_0}{dx} = \frac{q}{\dot{m} c_p \Delta x} \tag{3.13}$$

This parameter then becomes the primary input representing heat transfer in the governing equation. Each of the prior relationships, Equation (3.11) - (3.13), is updated with each subsequent iteration of the model until convergence.

3.3 Fanno-Rayleigh Model

The first model to be considered is the design case. A constant-diameter channel with frictional effects and heat transfer constitutes the normal operating condition of SCEPS injectors. Although such a system is not officially described using a combined term in research, it will be referred to as Fanno-Rayleigh flow in this work.

Since heat transfer and friction are the main components considered in this case, the majority of terms in the governing equation (D-G) drop out, reducing it to the following form:

$$\frac{dM}{dx} = \frac{M\left(1+\frac{\gamma-1}{2}M^2\right)}{(1-M^2)}\left[\frac{(1+\gamma M^2)}{2T_0}\frac{dT_0}{dx} + \gamma M^2 \frac{f_{Darcy}}{2D}\right] \tag{3.6}$$

It may be noted that Equation (3.6) is simply a combined form of Equation (2.5) and Equation (2.7). This confirms both the mathematical and physical nature of adding together the effects of friction and heat transfer.

The physical characteristics of the design case are chosen such that the injector contains a subsonic inflow and a choked condition at the exit plane. This is done so that steady operation may be maintained by a consistent mass flow rate. To ensure this, the inlet stagnation pressure,

P_o, is chosen such that the pressure ratio of the injector, P_o/P_{back} , is larger than the critical value at which choked flow occurs for the given features (D, L, T, Rgh., etc.). Flow will remain choked for all higher values of P_o, yet the mass flow through the nozzle will increase as P_o increases. A summary of the Fanno-Rayleigh injector design case is provided in Table 2.

Table 2: Injector Design Characteristics - Fanno-Rayleigh Case

	Parameter	**Dimension**
Geometry	Axial Length	L = 8 [in] (0.203 m)
	Diameter	D(x) = 0.25 [in] (0.006 m)
Inlet Conditions	Stagnation Temperature	$T_o(1)$ = 40 [℉] (278 K)
	Stagnation Pressure	$P_o(1)$ = 150 [psia] (1034 kPa)
Boundary Conditions	Uniform Wall Heat Flux	$q''_{wall}(x)$ = 50 [Btu/s·ft^2] (5.68x10^5 W/m^2)
	Wall Roughness	Rgh(x) = 63 x 10^{-6} [in] (1.60x10^{-6} m)
	Back Pressure	P_{back} = 1.0 [atm] (101 kPa)

3.3.1 Summary of Model Code

Numerical approximation of the governing equation in each model case requires an iterative solution method. In other words, the initial distribution of properties (i.e. T(x), P(x), M(x), etc.) must be guessed and then subsequently calculated by the next solution to the governing equation. In order to ensure that the solution does not immediately diverge, initial guesses must be chosen such that they relatively approximate the final solution.

In the case of Fanno-Rayleigh flow, the velocity of the flow is known to accelerate from subsonic values to a sonic condition at the nozzle exit. The actual Mach number solution, as predicted by Shapiro [11] (pg. 248) in a similar case, has a positive parabolic distribution in its final form. However, a linear profile of Mach number from subsonic to sonic values is a

sufficient approximation for the initial guess. Likewise, the static temperature and static pressure distributions decrease from inlet to outlet and have a negative parabolic final form. As with Mach number, the initial temperature and pressure profiles may be linear, yet decreasing distributions.

Due to the nonlinear nature of the governing equation, it is necessary to constrain the change of the solution between each iteration by a selected limiting factor. If the difference between the value of dM/dx from the current iteration and that of the previous iteration is greater than the limiting factor, the current iteration is incremented by the value of the factor instead of the calculated value. Once the change between iterations is less than the limiting factor, the governing equation is no longer constrained and may naturally iterate to convergence. The basic logic structure employed in the code is given in Figure 16.

$$If: M_{(j,i+1)} - M_{(j,i)} > Factor: Then \rightarrow M_{(j,i)} = M_{(j,i-1)} - Factor$$

$$Else: M_{(j,i)} = M_{(j-1,i)} - dx\left(\frac{dM}{dx}\right)_{(j,i)}$$

Figure 16: Model Convergence Logic

The solution is considered converged when the difference between subsequent calculations is less than a selected convergence criterion ($1x10^{-6}$), which is a small percentage of the average final solution value (≈ 0.0001%). If such a constraint is not applied, the nonlinear governing equation will quickly "overshoot" the solution due to too great a difference between the initial guesses and the actual solution. However, application of said factor results in a slower convergence rate of the solution and requires some iteration by the user in order to find values that allow the solution to converge in a reasonable time.

3.3.2 Characteristic Model Properties

This section serves to display the distribution of the relevant physical characteristics in the Fanno-Rayleigh nozzle, as predicted by the numerical model. Evaluation of these parameters in terms of their agreement with compressible flow theory, together with a comparison of an equivalent analysis to that demonstrated by NASA's GFSSP, are sufficient to determine if the model is performing properly. In other words, if the pressure, temperature, and velocity characteristics agree with the expected gas dynamic trends for each given set of inputs (geometry, inlet conditions, friction, etc.) and the model is able to produce the same results for equivalent inputs to the GFSSP example, then sufficient confidence in its predictions may be achieved.

Figure 17 displays the numerical model's prediction of Mach number distribution (and essentially velocity) through the Fanno-Rayleigh nozzle plotted along a profile of its constant-area channel. To show the relative Fanno (friction) and Rayleigh (thermal) effects on the flow, the model was executed with each isolated case and all were plotted simultaneously. As expected, the nozzle accelerates the flow to sonic conditions at the exit, with a greater rate of increase in the latter half. This agrees with general gas dynamics theory, which predicts a comparable distribution of velocity in nozzles.

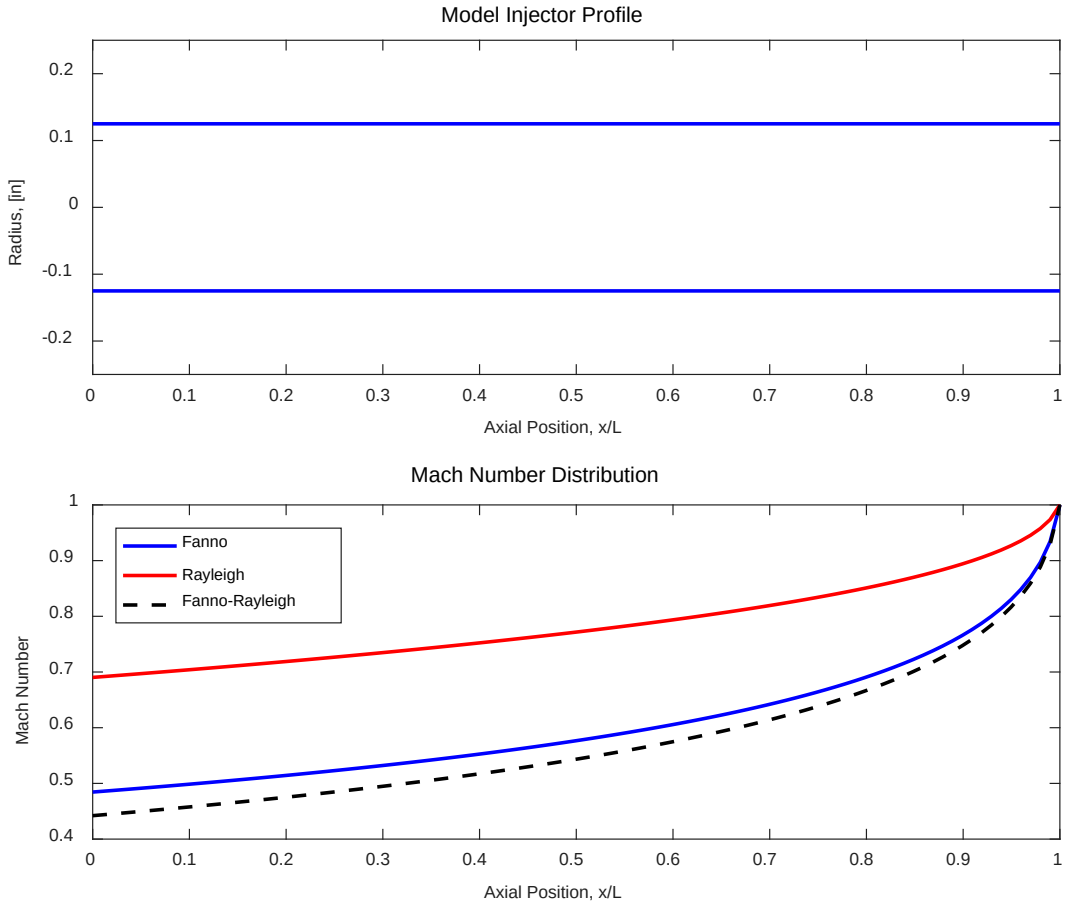

Figure 17: Fanno-Rayleigh Nozzle Velocity Distribution

Figure 18 presents the anticipated static and stagnation properties of the given Fanno-Rayleigh nozzle condition. The static and stagnation temperature exhibit a general increasing trend due to heat transfer to the fluid regime from the nozzle walls. The static temperature, dissimilar to the stagnation temperature, is predicted to experience a rapid decline near the nozzle exit due to the rapid expansion of the gas as it approaches the exit of the nozzle. The stagnation temperature, however, holds a consistent (nearly linear), increasing trend through the entire nozzle. This phenomenon is due to the increased flow velocity contribution near the nozzle exit that balances the temperature reduction due to expansion of the gas.

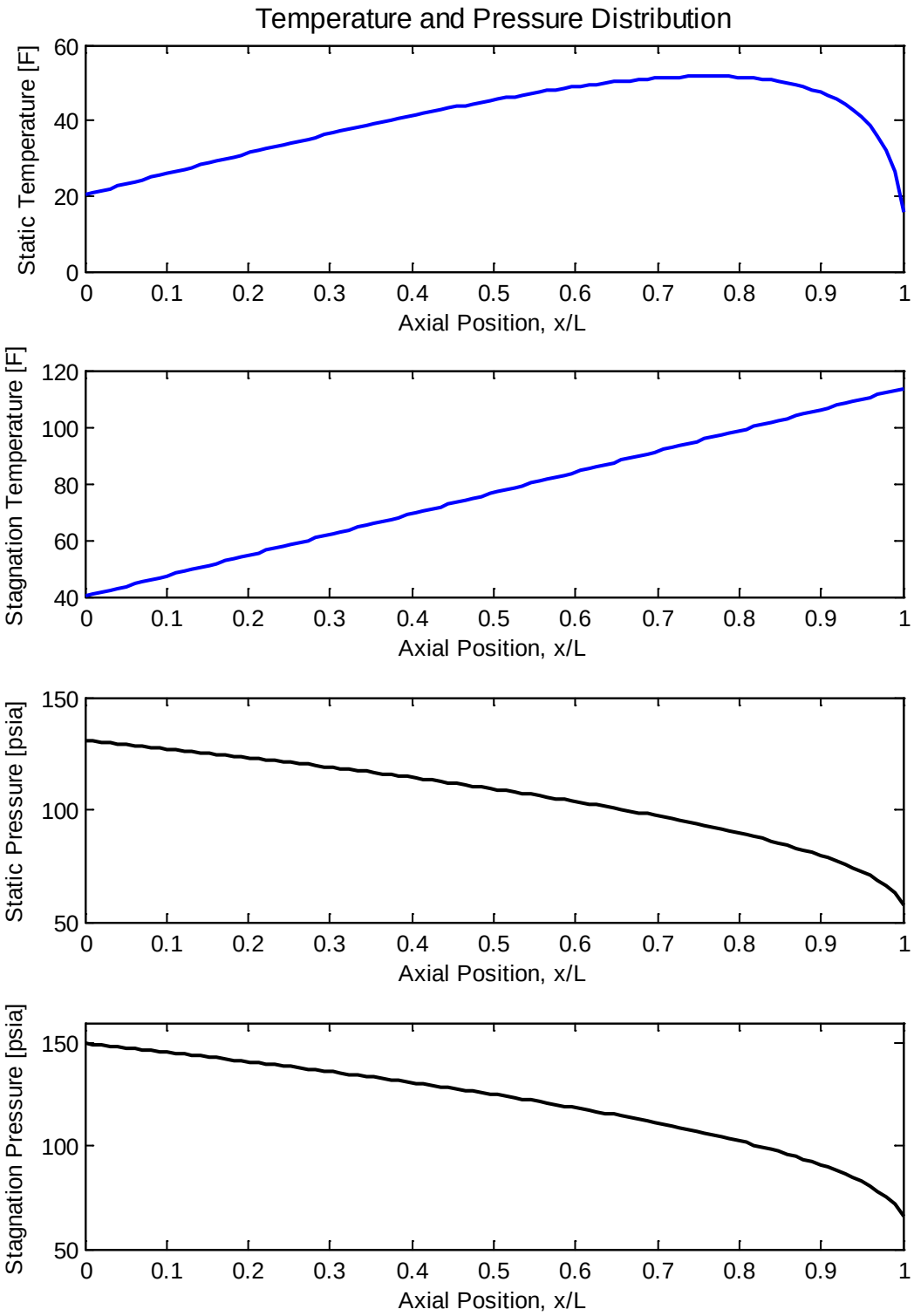

Figure 18: Fanno-Rayleigh Nozzle Temperature and Pressure Distributions

3.3.3 Entropy Characteristics

In addition to the primary model parameters, plotting the characteristic temperature-entropy (T-S) curve for any given nozzle conditions aides understanding of the energy state through the nozzle. Of primary interest, the choking point in the nozzle, or the location at which M = 1, may be determined by evaluation of this diagram. The location on the T-S curve that represents the choked point in the nozzle is given by the following condition in Equation 3.14.

$$\frac{\partial(\Delta S)}{\partial T} = 0 \tag{3.14}$$

Most compressible flow texts, including John [10] and Shapiro [11], present this prediction of choked flow for Fanno line flow and Rayleigh line flow, separately. These sources then compare the separate cases for a given nozzle on the same T-S diagram to demonstrate the occurrence of shockwaves, as shown by the transition (dotted line) from a supersonic location (1) to subsonic conditions (2) in Figure 19.

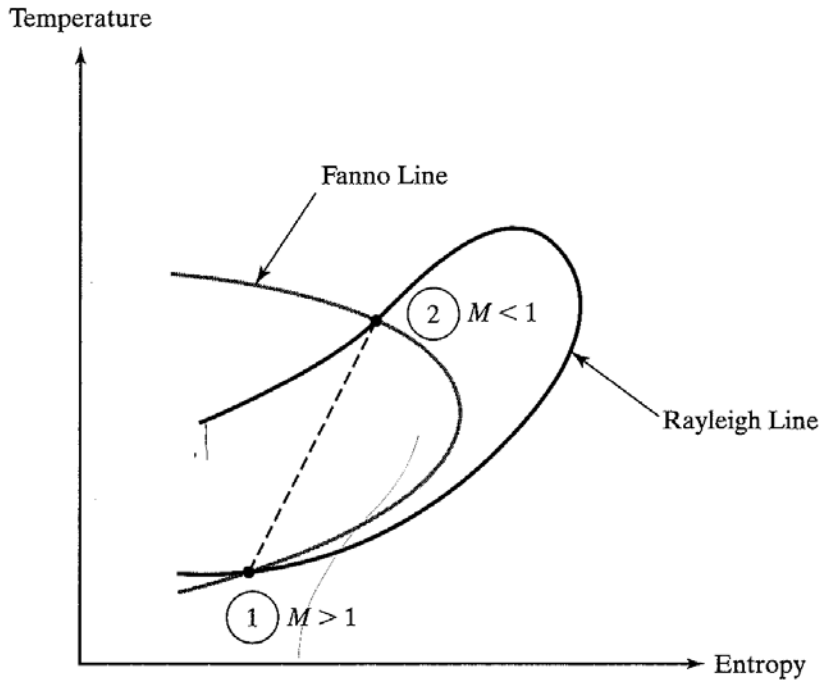

Figure 19: Individual Fanno and Rayleigh Lines for Same Nozzle Case [10]

Following the individual presentation of these flows, the combined effects of heat transfer and friction are developed, and the combined energy equation is provided in the succeeding form.

$$\frac{\Delta s}{R} = \frac{\gamma}{\gamma - 1} \ln\left(\frac{T}{T_1}\right) - \ln\left(\frac{P}{P_1}\right) \tag{3.15}$$

However, neither of these texts employs this combined entropy equation to predict nozzle choking, or the nozzle location at which M = 1. Moreover, the author has not discovered such use of this equation in any literature, to date. In other words, to the author's knowledge, a so-called combined Fanno-Rayleigh curve used to predict the critical Mach number condition in nozzles is not currently employed in gas dynamics texts and open-source research. In light of this, it is an objective of this work to present how this very exercise was employed in this project.

Figure 20 displays the Fanno line, Rayleigh line, combined Fanno and Rayleigh curve, and the plot of the combined heat transfer and friction energy (Fanno-Rayleigh, Equation (3.15) for the given constant-area nozzle case. The Fanno case (blue line) was produced by running an adiabatic form of the numerical model and was plotted via Equation (2.1). Subsequently, the Rayleigh case (red line) was generated by a frictionless form of the model and was produced by Equation (2.2). The combined case of friction and heat transfer (black line) was then included by plotting Equation (3.15) for the full numerical model conditions.

In order to demonstrate whether or not the combined case accurately predicts the critical Mach number condition, the Fanno and Rayleigh entropy curves were added together and plotted against the resulting temperatures of the combined case, producing the final curve (dashed, purple line). It may be readily observed that the combined Fanno-Rayleigh curve calculates a greater increase in entropy through the nozzle than the addition of the individual cases. This is

due to the related effect of friction upon the heat transfer in the nozzle. A frictional duct will change the resulting heat transfer from that of a frictionless duct, subsequently altering the change in total entropy.

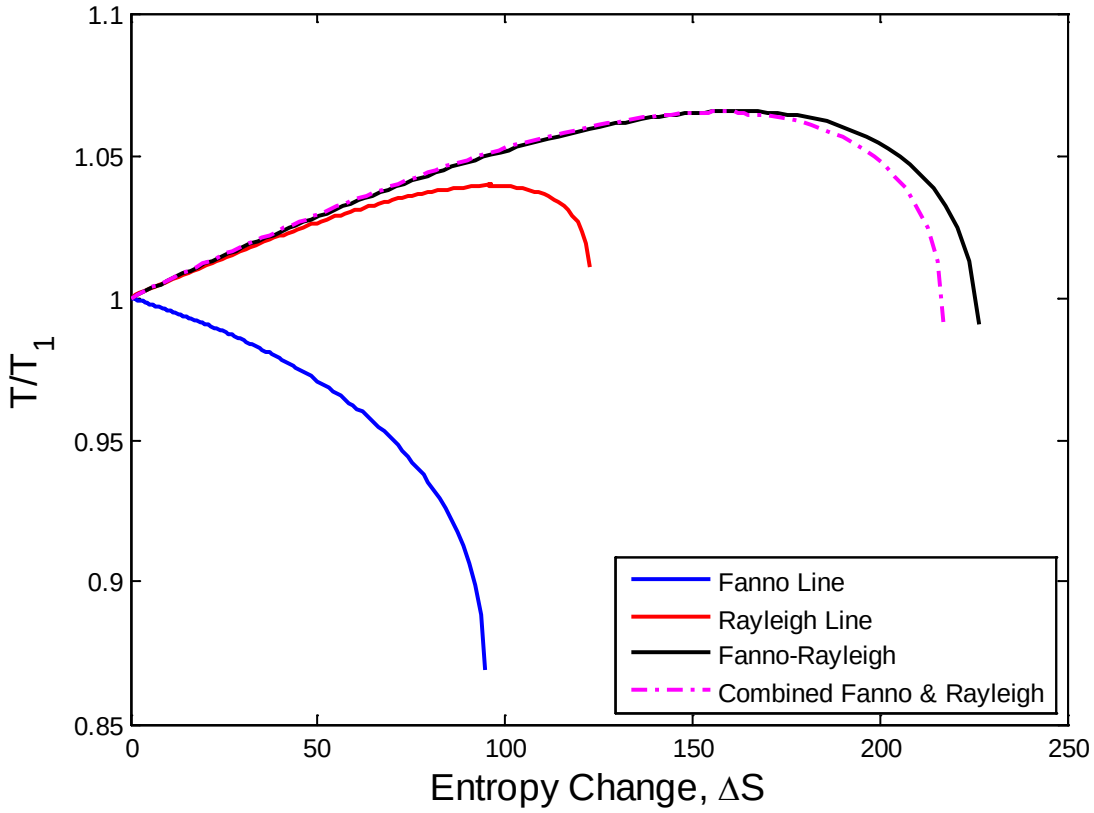

Figure 20: Fanno-Rayleigh Nozzle Flow Energy

Although the resulting entropy prediction of the summed individual and combined Fanno-Rayleigh equations differ, the location of the critical Mach number (M = 1) is predicted at the same nozzle location by both. The point of zero slope, given by the condition of Equation (3.14), is predicted to be located at the exit of the nozzle in both cases. In conclusion, the combined entropy calculation provided by Equation (3.15) may be used to predict where the Mach number will reach unity in the given nozzle case.

3.3.4 Model Validation

As stated above, demonstration of the equivalent nozzle case as the one calculated by GFSSP in Reference [5] helps to validate the accuracy of the numerical model. The conditions of the example in Figure 21, below, were used as inputs to the Fanno-Rayleigh nozzle of the numerical model. Note that Figure 21 shows an inlet Mach number of 0.45, since this was used for the isolated Fanno flow condition. In the combined Fanno-Rayleigh case, an inlet Mach number of 0.5 was used as an input to the GFSSP model, so it is the expected result of the reverse-calculation of Mach number in the model of this work. Also included as inputs were a constant friction factor, f = 0.002, and a uniform heat rate, Q = 555 BTU/s.

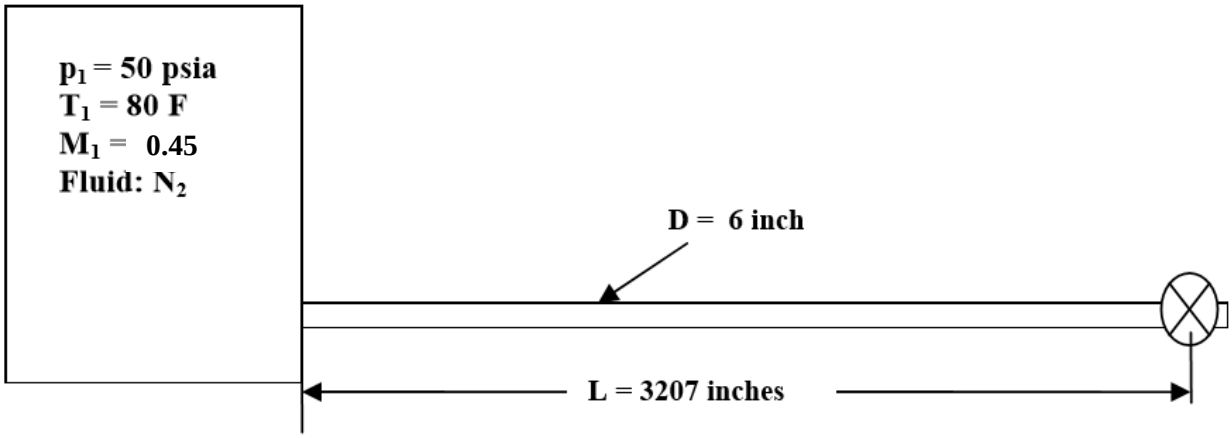

Figure 21: Example Schematic for GFSSP Fanno-Rayleigh Demonstration [5]

Figures 22-24, below, display the comparison of the primary model characteristics as predicted by GFSSP and the model developed in this work. Comparison of these characteristics (velocity, pressure, and temperature), alone, is adequate to determine if the numerical model has the same fidelity as GFSSP. Additionally, since GFSSP is effective in calculating the gas dynamics in a particular nozzle, as demonstrated by similarity to the analytical solution, the credibility of the developed model is helped by its nearness to the GFSSP solution.

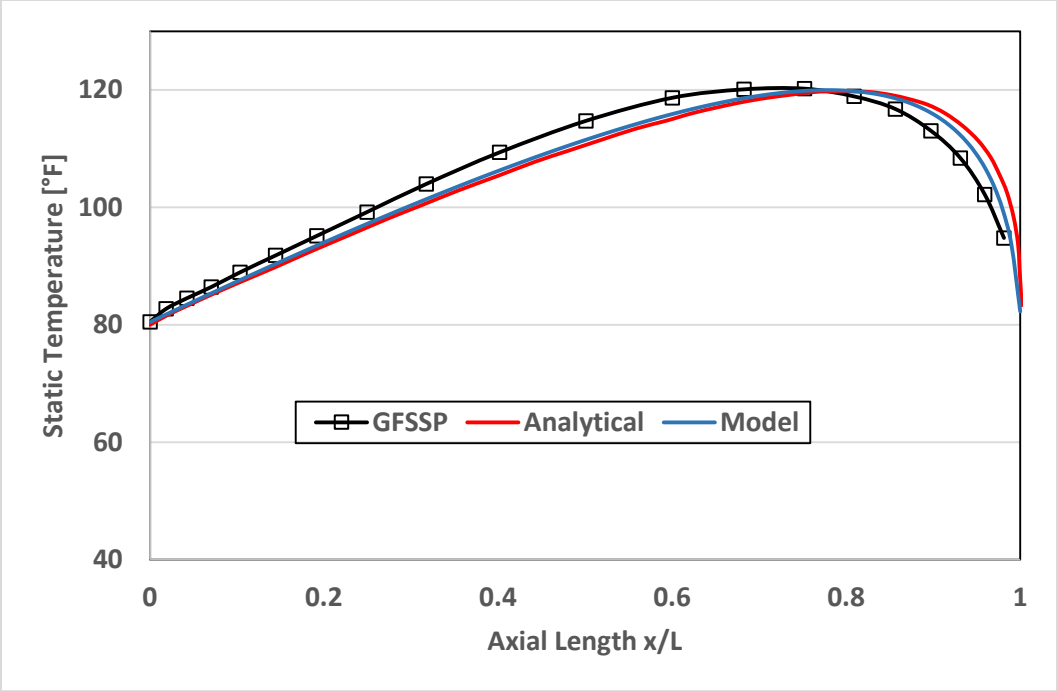

Figure 22: Numerical Model Static Temperature Comparison to GFSSP [5]

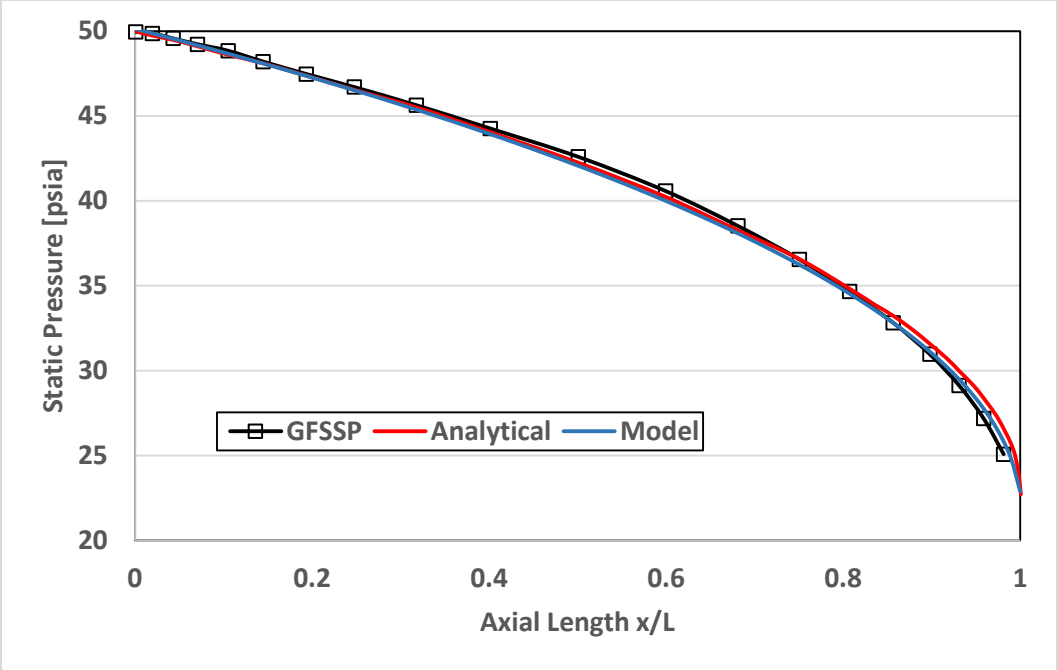

Figure 23: Numerical Model Static Pressure Comparison to GFSSP [5]

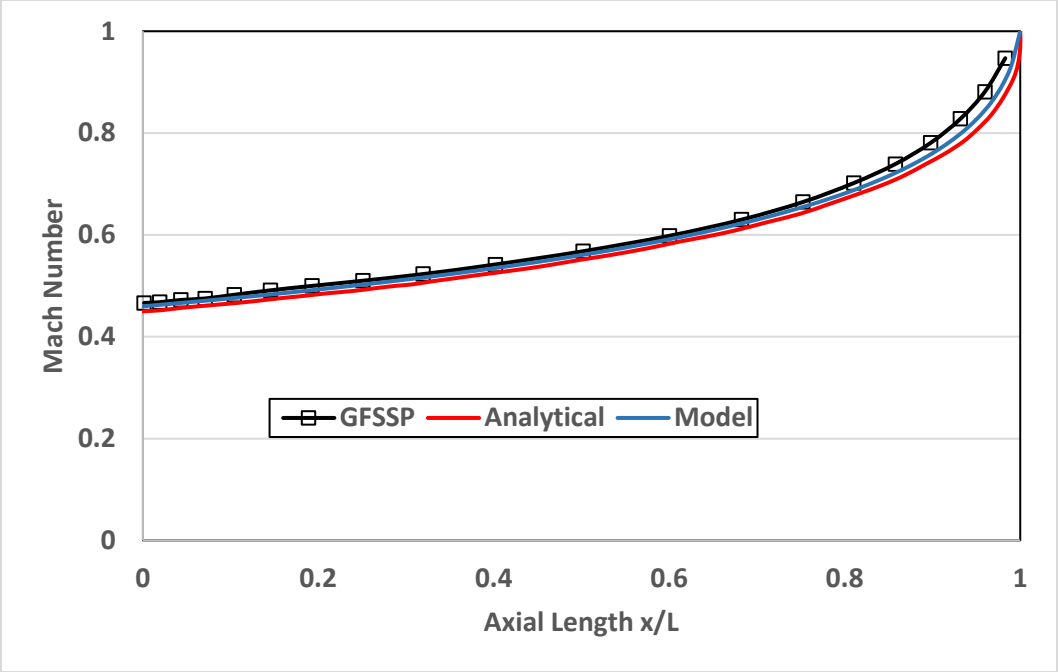

Figure 24: Numerical Model Mach Number Comparison to GFSSP [5]

According to the comparison in the above figures, each of the critical characteristics of the developed model agrees well with the equivalent parameter predicted by GFSSP. It is noteworthy that the conditions at the inlet of the nozzle match between the two codes, given that GFSSP inputs the inlet parameters, including Mach number, and calculates in the direction of the exit plane, whereas the developed numerical model inputs the stagnation properties at the inlet, while calculating from the choked exit plane backwards toward the inlet. In other words, the model in this work sets the stagnation properties and the choked nozzle condition and iterates the governing equation until the nozzle state adjusts to the given set of conditions. Therefore, although the two codes employ different solution methodologies, they still produce comparable results.

3.4 Converging-Area Model

After the design case was demonstrated, a converging-area nozzle geometry was input to the numerical for the same boundary conditions, shown in Table 3. This was executed in order that

greater fidelity of the model may be observed for varying nozzle geometric profiles. The governing equation now includes the area term that was neglected in the previous nozzle case, resulting in the following form.

$$\frac{dM}{dx} = \frac{M\left(1+\frac{\gamma-1}{2}M^2\right)}{(1-M^2)}\left[\frac{(1+\gamma M^2)}{2T_0}\frac{dT_0}{dx} + \gamma M^2 \frac{f_{Darcy}}{2D} - \frac{1}{A}\frac{dA}{dx}\right] \tag{3.16}$$

Table 3: Injector Design Characteristics – Converging Nozzle Case

	Parameter	Dimension
Geometry	Axial Length	L = 8 [in] (0.203 m)
	Diameter	$D(x) = \begin{cases} 0.25, \ 0 \le x \le 0.5L \ \text{[in]} \\ 0.25 - 0.01x, \ 0.5L < x \le L \ \text{[in]} \end{cases}$
Inlet Conditions	Stagnation Temperature	$T_o(1)$ = 40 [℉] (278 K)
	Stagnation Pressure	$P_o(1)$ = 150 [psia] (1034 kPa)
Boundary Conditions	Uniform Wall Heat Flux	$q''_{wall}(x)$ = 50 [Btu/s·ft^2] (5.68x10^5 W/m^2)
	Wall Roughness	Rgh(x) = 63 x 10^{-6} [in] (1.60x10^{-6} m)
	Back Pressure	P_{back} = 1.0 [atm] (101 kPa)

A converging nozzle is expected to have a higher system pressure than the design case due to greater constriction of the flow. Since the same choked condition is set, this is presumed to produce a more rapid acceleration of the flow near the exit plane of the nozzle. If this is the case, the governing equation employed by the numerical model would need to perform a more nonlinear calculation of the Mach number distribution. Dissimilar to the Fanno-Rayleigh condition, a smaller value of the limiting factor must be utilized in order to prevent divergence of the model. This more restrictive factor increases the convergence rate of the Diverging model solution, as compared with the previous cases.

3.4.1 Physical Characteristics

The resulting predictions of the converging model case (Figure 25) showed similar trends to the Fanno-Rayleigh design case, as expected. The inlet side of the nozzle showed a gentle rise in flow velocity, while the latter half displayed a rapid increase up to the choked condition at the nozzle exit. In this case, the convergence of the bore area produced an even greater change in slope than the constant-area case. The overall flow velocity was reduced, as well, given by a predicted inlet Mach number of 0.29 versus the 0.45 value of the previous case. This agrees with compressible flow theory in that a greater flow restriction should result in a reduction of inlet flow velocity for a choked nozzle condition.

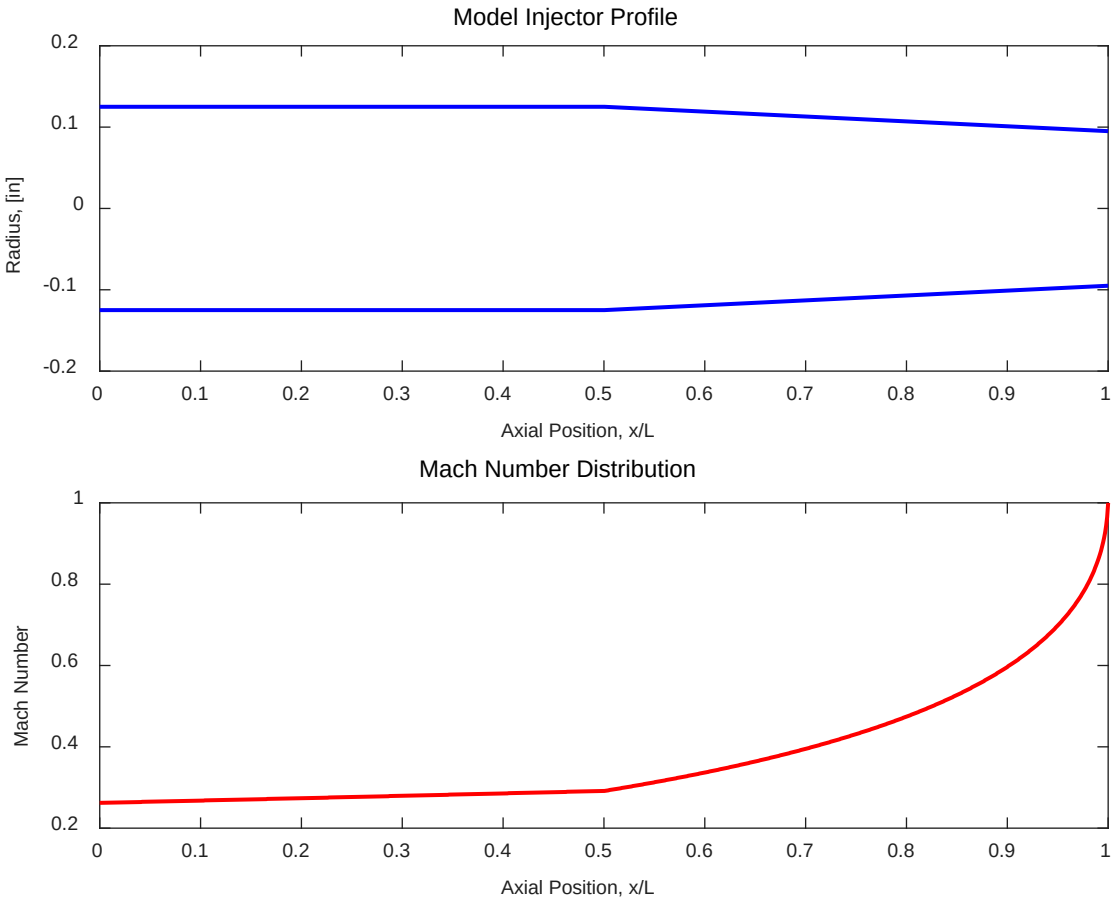

Figure 25: Converging Nozzle Velocity Distribution

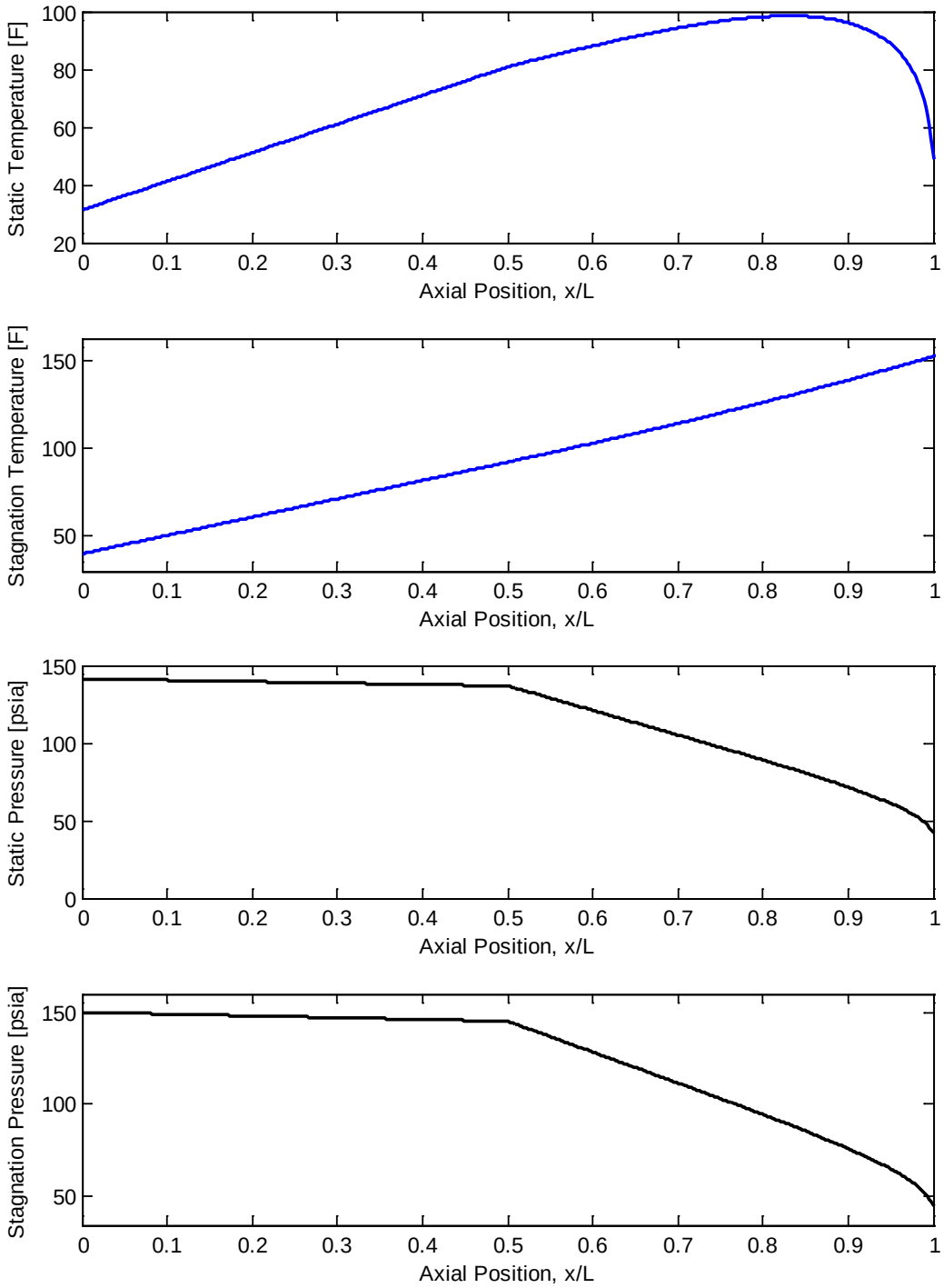

Figure 26: Converging Nozzle Temperature and Pressure Distributions

The resulting pressure and temperature conditions, as shown in Figure 26, correlate to the predicted flow reduction, demonstrated by an increased static and stagnation pressure and temperature. The greater flow restriction produces a more sustained (lesser slope) pressure in the

first half of the nozzle, forcing a more rapid expansion toward the exit to reach sonic conditions. The temperature profile increased significantly, as compared to the design case, indicating greater heat addition to the flow from the nozzle wall. This increase in temperature agrees with the lower flow velocity condition, which allows greater heat transfer due to a slower transient.

3.4.2 Entropy Characteristics

The entropic condition of the converging case is informative regarding the heat transfer and frictional effects in the bore of the nozzle. When compared to the constant-area case, the temperature-entropy curve for this nozzle (Figure 27) exhibits a large temperature, or Rayleigh, effect. As was observed in Figure 16 for the design case, Rayleigh effects drive up the temperature component of the T-S curve, while the Fanno (frictional) effects exhibit a downward trend for increasing entropy.

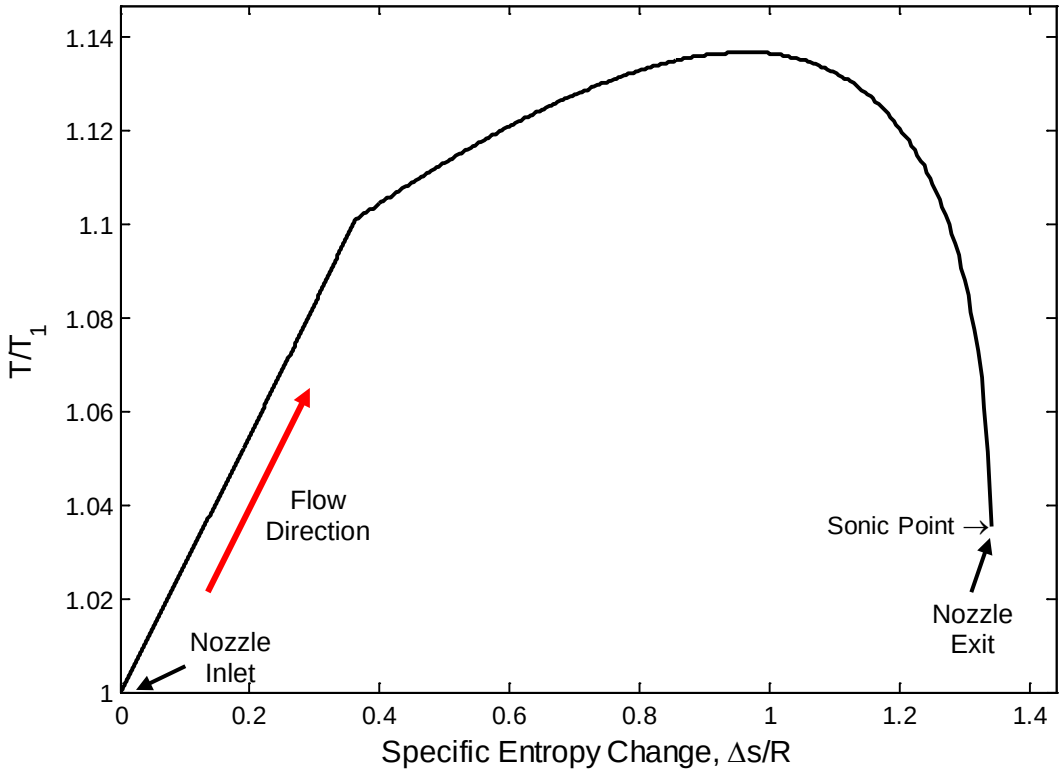

Figure 27: Converging Nozzle Flow Energy

Therefore, the greater increase in temperature exhibited by the curve, above, also demonstrates greater heat transfer effects than the design case. The downward trend to the critical Mach number condition ($\frac{\partial(\Delta S)}{\partial T} = 0$) confirms the rapid expansion of the gas near the nozzle exit and sonic condition. This also demonstrates the increased frictional effects that help drive the flow to Mach = 1.0 at the exit plane.

3.5 Diverging-Area Model

The third, and final, case developed within the numerical model was that of a diverging-area nozzle geometry. This served to demonstrate the model's ability to handle supersonic flow conditions, and in particular, transonic calculations. Dissimilar to the previous two examples, the sonic point no longer exists at the exit plane of the nozzle, but rather at the transition from constant area to the diverging section. Table 4 summarizes the inputs to the numerical model for the diverging-area case. In order to make a legitimate comparison to the previous models, all other model inputs remained the same.

Table 4: Injector Design Characteristics – Diverging Nozzle Case

	Parameter	**Dimension**
Geometry	Axial Length	L = 8 [in] (0.203 m)
	Diameter	$D(x) = \begin{cases} 0.25, \ 0 \le x \le 0.5L \ \text{[in]} \\ 0.25 + 0.01x, \ 0.5L < x \le L \ \text{[in]} \end{cases}$
Inlet Conditions	Stagnation Temperature	$T_o(1)$ = 40 [°F] (278 K)
	Stagnation Pressure	$P_o(1)$ = 150 [psia] (1034 kPa)
Boundary Conditions	Uniform Wall Heat Flux	$q''_{wall}(x)$ = 50 [Btu/s·ft^2] (5.68×10^5 W/m^2)
	Wall Roughness	Rgh(x) = 63 x 10^{-6} [in] (1.60×10^{-6} m)
	Back Pressure	P_{back} = 1.0 [atm] (101 kPa)

The same form of the governing equation as the previous converging model condition is employed, Equation 3.16. In this case, however, the sign of the area gradient is positive, resulting in velocity increases for supersonic flow and velocity reductions for subsonic conditions. In order that supersonic condition may be assumed in this nozzle geometry, the driving pressure ratio must be above the critical value for supersonic flow. This critical value was determined by the standard tables for isentropic flow for the area ratio input of the current nozzle, given below.

$$\frac{A_{exit}}{A_{throat}} = \left(\frac{D_{exit}}{D_{throat}}\right)^2 = 2.25 \tag{3.17}$$

From Table A.1 of Anderson's compressible flow text [19], the resulting pressure ratio required for fully isentropic, supersonic flow is given.

$$\frac{P_{o\,inlet}}{P_{exit}} = 13.07 \tag{3.18}$$

Although this criterion assumes isentropic, supersonic nozzle flow, with no friction or heat transfer, it still serves as a valid reference for the current assumption. In other words, if the given pressure ratio is significantly above the critical ratio for isentropic flow, then fully supersonic flow in the diverging portion of the nozzle may be assumed. Since the given pressure ratio is approximately 150/0, assuming a vacuum back pressure ($P_{back} < 1.0$ atm), it may be reasonably assumed that the nozzle is experiencing fully supersonic flow.

Given the assumption of supersonic flow, the next critical assignment in the model becomes the location of the sonic condition. As previously discussed, a Mach number of unity is a critical value that is undefined by the governing equation. Therefore, unlike the previous nozzle examples, the diverging nozzle requires the numerical model to calculate the transition from

subsonic to supersonic flow, through a sonic point. In order to accomplish this, it is necessary to determine the location in the nozzle at which the Mach number reaches unity. Gas dynamics theory informs us that this location occurs at the minimum area, or throat, of the nozzle for isentropic flow. John [10] further states the addition of heat transfer and frictional effects cause the sonic location to move slightly past the throat toward the nozzle exit. Since the resulting Mach number distribution variance is minimal when this slight shift is included, the developed model assumes the sonic location to take place at the throat, as in isentropic flow. Future development of the current work should include this correction in the supersonic nozzle case of the model.

Since the sonic point location is situated at the midpoint of the nozzle, the governing equation may not be calculated continuously through the nozzle. As with the previous cases, initial velocity, pressure, and temperature distributions are initialized through the nozzle to provide for the first iteration of the governing equation. However, in this example, the equation must calculate two different directions through the nozzle; backward from the sonic midpoint to the inlet and forward from the midpoint to the nozzle exit. As before, a limiting factor is needed, yet it must be applied to each calculating direction to prevent divergence around the critical sonic location.

3.5.1 Physical Characteristics

The diverging case exhibits characteristics with significant variance from the prior nozzle examples. As anticipated, the model predicts a supersonic state for a sufficient pressure ratio and increasing nozzle area. The Mach number distribution and related nozzle geometry are displayed in parallel in Figure 28.

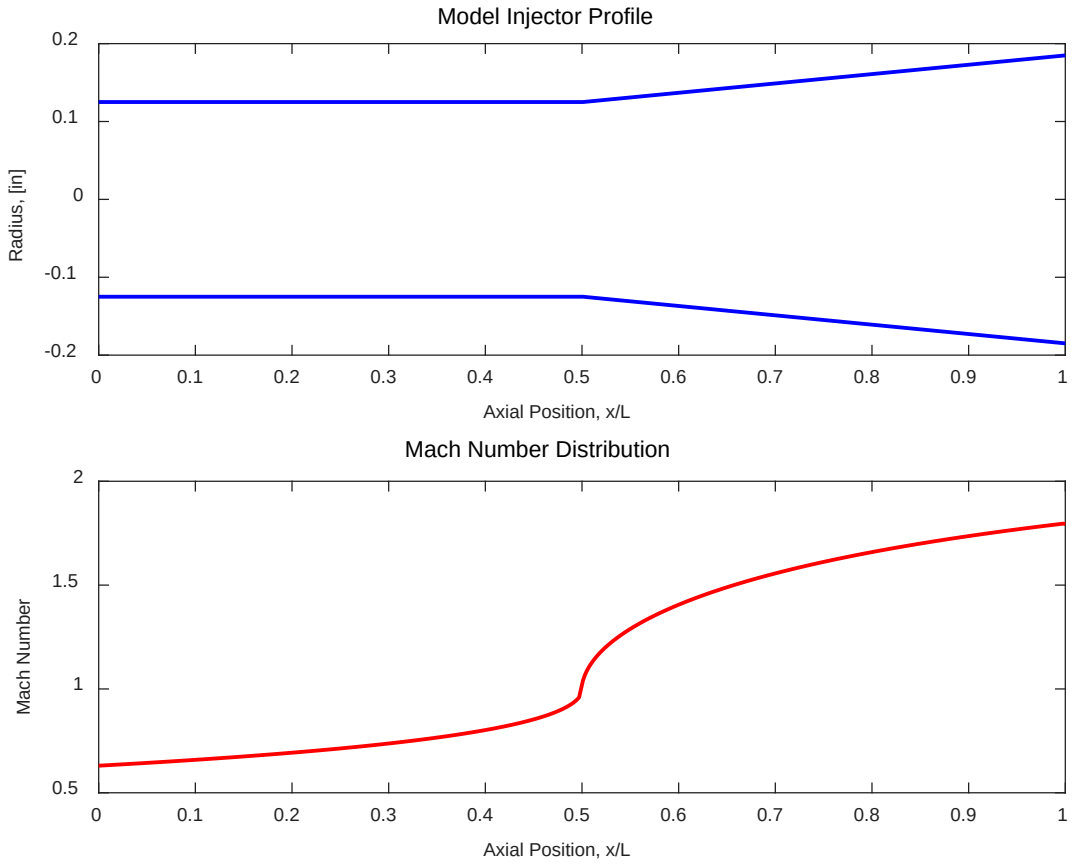

Figure 28: Diverging Nozzle Velocity Distribution

As expected, the velocity distribution in the first half of the nozzle takes a similar form to the constant and converging-area nozzles in that the flow rapidly accelerates near the sonic point. In this case, however, the flow continues to accelerate through the remainder of the nozzle, up to an approximate exit Mach number value of 1.74. When compared with the predicted exit Mach number for isentropic flow, given below, it may be observed that the addition of heat and friction also has a substantial effect on supersonic flow.

$$M_{exit-isentropic} = 2.33 \tag{3.19}$$

This serves to confirm that friction and heat addition work to drive a compressible flow toward sonic conditions.

Similar to the velocity form, the pressure and temperature characteristics display unique forms for the diverging nozzle. Since the flow undergoes significant acceleration beyond the sonic location, further expansion of the gas is expected. As seen in Figure 29, both the static and stagnation pressures show substantial expansion of the fluid in the supersonic portion of the nozzle. The stagnation pressure, which incorporates the kinetic energy of the flow, displays the same form as the static pressure, yet with greater values. Once again comparing to isentropic predictions, the exit static pressure for an isentropic nozzle with the same inlet conditions and geometry (area ratio) is determined by the relationship given by equation 3.18.

$$P_{exit-isentropic} = P_{0_{inlet}} \cdot \left(\frac{P_{exit}}{P_{0_{inlet}}}\right) = 150\ psia \cdot \left(\frac{1}{13.07}\right) = 11.48\ psia \quad (3.20)$$

Following a similar trend to the pressures, the static temperature distribution exhibits a rapid reduction after the sonic midpoint. This demonstrates that, due to the temperature reduction from expansion, the gas is not significantly heated in the supersonic portion of the nozzle. In other words, the reduction in pressure and density of the gas is accompanied by a significant reduction in static temperature. Stagantion temperature, on the other hand, does not display a similar trend to the static temperature and pressures. This is due to the inclusion of the kinetic energy of the flow in producing stagnation values. Additionally, the lower values of stagnation temperature than the previous nozzle cases serves to confirm the temperature reduction due to gas expansion. If allowed to expand isentropically for the given nozzle, the gas would be expected to cool much more significantly than with the presence of heat transfer and friction. This is demonstrated by the isentropic prediction of the exit stagnation temperature for the given nozzle geometry and inlet conditions.

$$T_{exit-isentropic} = T_{0_{inlet}} \cdot \left(\frac{T_{exit}}{T_{0_{inlet}}}\right) = 277.6\ K_{(40\ °F)} \cdot \left(\frac{1}{2.104}\right) = 131.9K = -222.3\ °F \quad (3.21)$$

In summary, the addition of heat transfer and friction to a supersonic flow regime serves to limit the expansion and cooling of the gas as compared to a constant entropy condition. A lower velocity nozzle flow is produced, as a result.

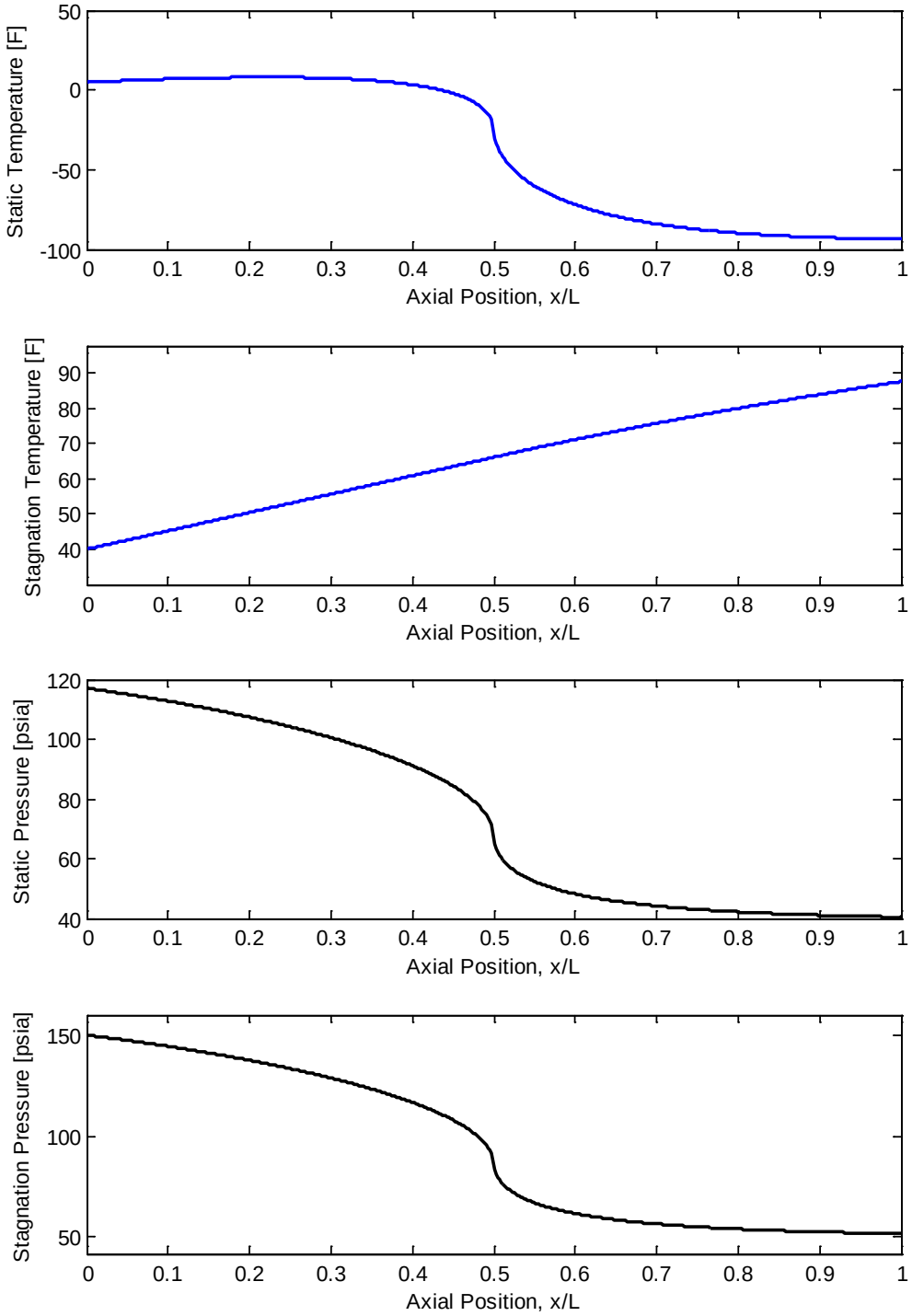

Figure 29: Diverging Nozzle Temperature and Pressure Distributions

3.5.2 Entropy Characteristics

The entropic characteristics of the diverging-area case are very informative of the frictional and heat transfer effects taking place in the nozzle. As discussed previously, Fanno flow effects drive the T-S curve downward on the temperature axis for both subsonic and supersonic flow, while Rayleigh flow effects, in the form of heat addition, drives the curve upward along the temperature axis for subsonic and supersonic flows. Given this general behavior associated with frictional and heat transfer effects, the T-S curve in Figure 30 may be interpreted to inform the energy state of the nozzle.

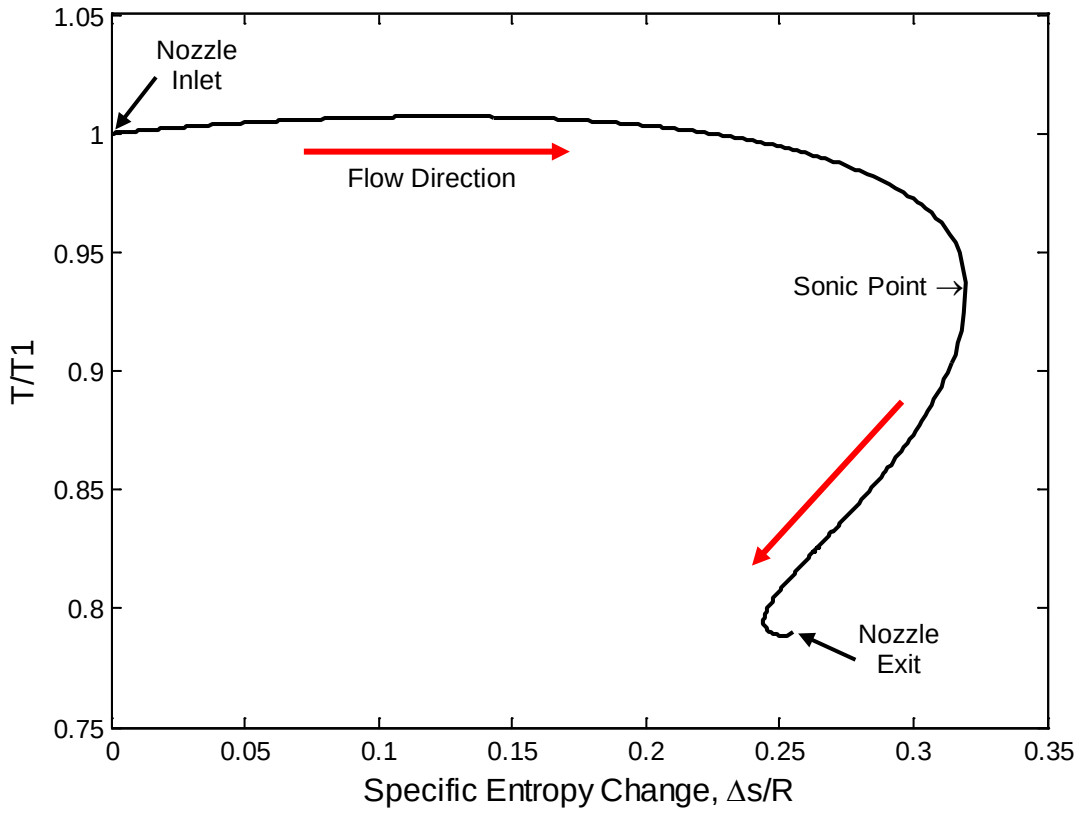

Figure 30: Diverging Nozzle Flow Energy

It may be observed that the majority of the energy curve is nearly the form of a Fanno flow line, such as in Figure 8. This establishes this nozzle case to be primarily driven by frictional effects, rather than heat addition. The general flow physics agree with this, given the significant cooling

of the gas due to expansion, which limits the temperature rise of the flow. The slight climb in the temperature contribution on the leading portion of the curve demonstrates some noticeable addition of heat to the flow in the first half of the nozzle. The latter half of the curve follows the general form of the supersonic portion of the Rayleigh and Fanno line distributions. This confirms that both friction and heat transfer effects are being overcome by supersonic flow. The very last portion of the curve demonstrates a quite interesting phenomenon taking place in near the exit of the nozzle. As discussed in Chapter 2, friction and heat addition always work to drive the flow condition to sonic conditions. In other words, subsonic flow or supersonic flow with added friction and heat addition will eventually be forced to a sonic Mach number condition. In this case, the reversal of the T-S curve back toward increasing entropy and temperature demonstrates the effects of friction and heat addition to drive the flow back to another sonic condition. The now supersonic flow near the exit of the nozzle is beginning to be reduced back toward the direction of sonic and subsonic flow by the friction and heat transfer occurring in the nozzle. If greater values of heat and friction (channel roughness) were added to the flow regime, the velocity of the gas would eventually be brought back to a sonic condition and, if continued, subsonic flow.

Chapter 4. Experimental Demonstration

In order to validate the accuracy of the numerical model in predicting the gas dynamics of varying nozzles designs, an experimental demonstration has been designed. Three physical nozzle geometries equivalent to those previously employed in the model (Fanno-Rayleigh, converging-area, diverging-area) were fabricated, and nitrogen was flown through each to simulate the compressible gas flow. In each experiment, a large, uniform heat source was applied to simulate heat addition to the flow field. The wall roughness and resulting wall temperature were also measured and used as inputs to the numerical model. The resulting axial static temperatures and static pressures in the flow were compared to those values predicted by the model, exhibiting the validity of the model. The following sections provide an overview of the test apparatus used to evaluate each nozzle design, including a description of the measurement methods employed.

4.1 Description of Test Apparatus

4.1.1 System Overview

In order to induce the desired high-velocity gas flow through the nozzles, a gas supply with a significant pressure head is required. A bank of 12 high-capacity nitrogen bottles was selected due to sufficient mass supply at 2400 psi. A needle valve was placed in the supply line between the nitrogen bank and the nozzle test section in order to modulate the inlet pressure to the nozzle as the gas was blown down from high pressure. The exit flow of the nozzle was exhausted to atmospheric pressure (approximately 14.2 psia), which served as a sufficiently low back pressure for the nozzle to reach a steady choked condition. A general schematic of the test apparatus is given in Figure 31, followed by a photograph of the actual physical testing system in Figure 32.

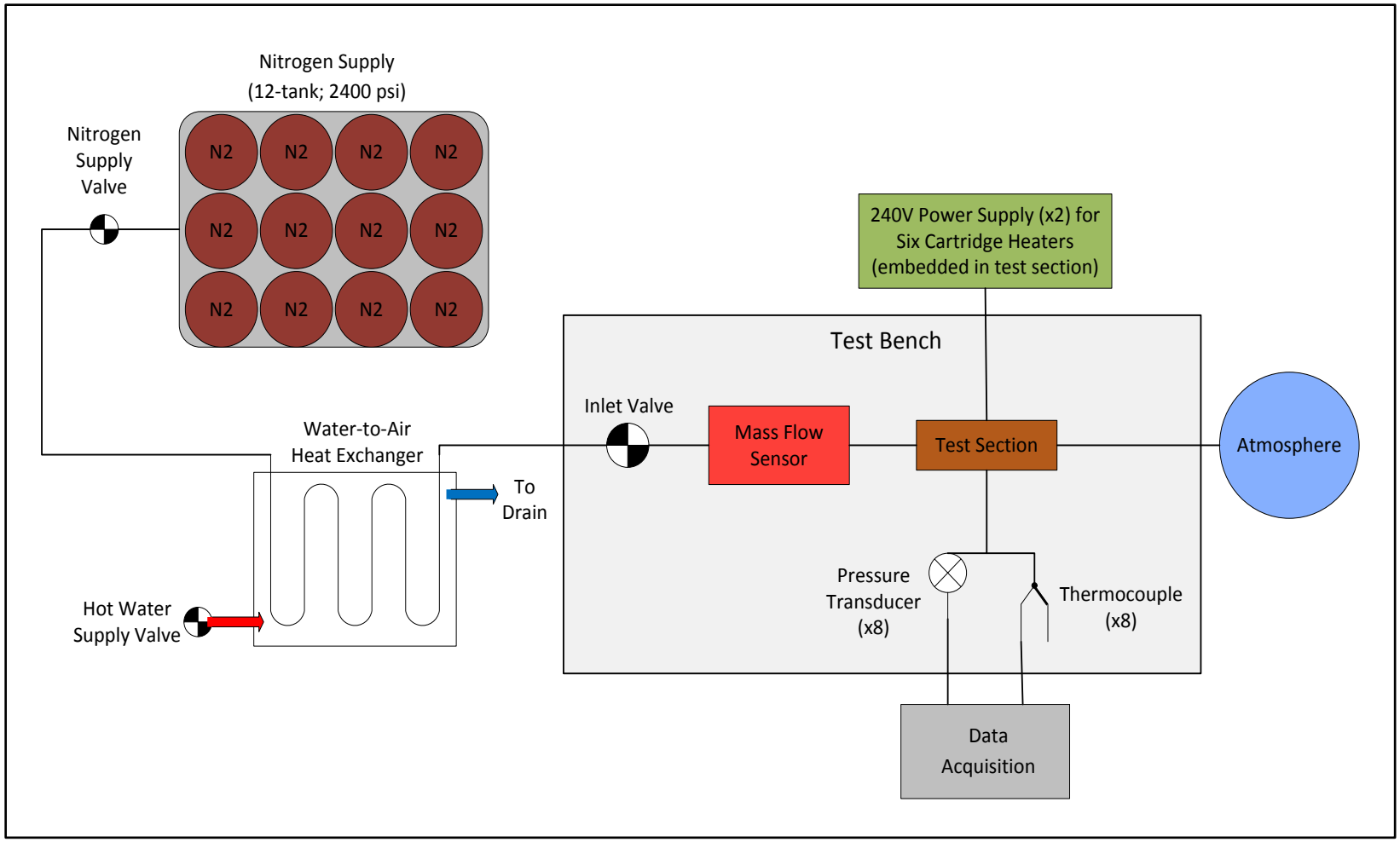

Figure 31: Experimental Test Apparatus Schematic

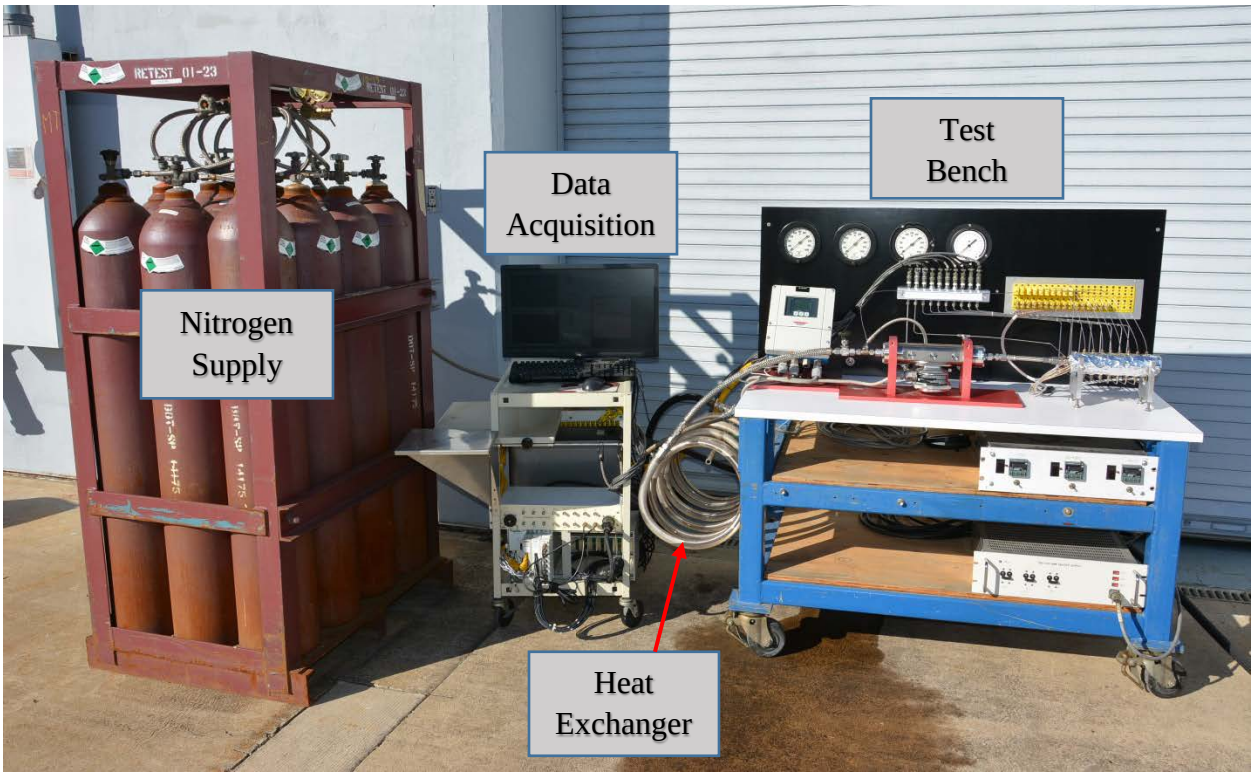

Figure 32: Physical Setup of Experimental Test Apparatus

Take note that a water-to-air heat exchanger precedes the inlet of the test section on the apparatus. This was implemented in order to abate the fluctuation in inlet temperature due to the blowdown from the high-pressure nitrogen supply. The temperature drop during the blowdown process is not constant with time; the inlet temperature of the gas continues to decrease during each test run. This presents a major problem since the numerical model predictions are constructed for steady-state conditions with constant boundary conditions. Without this correction, the experimental model could not be legitimately compared to the numerical model. Implementation of the heat exchanger solved this issue by producing a steady inlet temperature (approx. 70˚F) that was significantly warmer than the prior inlet temperature range (0-15˚F).

4.1.2 Test Sections

As stated above, three test sections were fabricated for each nozzle geometry. In order to ensure sufficient, uniform heat transfer through the test section and into the flow-field, copper was selected for the nozzle material because of its high thermal conductivity. The specific alloy, C145 (copper tellurium), was chosen due to its superior machinability with a small sacrifice in conductivity (k_{C145} = 232 [BTU/ft·h·ºF]) from that of pure copper.

Each copper test section was machined to a 2-inch outer diameter with six 3/8-inch thru holes along the 8-1/2 inch length. These holes are axisymmetric about the center thru hole, which serves as the nozzle bore. They are designed to house 3/8 diameter, 240 Volt stainless steel cartridge heaters (Omega HDC00393), which serve as the generation of heat transfer to the nozzle bore. The cartridge heaters are rated to 1000 Watts and are temperature controlled to ensure overheating of the test section is prevented. The test setup was designed to simulate a uniform heat flux along the nozzle bore, as simulated in the previous model examples. Ideally, the entire bore surface would experience a uniform heat flux from the symmetric distribution of equally powered heaters. However, the channel is more likely to experience constant temperature due to the high conductivity of the copper material. By design, the copper test section assembly is insulated on the exterior to ensure that the majority of heat provided by the heaters is sunk in the direction of the nozzle bore. This would work for the theoretical case of perfect insulation and no heat loss to the exterior, but this is unrealistic for the actual experiment. Because of multiple modes of heat distribution errors (radiation heat loss, uneven conduction, uninsulated test section ends, etc.), the wall temperatures were used as data inputs to the model code, rather than assuming a perfectly uniform heat flux. The nozzle bore geometries were machined using custom tooling to the same geometries specified by the numerical model. The

machined surface finish was specified to a standard $63x10^{-6}$ inches, and validated by stylus profilometer measurement of a separate test sample.

A cross-sectional drawing of the nozzle geometry for each test section is displayed in Figure 33.

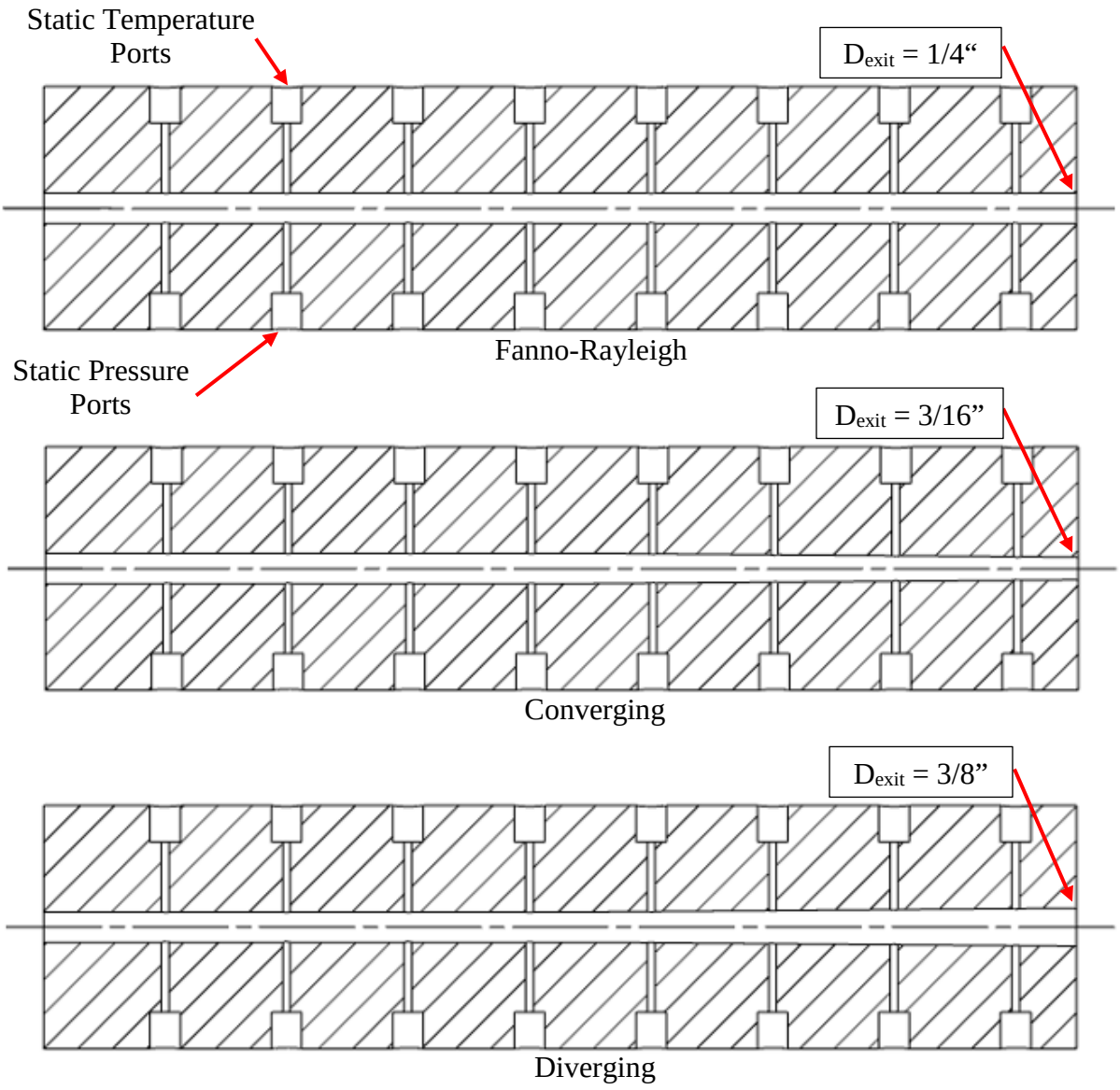

Figure 33: Cross-Section View of Nozzle Bore for Each Test Section

As discussed in section 3.2, each nozzle was scaled such that it meets the criterion of the fully developed condition for turbulent flow. Since the inlet Reynolds Number is greater than $1x10^4$

for all cases, demonstrating turbulent flow conditions, Equation 4.1 confirms fully developed flow for the nominal diameter of each nozzle.

$$\frac{L}{D} = \frac{8.0 \text{ in}}{0.25 \text{ in}} = 32 \gtrsim 10 \tag{4.1}$$

Furthermore, the tube fitting connected at the inlet of each nozzle was machined to the same bore diameter (0.25 inches) as the first section of the nozzle.

For further detail, the actual machined Fanno-Rayleigh nozzle test section is pictured in Figure 34. Note that the nozzle exit side is being viewed, while the secondary wall thermocouples (opposite side) and static pressure ports (bottom side) are not visible.

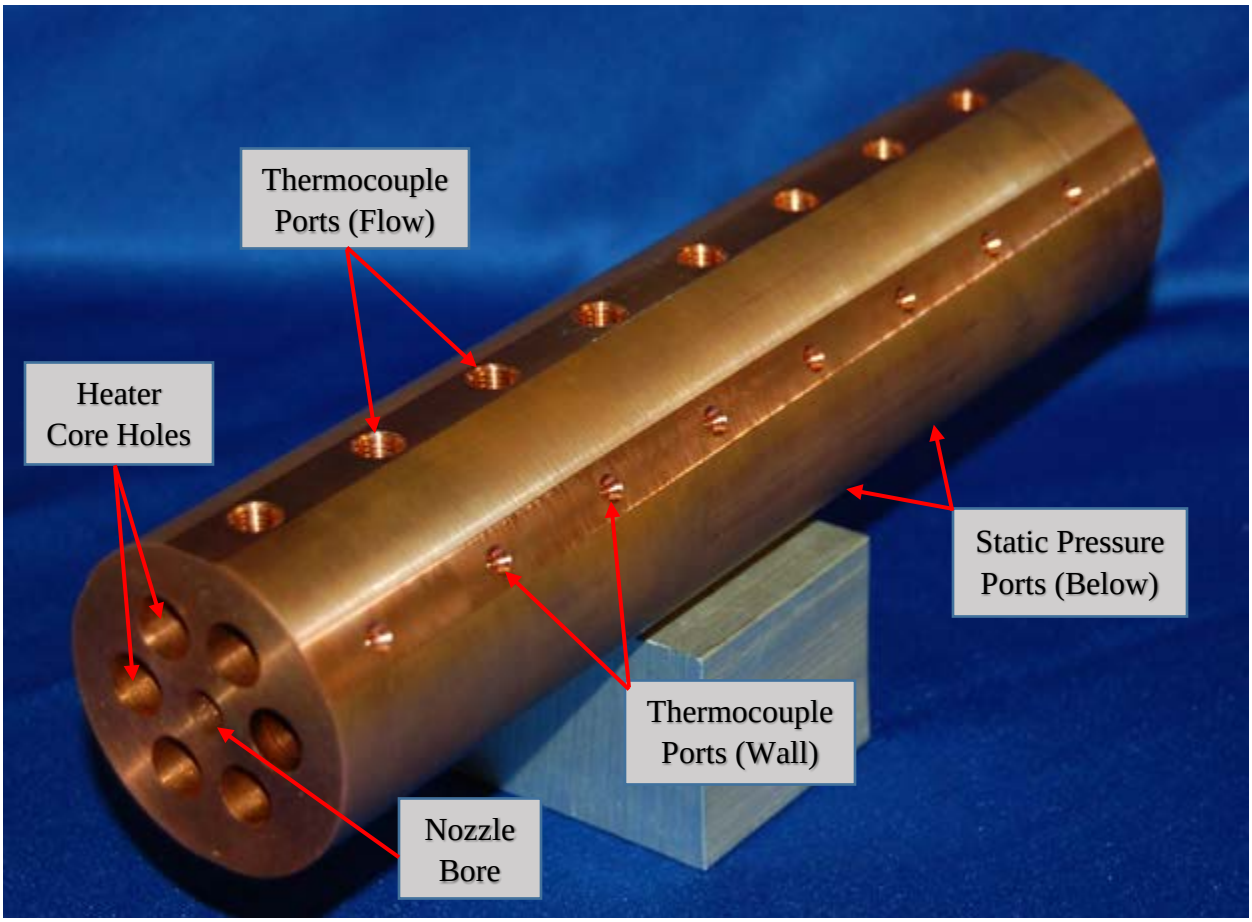

Figure 34: Fanno-Rayleigh Nozzle Copper Test Section

A total of four 8-hole arrays were drilled radially along each test section for temperature and pressure instrumentation around the center nozzle bore. The two side arrays housed glass-insulated thermocouples taking temperature measurements within1/16th inch of the bore to approximate the nozzle wall temperature. The array directly on top of the test section housed thermocouple probes that extend to the center axis of the nozzle bore to extract mean flow temperatures (probe area ≈ 1.43% of bore cross-sectional area). Finally, the bottom array housed tubing for static pressure measurements in the flow. A cross-sectional schematic of this instrumentation that exists at each axial location is displayed in Figure 35.

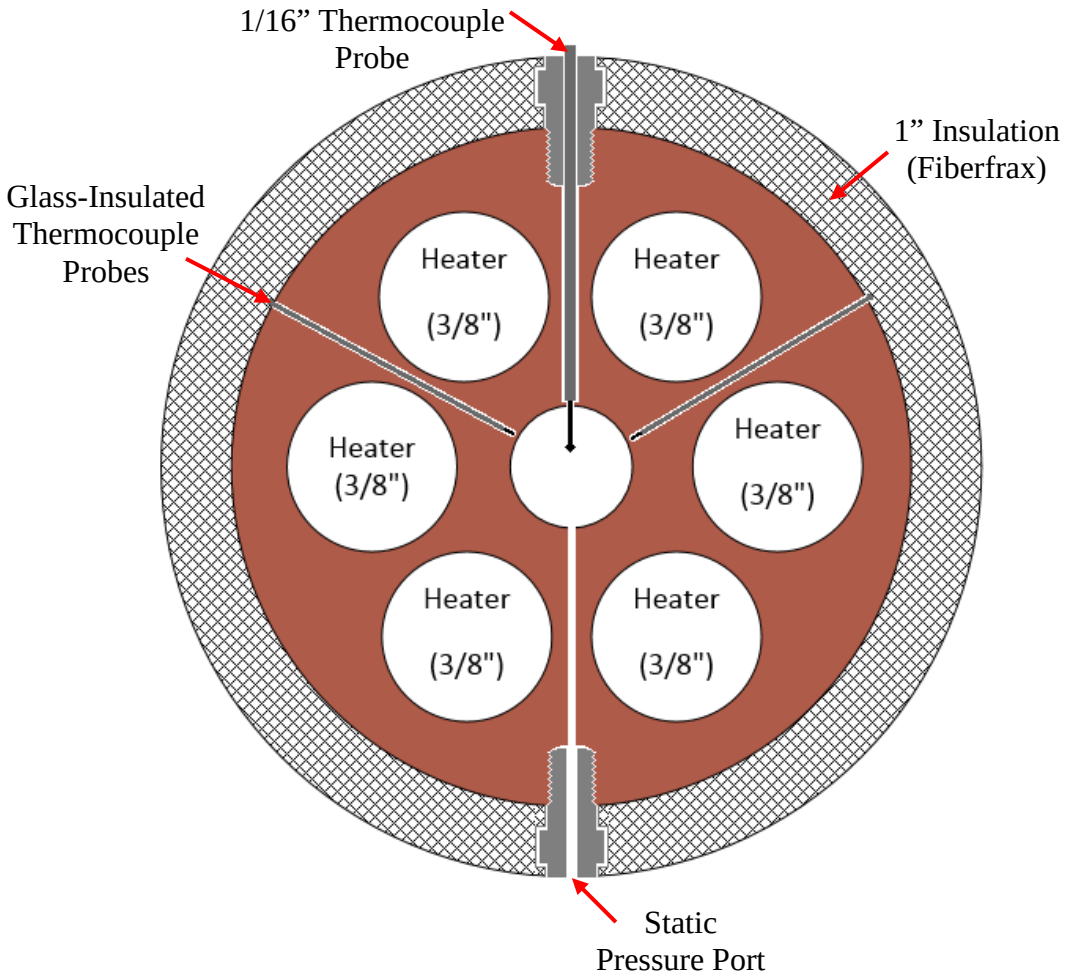

Figure 35: Cross-Sectional Schematic of Test Sections

4.1.3 Instrumentation

A test bench was constructed as a platform to support instrumentation for acquisition of the desired data. All temperature, pressure, and mass-flow measurements were taken by a National Instruments (NI) data system using LabVIEW®. A tabulated figure of the instrumentation components is displayed below in Figure 36. Note that analog pressure gages were included for monitoring several locations in the flow around the mass flow sensor and test sections to help ensure proper pressurization at these points.

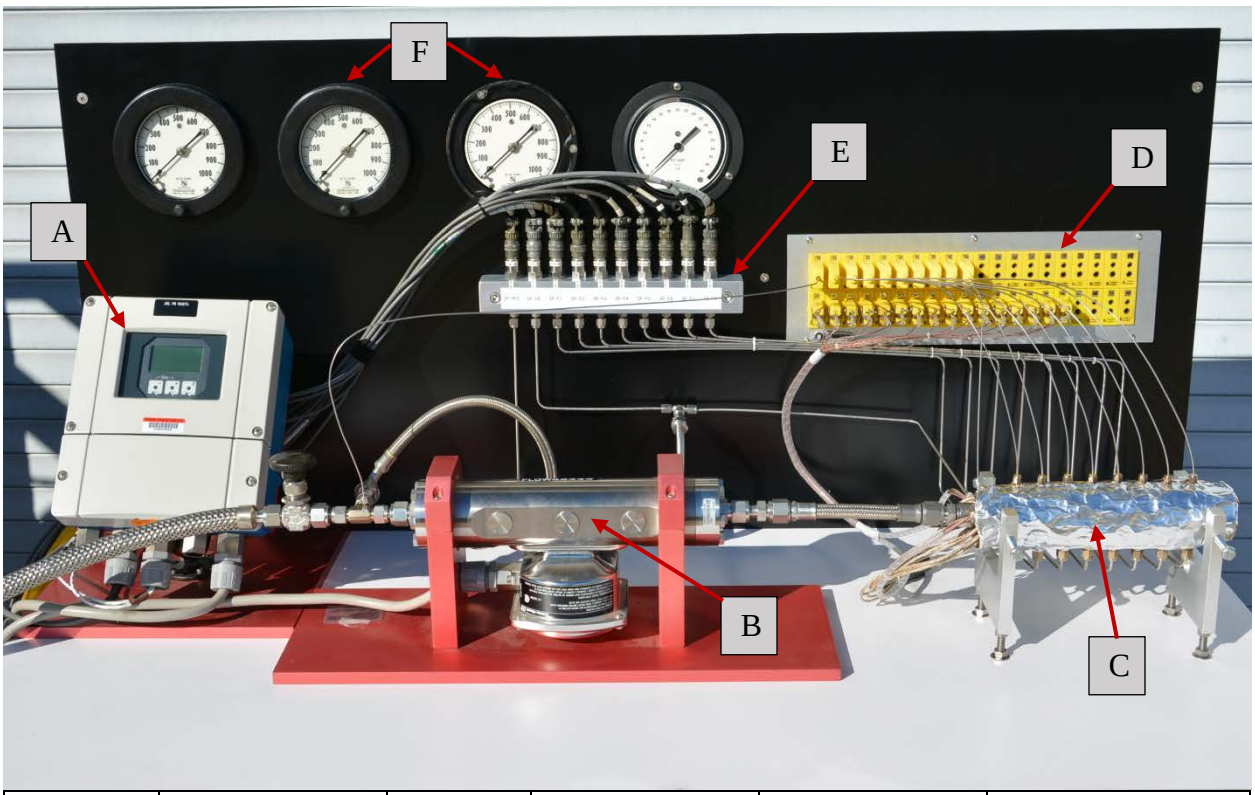

MFS Display	Mass Flow Sensor (MFS)	Test Section	Thermocouple Board	Transducer Block	Safety Pressure Gauges
A	B	C	D	E	F

Figure 36: Instrumentation and Test Section

Also note that the mass flow sensor display was used to calibrate the meter to the expected range of flow and to corroborate the values read by the NI data system. The mass flow sensor is an

Endress-Hauser Promass 83 Coriolis flowmeter; it employs the Coriolis Effect in measuring the density and velocity of a moving gas. Although mass flow was not a primary parameter evaluated in this study, the mass flow measurement served as an additional validation of the primary measurements, static pressure and temperature.

Figure 37 displays the detailed configuration of the test section once it was positioned in the test apparatus. Note the location of the inlet pressure and temperature probes which were used to implement the set points for test control. For more detail on how instrumentation was employed in this experiment, a detailed procedure may be found in Appendix B.

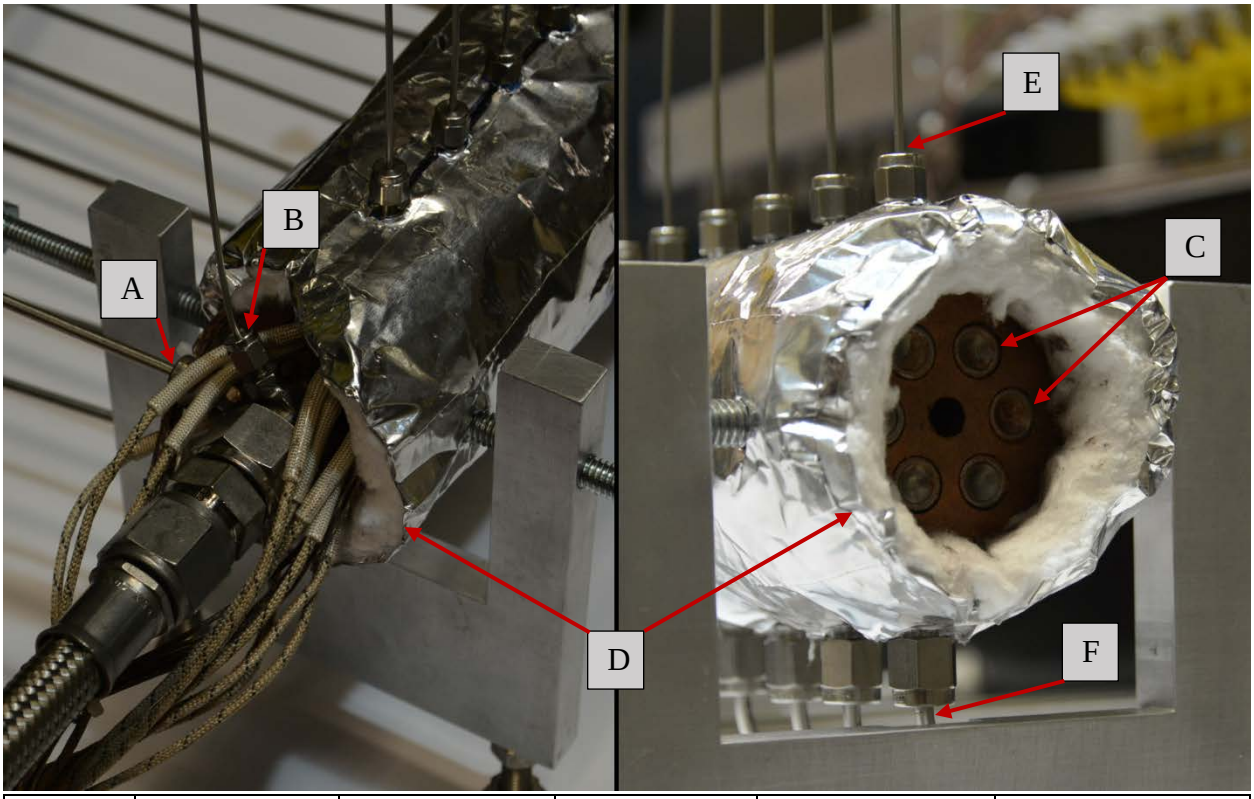

Inlet Static P	Inlet Stagnation T	3/8” Cartridge Heaters	Fiberfrax® Insulation	Thermocouple Probes (Flow)	Static Pressure Lines
A	B	C	D	E	F

Figure 37: Test Section Setup

Chapter 5. Presentation and Discussion of Results

Once each nozzle test was complete, a sample of the collected data was taken from where steady-state conditions were observed. This was done by plotting the wall and flow temperatures over the runtime of the test and surveying where all the lines reached an asymptote. For each nozzle test, steady temperature conditions were achieved when the thermocouple-controlled cartridge heaters reached their set point (1000 °F). This occurred after approximately two minutes for each nozzle test, after which point any set of data in the test run is valid for steady-state analysis.

In order to best compare the experimental data to the numerical model results for the same conditions, the static wall temperatures were used as inputs in the code. This was accomplished by extracting the equation from a polynomial fit of the data and implementing it in the numerical model. With these temperature inputs, as well as the inlet temperature and pressure, the subsequent heat transfer and resulting thermodynamic state of the nozzle was solved. After this, the measured experimental temperature and pressure data were plotted with the corresponding numerical model results on the same chart. The following sections display and interpret the results of each nozzle test.

5.1 Data Analysis

In order to draw appropriate conclusions from the experimental data, it is necessary to understand, what physical quantity is being measured and the uncertainty that is associated with each measurement. In the case of this experiment, the wall temperatures and the flow temperatures and pressures are the critical measurements to evaluate.

The wall temperatures may be treated as static or total temperatures, since they are in a quiescent environment and do not experience any of the flow, directly. Under such conditions, static and stagnation temperatures are the same. For this reason, the measured values may be used directly, with any correction factor.

Similar to the wall temperature data, the pressure data may be treated as static pressure. This is due to the orientation of the pressure ports being orthogonal with respect to the flow direction; they measure the pressure of the flow field without effecting the flow velocity. If oriented parallel, and in the opposite direction, to the flow, the flow would be brought to rest at the measurement location and may be considered stagnation (total) pressure. This is the methodology employed by pitot-static probes in measuring the total pressure directly within a flow field. Since the pressure ports are located in the nozzle wall, they are simply measuring static pressure.

Unlike the wall temperatures and pressures, the mean flow temperatures require more consideration. Since the measurement location is directly in a high-velocity flow field, the static and stagnation temperature may not be considered equivalent. The precise point of measurement exists at the surface of the junction of the thermocouple probe, which consists of a spherical bead with a nominal diameter measuring approximately 0.010 inches. As the flow comes into contact with the probe, it is forced to stagnate on its surface, due to the no-slip flow boundary condition. Theoretically, the thermocouple absorbs the full energy of the flow and, as a result, measures stagnation temperature. In reality, however, other sources of energy contribute to the temperature actually measured at the bead. Figure 38 displays a schematic of the thermocouple bead in the nozzle flow and displays the energy balance taking place within a control volume around the bead.

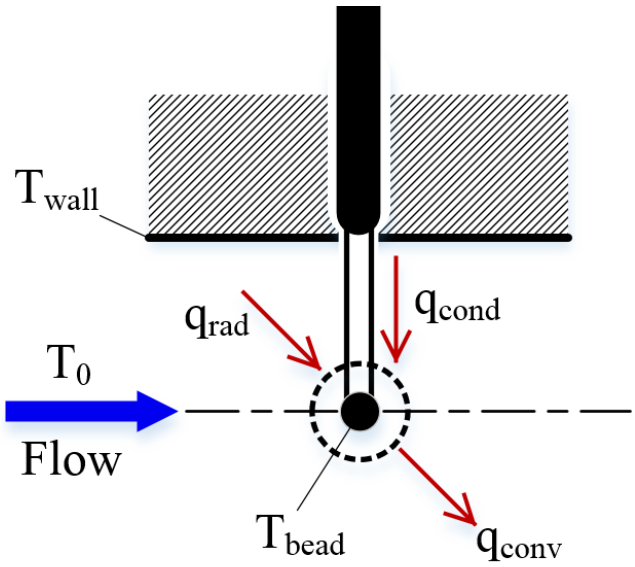

Figure 38: Thermocouple Energy Balance

Starting with the classical thermal equation (5.1), an energy balance may be performed on the thermocouple probe.

$$\dot{E}_{stored} = \dot{E}_{in} - \dot{E}_{out} + \dot{E}_{generated} \tag{5.1}$$

Recognizing that the primary modes of heat transfer are radiation from the heated nozzle wall, conduction through the thermocouple probe wires into the bead, and convective cooling from the gas flow, the energy balance may be reduced to Equation (5.2) and subsequently substituted with the definitions for each mode of heat transfer (Equation 5.3),

$$q_{convection} = q_{conduction} + q_{radiation} \tag{5.2}$$

$$hA_{bead}(T_o - T_{bead}) = -k_{wire}A_{wire}(T_{wall} - T_{bead}) + \epsilon_{bead}\sigma A_{bead}\left(T_{wall}^4 - T_{bead}^4\right) \tag{5.3}$$

where $k_{wire} = 14.2\ [BTU/ft \cdot hr \cdot °F]$, $A_{wire} = 1.26x10^{-5}\ [in^2]$, $\epsilon_{bead} = 0.35$, and $A_{bead} = 3.14x10^{-4}\ [in^2]$.

Additionally, Equation 5.3 may be rearranged to solve for the parameter of interest, the actual stagnation temperature of the gas flow.

$$T_o = \frac{[-k_{wire}A_{wire}(T_{wall}-T_{bead})+ \epsilon\sigma A_{bead}(T_{wall}^4-T_{bead}^4)]}{hA_{bead}} + T_{bead} \quad (5.4)$$

The value of the convection coefficient, h, must be estimated in order to approximate the convective heat transfer from the thermocouple bead. This may be accomplished by employing the appropriate correlation for flow over a spherical body, given in Equation 5.5 [20],

$$\overline{Nu}_D = \frac{hD}{k_f} = 430 + 5 \times 10^{-3} Re_D + 0.25 \times 10^{-9} Re_D^2 - 3.1 \times 10^{-17} Re_D^3 \quad (5.5)$$

where $k_f = 0.0159$ [$BTU/ft \cdot hr \cdot$ °F].

The resulting values of Equation 5.4 are used as the experimental data for each of the temperature plots in this section. This ensures that the experimental values may be compared to the model predictions for stagnation temperature through the model.

As previously stated, determining the uncertainty associated with each measurement is crucial for drawing appropriate conclusions from the data. Once defined, the uncertainty provides the range that may be considered for the actual value of any given measurement. Applying a standard 95% confidence in the random distribution of the data, the uncertainty for any measurement may be determined by Moffat's relationship for multi-sample analyses (Equation 5.5) [21]:

$$U_{0.95} = \sqrt{(B_{X_i})^2 + (t \cdot S_{\overline{X_i}})^2} \quad (5.5)$$

where B_{X_i} is the bias limit for the i*th* measurement, $S_{\overline{X_i}}$ is the precision index of the mean i*th* measurement, and t is the Student's t multiplier for 95% confidence and the number of sample

measurements. The bias limit is determined by the manufacturer's error tolerance for the measurement instrument, while the precision index is obtained by Equation 5.6 [21]:

$$S_{\overline{X_i}} = \frac{\sigma}{\sqrt{N}} \tag{5.6}$$

where σ is the standard deviation of each measurement in a data set and N is the number of data sets. The uncertainty of each measurement was determined for every set of wall temperature and flow temperature and pressure data and is displayed as error bars on each data figure in the following sections.

5.2 Fanno-Rayleigh Test Results

The results of the constant channel area, or Fanno-Rayleigh, nozzle are significant in that they serve as the baseline analysis for each test. The data of the succeeding tests (converging, diverging) are contrasted with the basic results presented here. Including this test as a baseline permits the observation of different flow dynamics and heat transfer that occur due to variation of the primary parameter, that is, channel area. In order to better identify the real physical state of every nozzle, it is advantageous to evaluate the primary quantities associated with each; namely, the measured inlet parameters and overall changes through the nozzle. Table 5 displays these measured parameters and the principal quantities that may be estimated from them.

Table 5: Fanno-Rayleigh Experimentally Measured and Estimated Quantities

Measured Quanitites	
Mass Flow	$\dot{m} \approx 445$ [lb_m/hr] (0.056 kg/s)
Inlet Stagnation Temperature	$T_{0,\,Inlet} \approx 70$ [℉] (294 K)
Exit Stagnation Temperature	$T_{0,\,Exit} \approx 200$ [℉] (366 K)
Inlet Static Pressure	$P_{Inlet} \approx 120$ [psia] (827 kPa)
Estimated Quantities	
Fluid Density	$\rho_{Inlet} = 0.741$ [lb_m/ft^3] (11.9 kg/m^3)
Fluid Dynamic Viscosity	$\mu = 1.193 \times 10^{-5}$ [lb_m/ft*s] (1.76×10^{-5} Pa*s)
Inlet Mean Velocity	$V_{Inlet} \approx 489$ [ft/s] (149 m/s)
Inlet Stagnation Pressure	$P_{0,\,Inlet} \approx 135.8$ [psia] (936 kPa)
Total Heat Addition to Channel over Nozzle Length	$Q_{Nozzle} \approx 1.462 \times 10^4$ [BTU/hr] (4285 W)
Inlet Reynolds Number	$Re_D \approx 3.711 \times 10^5$

It may be noted that, although the inlet static pressure was fixed during each test to produce a stagnation pressure of approximately 150 psia, this is not precisely the case. Supplementary evaluation of the measured mass flow and inlet static pressure gives a closer estimate of the actual stagnation pressure at the inlet of the nozzle. This is accomplished via Equation 5.7 and 5.8 by using the fluid properties at the inlet pressure and temperature.

$$\dot{m} = \rho A V \rightarrow V = \frac{\dot{m}}{\rho A} \tag{5.7}$$

$$P_{0,Inlet} = P_{Inlet}\left(1 + \frac{\gamma}{2}M^2\right)^{\frac{\gamma}{\gamma-1}} = P_{Inlet}\left(1 + \frac{\gamma}{2}\left(\frac{V}{C}\right)^2\right)^{\frac{\gamma}{\gamma-1}} \tag{5.8}$$

In order to best compare the results of each test to the model predictions, this estimated pressure was used as the inlet condition in the model code. The remaining quantities in Table 5 may be used to better understand the approximate flow and heat transfer conditions of the nozzle.

Specifically, the Reynolds number estimate serves to evaluate whether or not the flow is turbulent, while the bulk heat addition to the nozzle bore estimates the total heat transferred from the cartridge heaters to the flow field.

$$Re_D = \frac{\rho V D}{\mu} \tag{5.9}$$

$$Q_{Nozzle} = \dot{m} c_p (T_{0,Exit} - T_{0,Inlet}) \tag{5.10}$$

The steady-state wall temperature data from the Fanno-Rayleigh test is given in Figure 39. A second-order polynomial curve was fit to the data in order that the trend of the eight temperature measurements might be more finely discretized as an input to the model. This was done to ensure that the model converged more easily and produced results of greater precision. Take note that the fit curve is well-matched to the data as demonstrated by an R^2 value very near unity.

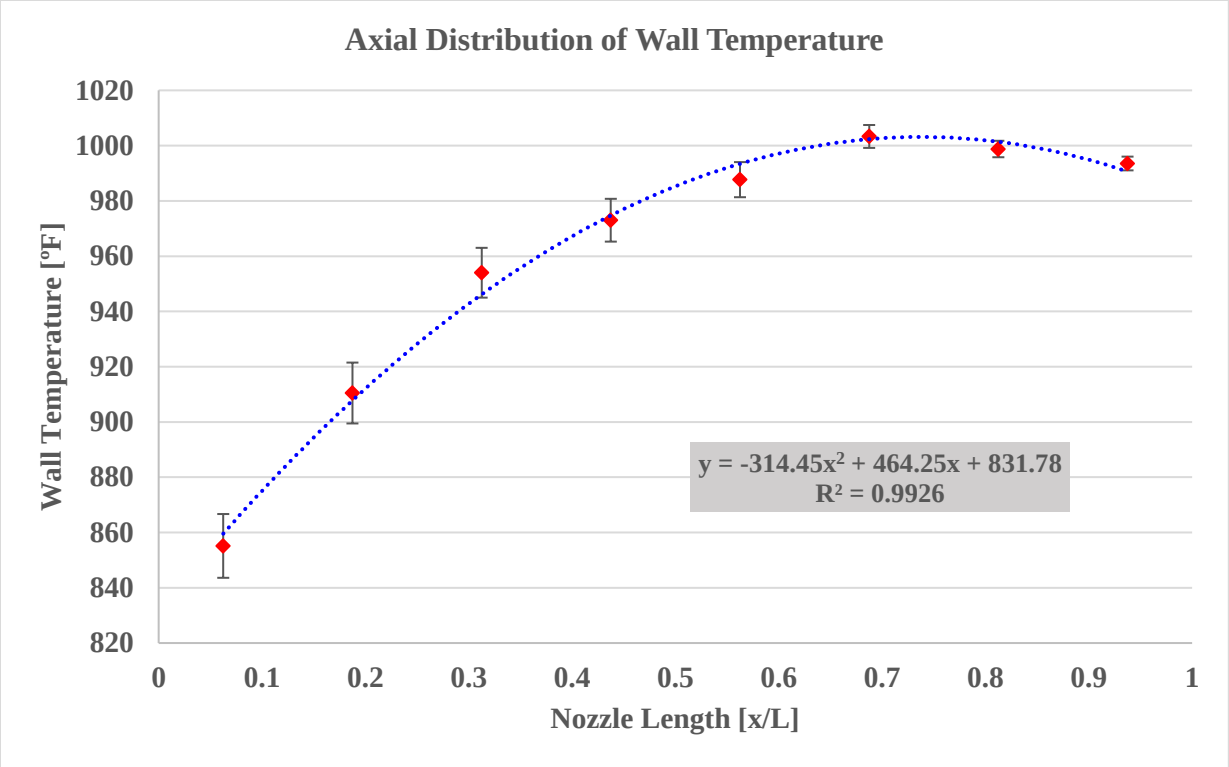

Figure 39: Fanno-Rayleigh Nozzle Wall Temperature Distribution

Also note the general trend of increasing temperature through the majority of the nozzle, followed by a slight decreasing trend near the exit. This is likely due to increasing flow temperatures that result from heat transfer from the wall to the flow. As the flow temperature increases, the temperature difference between the flow and the wall is reduced, and lower cooling of the wall takes place, demonstrating the observed overall trend. As for the latter end of the curve, the decreasing trend of the wall temperature is likely due to the rapid expansion of the gas as it approaches the exit plane. In other words, the temperature drop due to the expansion of the gas outweighs the heating of the gas from the wall, resulting in greater wall cooling near the exit.

The model-predicted static pressure and stagnation temperature through the nozzle are plotted on top of the data points in Figure 40 and 41, respectively. It may be readily observed that,

according to the data, the numerical model is an accurate predictor of pressure for the given Fanno-Rayleigh nozzle case. The slight offset of the predicted curve may be due to a difference between the inlet stagnation pressure input in the model and the actual experimental value at that location. Since the inlet stagnation pressure is not directly measured experimentally (Ex. Pitot-static probe), it is estimated by the measured mass flow and static pressure at the nozzle inlet. The actual stagnation pressure at the inlet of the nozzle may differ from this prediction, resulting in the lower experimental values. If the stagnation pressure is adjusted, the model curve will fall more precisely on the experimental data.

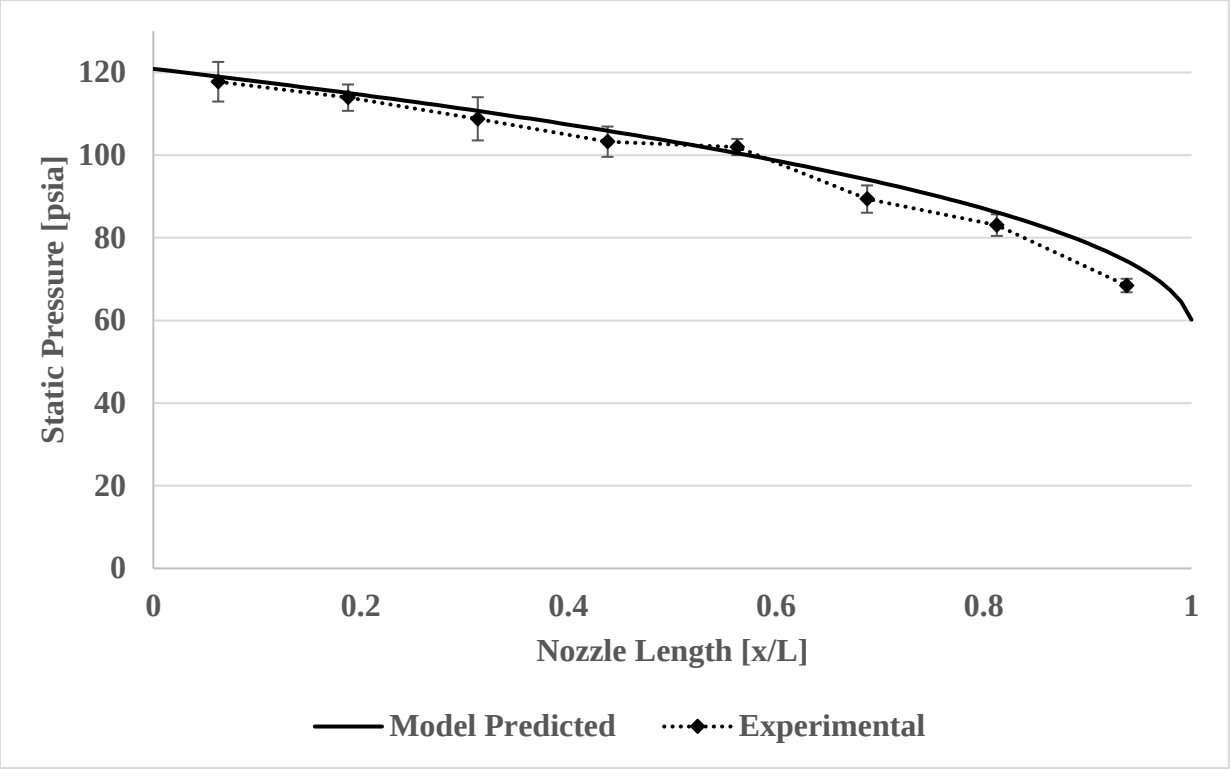

Figure 40: Fanno-Rayleigh Nozzle Static Pressure Distribution

The mean stagnation temperature was not accurately predicted as was the static pressure. Although the overall increasing trend and order-of-magnitude values agreed, the model underpredicted flow temperature toward the inlet and overpredicted values in the latter portion of

the nozzle. A likely source of this poor prediction is the instrumentation of thermocouples measuring flow temperature. Since the model employs a quasi-one dimensional analysis, it solves for a mean temperature at any location in the nozzle channel. In reality, the flow temperatures should have a mostly uniform distribution through the bulk cross section of the channel, with a larger gradient toward higher temperatures near the wall. Due to the relatively small scale of the channel area, any variation in thermocouple position in the flow may have significant effects. Since the emperimental temperatures do not produce the expected smooth distribution, it is likely that this instrumentation is the source of the significant difference from predicted values.

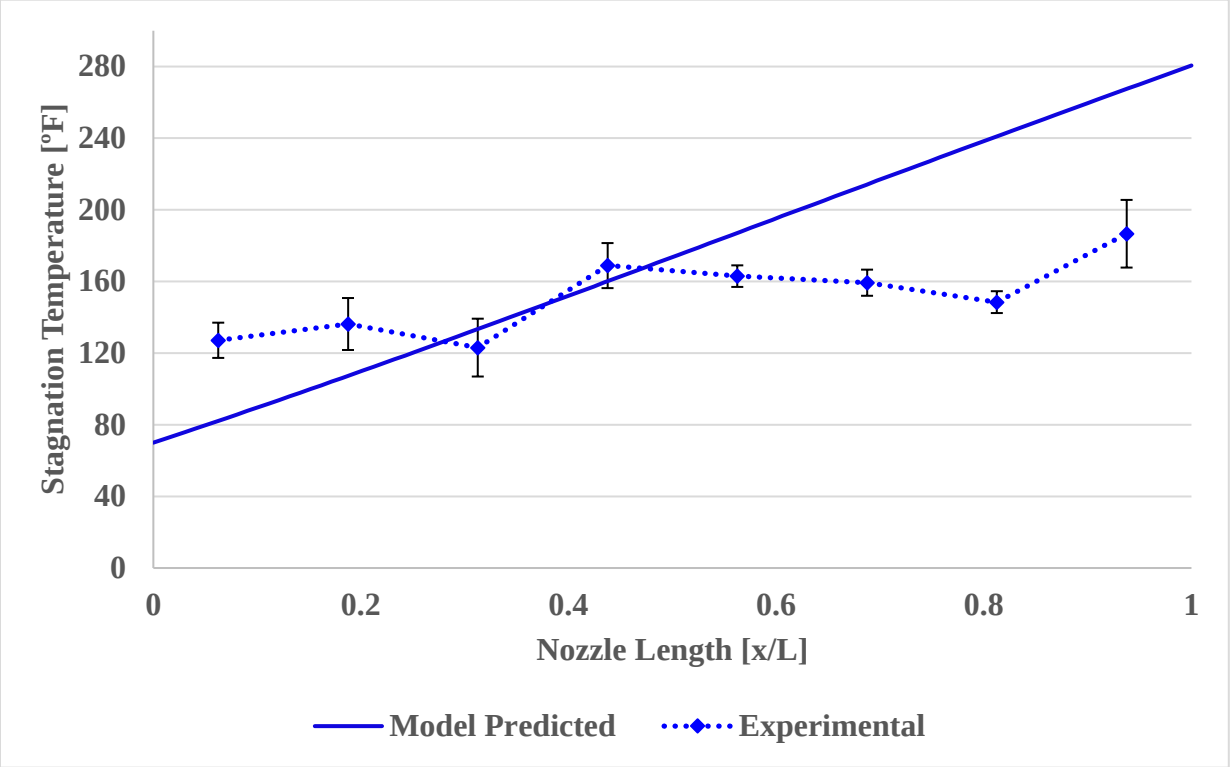

Figure 41: Fanno-Rayleigh Nozzle Mean Flow Stagnation Temperature Distribution

5.2 Converging-Area Model

As with the Fanno-Rayleigh nozzle, the key experimental measurements from the converging nozzle tests were used to estimate the over-all state of the nozzle. It may be noted that these parameters are changed significantly from the previous case, even though the measured static pressure just prior to the nozzle inlet was set to the same value (150 psia) and all other primary test settings remained the same (heater temperature set point, hardware configuration, etc.). This demonstrates that a change in nozzle geometry has a significant effect on the flow and heat transfer dynamics for the same general conditions. A summary of these measurements and subsequent estimates is given in Table 6.

Table 6: Converging Nozzle Experimentally Measured and Estimated Quantities

Measured Quanitites	
Mass Flow	$\dot{m}$ = 317 [lb_m/hr] (0.040 kg/s)
Inlet Stagnation Temperature	$T_{0,\ Inlet} \approx 70$ [°F] (294 K)
Exit Stagnation Temperature	$T_{0,\ Exit} \approx 300$ [°F] (422 K)
Inlet Static Pressure	$P_{Inlet} \approx 145$ [psia] (1000 kPa)
Estimated Quantities	
Fluid Density (Nitrogen @ $T_{o,\ Inlet}/P_{Inlet}$)	ρ_{Inlet} = 0.716 [lb_m/ft^3] (11.5 kg/m^3)
Fluid Dynamic Viscosity	μ = 1.195 x 10^{-5} [lb_m/ft*s] (1.78x10^{-5} Pa*s)
Inlet Mean Velocity	V_{Inlet} = 361 [ft/s] (110 m/s)
Inlet Stagnation Pressure	$P_{0,\ Inlet} \approx 155.2$ [psia] (1070 kPa)
Total Heat Addition to Channel over Nozzle Length	Q_{Nozzle} = 1.842 x 10^4 [BTU/hr] (5399 W)
Inlet Reynolds Number	Re_D = 2.648 x 10^5

The converging nozzle wall temperatures, shown in Figure 42, followed the same overall trend as the Fanno-Rayleigh nozzle. That is, the temperatures steadily increased through the nozzle until the latter portion near the exit, where they began to drop off. One noticeable difference

from the Fanno-Rayleigh distribution is that the temperature decreased more significantly in this latter portion. This may be due to the more rapid expansion of the gas that takes place in the converging area of the nozzle. This larger gradient in pressure (and density) is accompanied by a greater descent in flow temperature, which leads to more cooling of the nozzle wall.

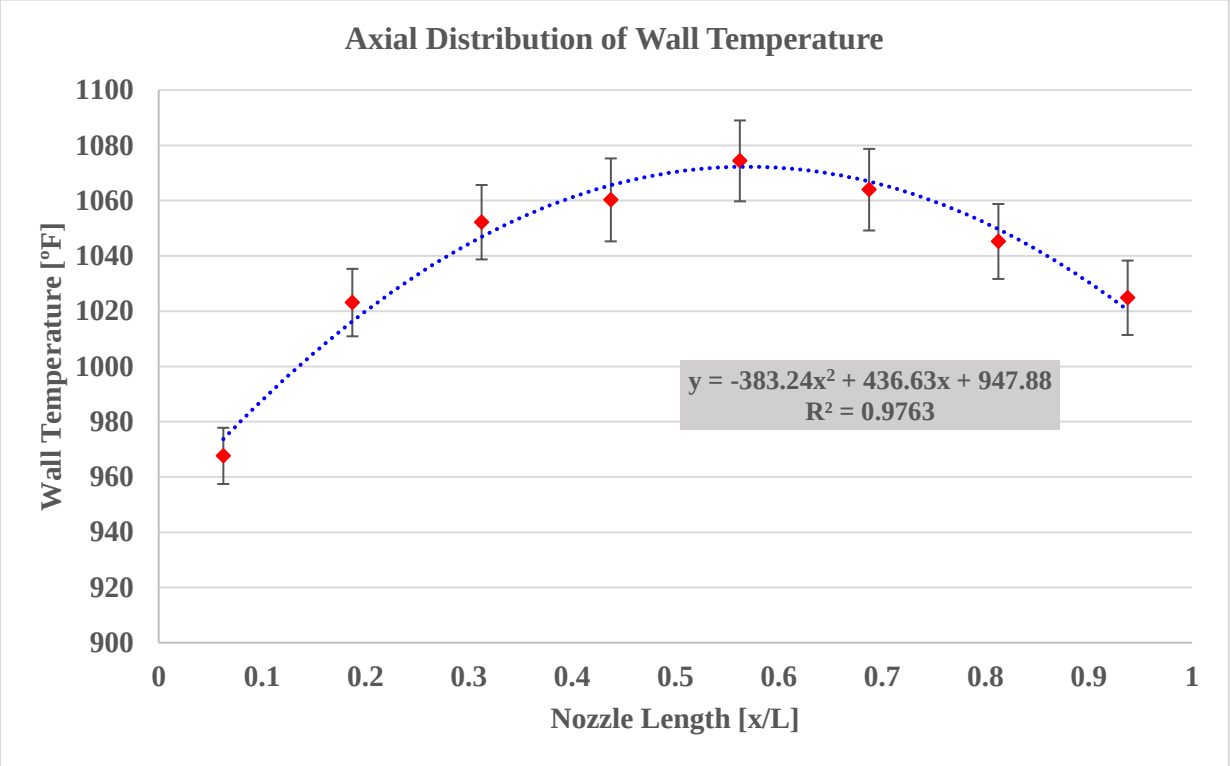

Figure 42: Converging Nozzle Wall Temperature Distribution

Once, again, the numerical model predicted the static pressure distribution in the nozzle with reasonable accuracy, as displayed in Figure 43. The experimental results in this case, however, slightly diverged from the model prediction in the converging section of the nozzle. Take note that the overall trend of the data matches the model, with the final pressures of both model and experiment coming more nearly together. This pressure trend demonstrates that the sharp transition in the nozzle, from constant area to converging, is where the model may start to miscalculate values. It appears that the code may be over-constraining the solution by the rigid

change in geometry, while the actual nozzle flow is more affected, and adjusts more in accordance with, the overall inlet-to-outlet area ratio. In external compressible flow, instantaneous changes in geometry usually coincide with immediate changes in flow properties (Ex. shockwave, expansion fan), whereas, internal compressible flow is analyzed more on the basis of overall geometry and fluid property ratios. Even with this divergence, however, the model still exhibits reasonable forecasting of the measured static pressures along the nozzle.

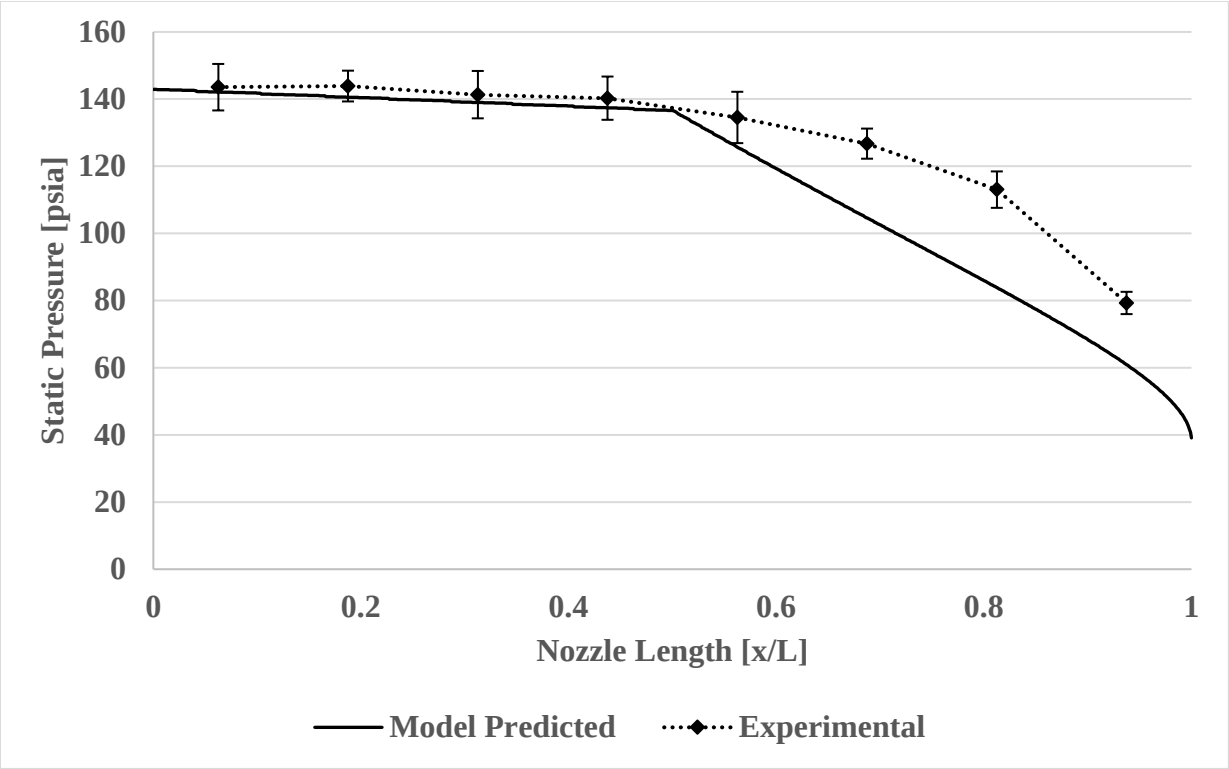

Figure 43: Converging Nozzle Static Pressure Distribution

The experimental stagnation temperature distribution follows the same increasing trend and general values as the model prediction. Unlike the previous case, however, the model prediction more nearly matches the experimental data. As before, the variation of temperature prediction may likely be related to imprecise measurement of the thermocouple probes within the flow regime. The stagnation temperature plot for the converging case is given in Figure 44.

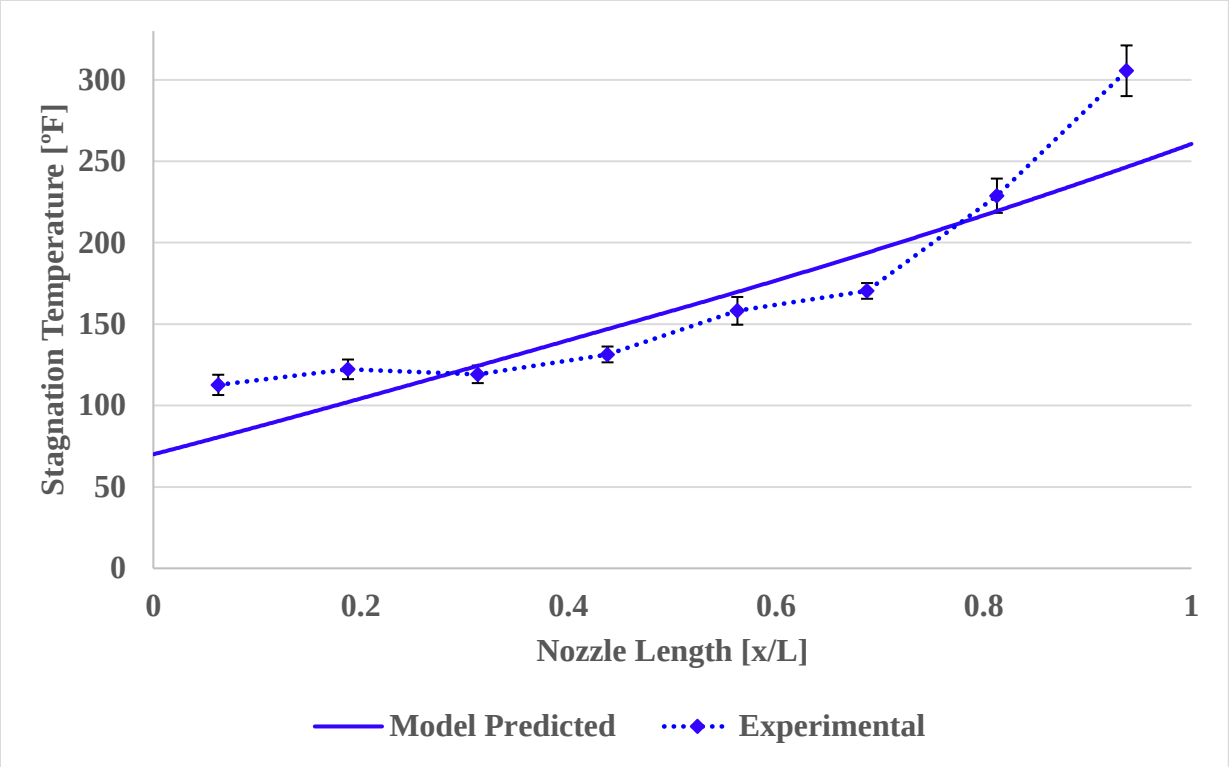

Figure 44: Converging Nozzle Mean Flow Stagnation Temperature Distribution

5.3 Diverging-Area Model

As with the previous cases, experimental measurements from the diverging nozzle tests were used to estimate the general state of the nozzle. It may be noted, once again, that these parameters are changed significantly from the previous cases, even though the other primary test settings remained the same. A summary of these measurements and subsequent estimates is given in Table 7.

Table 7: Diverging Nozzle Experimentally Measured and Estimated Quantities

Measured Quanitites	
Mass Flow	$\dot{m}$ = 584 [lb_m/hr] (0.074 kg/s)
Inlet Stagnation Temperature	$T_{0,\ Inlet} \approx 70$ [°F] (294 K)
Exit Stagnation Temperature	$T_{0,\ Exit} \approx 150$ [°F] (339 K)
Inlet Static Pressure	$P_{Inlet} \approx 115$ [psia] (793 kPa)
Estimated Quantities	
Fluid Density (Nitrogen @ $T_{o,\ Inlet}/P_{Inlet}$)	ρ_{Inlet} = 0.568 [lb_m/ft^3] (9098 kg/m^3)
Fluid Dynamic Viscosity	$\mu = 1.192 \times 10^{-5}$ [lb_m/ft*s] (1.77×10^{-5} Pa*s)
Inlet Mean Velocity	V_{Inlet} = 838 [ft/s] (255 m/s)
Inlet Stagnation Pressure	$P_{0,\ Inlet} \approx 163.5$ [psia] (1127 kPa)
Total Heat Addition to Channel over Nozzle Length	$Q_{Nozzle} = 9.116 \times 10^3$ [BTU/hr] (2672 W)
Inlet Reynolds Number	$Re_D = 3.764 \times 10^5$

The diverging nozzle wall temperatures revealed the same general trend as the previous two nozzle cases, as seen in Figure 45. That is, the wall experiences rapid cooling near the nozzle exit after a steady temperature increase throughout the majority of the length from the inlet. This cooling is likely due to, as in the prior cases, expansion and acceleration of the flow. In this case, however, the flow is not limited to a Mach number value of unity, but continues to expand and accelerate as it passes through the diverging portion of the channel.

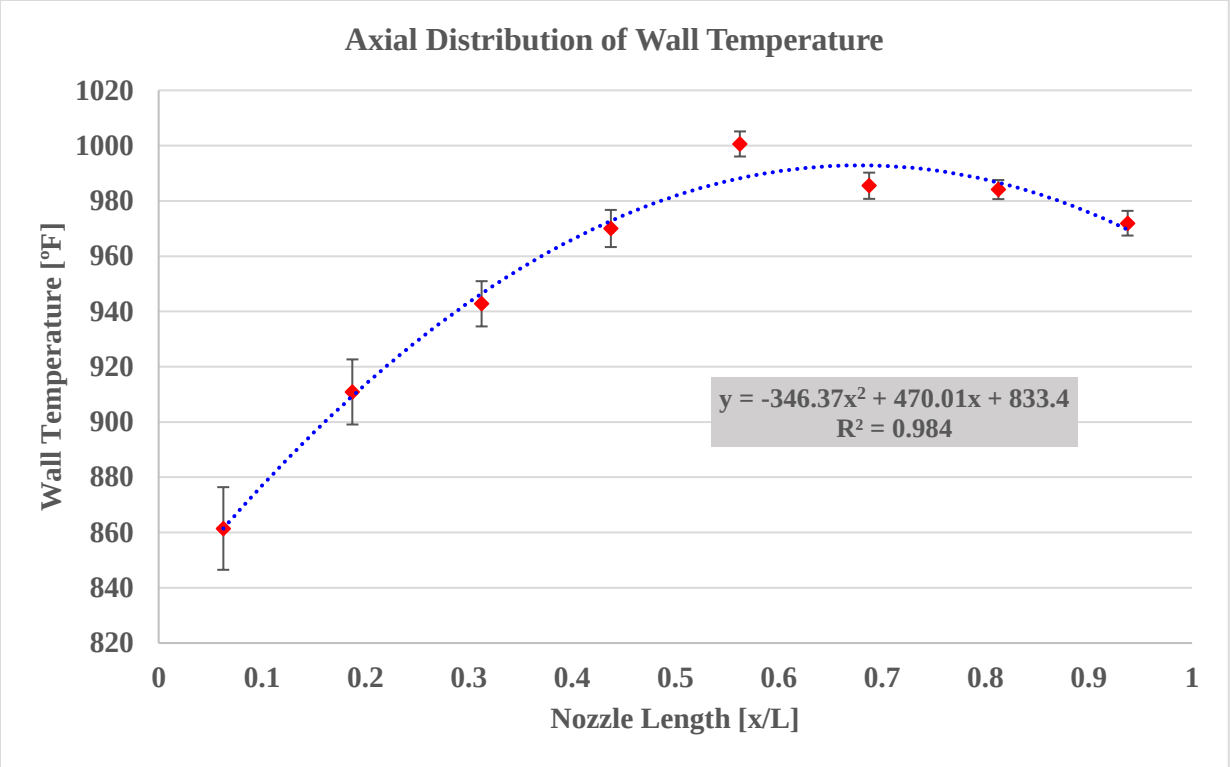

Figure 45: Diverging Nozzle Wall Temperature Distribution

The general distribution of static pressure (Figure 46) approximates that of the model predicted curve. However, unlike the previous cases, the experimental data follows a different trend in the latter, diverging half of the nozzle. The most likely reason for this difference is the constraint of the sonic point location in the model code. As discussed in earlier chapters, the sonic point was set at the nozzle throat in the diverging case, forcing the predicted result to conform to this condition. In reality, the sonic location may not be precisely at this location, but somewhere further downstream in the nozzle, as indicated in Chapter 10 of Reference [9]. As a reference, the diverging nozzle model was run with the same geometry and inlet settings, but with the sonic location set at the exit of the nozzle. This simulation assumes that the heat transfer and friction in the nozzle may actually cause it to choke as far as the exit plane. Comparison of the experimental pressure data to this exit-choking condition and the original throat-choking prediction support the inference that the nozzle is likely choking somwhere downstream of the

throat and before the nozzle exit. This is seen by the more rapid descent in pressure occurring later than the throat, yet the overall pressure data is well below the prediction of the exit-choking case. Based upon general compressible flow intuition, this lower pressure indicates the expectation that rapid acceleration of the flow is taking place in the diverging portion of the nozzle. As it currently stands, it may be clearly observed that the transition of the flow from subsonic to supersonic conditions is a realm of poor prediction on the part of the model.

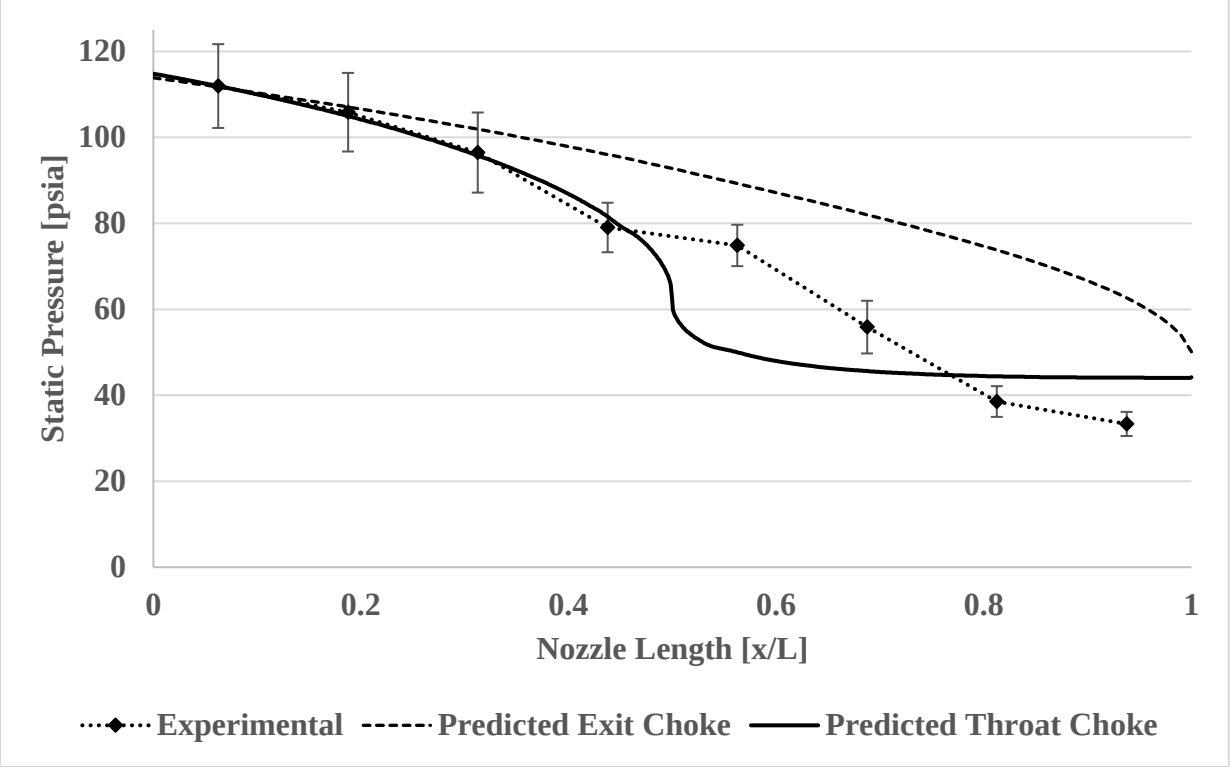

Figure 46: Diverging Nozzle Static Pressure Distribution

Once again, the stagnation temperature distribution followed a similar total trend as that predicted by the numerical model, as seen in Figure 47. However, the deviation in this case is much more significant, demonstrated by the significant over-prediction of temperature by the model. In the previous two nozzles, it is more legitimate to conclude that the difference between experimental and analytical values is primarily due to instrumentation error since the

experimental data of the Fanno-Rayleigh and converging cases demonstrated an inconsistent distribution, yet fell close to the predicted values. In this instance, however, the experimental values display a smooth trend that could represent a correct compressible nozzle case, but for a much lower than predicted heat transfer.

It may be noted that both model predictions are nearly the same for the exit-choking and throat-choking conditions. The author's best explanation for this is that the temperature increase in the throat-choking case is largely due to the high-velocity (kinetic energy) of the flow, while the exit-choking condition experiences more significant heat transfer to the flow due to greater transit time through the nozzle. Regardless of the assumed location of the sonic point, the model is clearly over-predicting flow temperatures for the diverging nozzle.

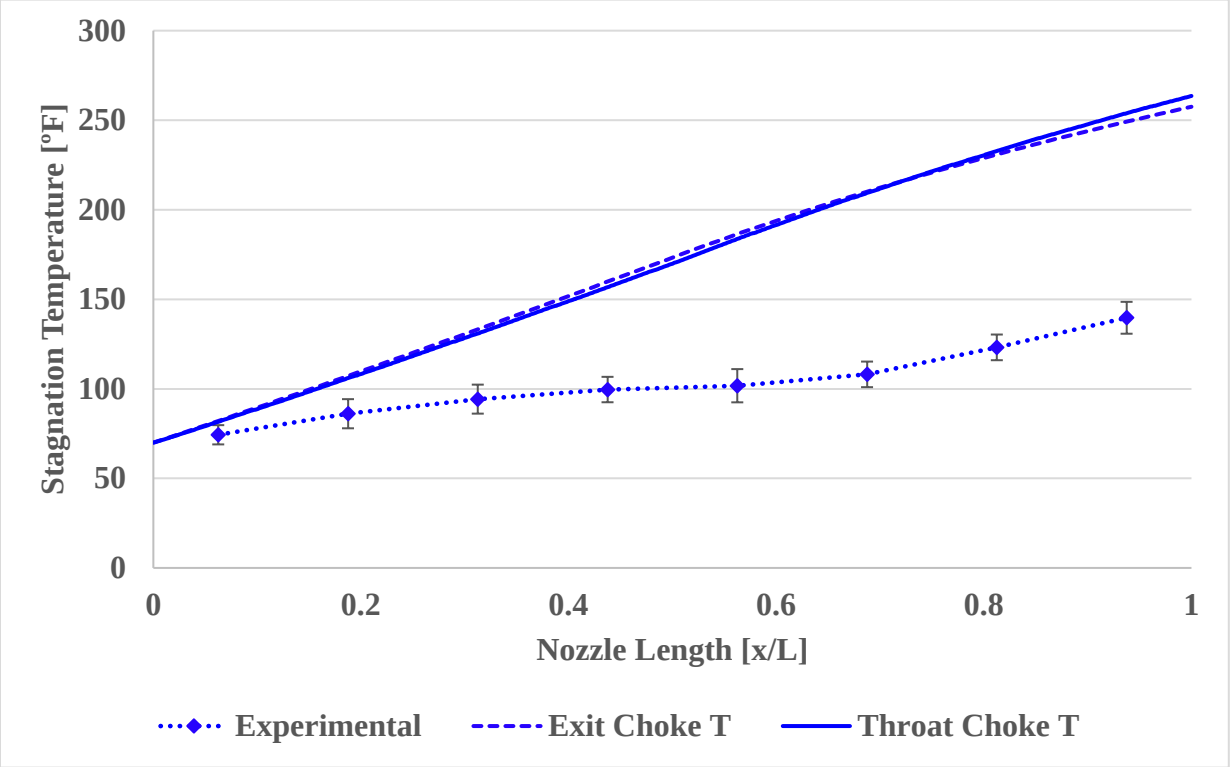

Figure 47: Diverging Nozzle Mean Flow Stagnation Temperature Distribution

Chapter 6. Conclusions and Future Development

6.1 Conclusions

Review of the present work provides several key observations from which major conclusions may be drawn. The bulk of these observations relate to the performance of the numerical model, and its ability to evaluate the various nozzle flows. However, an evaluation of the experimental methods employed, here, also lends significant deductions.

The first of these conclusions is from the observed agreement between NASA's GFSSP code and the developed model for evaluation of the design case. It was determined that, for the same set of nozzle conditions, the numerical model predicted nearly the same distribution of characteristics through the nozzle as the GFSSP code. In fact, the model developed, here, was even in better agreement with the analytical curves that were used to validate the performance of GFSSP. This concurrence with an externally validated code serves to advance the credibility of the numerical model.

A second major conclusion from this work is that the method of experimentation employed is not sufficient to validate the numerical model. If the model is assumed to be accurate for all nozzle cases, then the error may be fully credited to experimental error. However, if the experimental data is to be trusted, then it may be determined that the model code is in need of adjustment for some of the nozzle conditions. While the experimental data is on the same order of magnitude as the model prediction and exhibits some of the same general trends for each nozzle case, the overall distribution of characteristics is not in good agreement. In general, the model is more capable of predicting subsonic flow conditions, while more significant divergence occurs for the supersonic case.

Furthermore, the combined Fanno Rayleigh entropy curve serves as a promising tool for sonic prediction. To the author's knowledge, such demonstration of the combined effects of heat transfer and friction with the energy equation has not been done in readily available research. This presentation was beneficial in that it helps to build intuition regarding the behavior of combined frictional, diabatic flow. It also served to confirm its agreement with the location of the sonic point location and, in the diverging case, the transition to supersonic flow.

6.2 Future Development

It is the author's view that, although there are many areas that may be addressed in this work, three primary subjects merit further examination.

The first, and most significant, of these areas is the method of calculating the effects of friction and heat transfer in the numerical model. Limited resources were discovered that accounted for the compressibility of the fluid for which a heat transfer or friction coefficient had been developed. If this work were to be continued, it is the author's recommendation that a search should be performed for improved correlations for determination of these model constituents.

In addition to enhancing the heat transfer and frictional calculations, it is recommended that a method for predicting the sonic point location be included in the model code. As a simplification, the sonic point was set as an input to the numerical model. This was applied on the basis of gas dynamics theory, although the precise location may not actually take place at the specified location. This is more significant for the diverging nozzle, as the sonic point may not actually occur directly at the nozzle throat, but further down the channel toward the exit side. Such a method as described in Chapter 9 of Reference [9] may be applied to the diverging nozzle

case in this work. The exit set point for the Fanno-Rayleigh and converging nozzles is quite legitimate, since the flow is restricted from surpassing sonic flow.

Thirdly, it is the author's recommendation that additional research be performed on experimental methods for measuring the pressure and temperature of a high-velocity flow (Ex. Pitot-static, Hot-wire Anemometry, etc.). Much of the uncertainty in drawing conclusions from the experimental data arose from the challenge of instrumentation on this small of a scale. Though testing with additional, as well as adjusted, instrumentation, was not performed due to limited project schedules and resources, it is highly recommended, should this work be continued.

Overall, the model developed in this work serves as a suitable starting point for SCEPS injector analysis. Although there are a number of areas that warrant further investigation, this work is a baseline for future development of compressible nozzle flow modeling.

References

[1] Chan, S. H., et al. "Li− SF6 combustion in stored chemical energy propulsion systems." *Symposium (International) on Combustion*. Vol. 23. No. 1. Elsevier, 1991.

[2] Hughes, T. G., R. B. Smith, and D. H. Kiely. "Stored chemical energy propulsion system for underwater applications." *Journal of Energy* 7.2 (1983).

[3] Hills, R. "HAP/OTTO fuel application to torpedo engines." *18th Joint Propulsion Conference*. (1982): Web. 04 January 2016.

[4] Majumdar, Alok K., et al. "Generalized Fluid System Simulation Program (GFSSP)-Version 6." *51st AIAA/SAE/ASEE Joint Propulsion Conference*. (2015): Web. 20 January 2017.

[5] Bandyopadhyay, Alak, and Alok Majumdar. "Modeling of Compressible Flow with Friction and Heat Transfer using the Generalized Fluid System Simulation Program (GFSSP)." *Thermal Fluid Analysis Workshop*. Vol. 10 (2007): Web. 20 January 2017.

[6] Bandyopadhyay, Alak, Andre LeClair, and Ric Moore. “Generalized Fluid System Simulation Program (GFSSP) Version 6.” nasa.gov (2012): Web. 19 June 2017.

[7] Khunger, Ishaan. "Fanno Flow and Rayleigh Flow Calculations for Bleed Flow through a Variable Area By-Pass Duct of a Pulse Detonation Engine." (2015): Web. 20 June 2017.

[8] Hsieh, Wilbur Po-sam. "Combined fanno-line, rayleigh-line heat transfer and friction effects on steady one-dimensional gas flow in constant-area passages." (1968).

[9] Yunus, A. Cengel, and John M. Cimbala. "Fluid mechanics: fundamentals and applications." *International Edition, McGraw Hill Publication* (2006): 622.

[10] John, James E. Gas Dynamics. Upper Saddle River, New Jersey 07458: Pearson Prentice Hall, 2006.

[11] Shapiro, Ascher H. The dynamics and thermodynamics of compressible fluid flow. John Wiley & Sons, 1953.

[12] Chen, Ning Hsing. "An explicit equation for friction factor in pipe." Industrial & Engineering Chemistry Fundamentals 18.3 (1979): 296-297.

[13] Peiyi, Wu, and W. A. Little. "Measurement of friction factors for the flow of gases in very fine channels used for microminiature Joule-Thomson refrigerators." Cryogenics 23.5 (1983): 273-277.

[14] Back, L. H., P. F. Massier, and H. L. Gier. "Convective heat transfer in a convergent-divergent nozzle." International Journal of Heat and Mass Transfer 7.5 (1964): 549-568.

[15] Saunders, O. A., and P. H. Calder. Some experiments on the heat transfer from a gas flowing through a convergent-divergent nozzle. No. ARC-14539. AERONAUTICAL RESEARCH COUNCIL LONDON (UNITED KINGDOM), 1952.

[16] Colebrook, C. F., and C. M. White. "Experiments with fluid friction in roughened pipes." *Proceedings of the royal society of london. series a, mathematical and Physical sciences* (1937): 367-381.

[17] Swanee, P. K., and Akalank K. Jain. "Explicit equations for pipeflow problems." *Journal of the hydraulics division* 102.5 (1976).

[18] Haaland, Skjalg E. "Simple and explicit formulas for the friction factor in turbulent pipe flow." *Journal of Fluids Engineering* 105.1 (1983): 89-90.

[19] Anderson, John D. "Modern Compressible Flow with Historical Perspective." (2003).

[20] Achenbach, Elmar. "Heat transfer from spheres up to Re= 6 x 106." *Proceedings of the Sixth International Heat Transfer Conference*. Vol. 5. 1978.

[21] Moffat, Robert J. “Describing the uncertainties in experimental results.” *Experimental thermal and fluid science*, 1.1 (1988): 3-17.

Appendices

Appendix A: Derivation of Governing Equation

Flow with Friction, Heat Addition, Area Change, Mass Flow, and Drag Force [Shapiro]

$$\frac{dM^2}{M^2} = -\frac{2\left(1+\frac{\gamma-1}{2}M^2\right)}{(1-M^2)}\frac{dA}{A} + \frac{(1+\gamma M^2)\left(1+\frac{\gamma-1}{2}M^2\right)}{1-M^2}\frac{dT_0}{T_0}$$
$$+\frac{(\gamma M^2)\left(1+\frac{\gamma-1}{2}M^2\right)}{1-M^2}\left(4f\frac{dx}{D}+\frac{dX}{\frac{1}{2}\gamma pAM^2}-2y\frac{d\dot{m}}{\dot{m}}\right)$$
$$+\frac{2(1+\gamma M^2)\left(1+\frac{\gamma-1}{2}M^2\right)}{1-M^2}\frac{d\dot{m}}{\dot{m}}$$

$$\frac{dM^2}{M^2} = -\frac{2\left(1+\frac{\gamma-1}{2}M^2\right)}{(1-M^2)}\frac{dA}{A} + \frac{(1+\gamma M^2)\left(1+\frac{\gamma-1}{2}M^2\right)}{1-M^2}\frac{dT_0}{T_0}$$
$$+\frac{(\gamma M^2)\left(1+\frac{\gamma-1}{2}M^2\right)}{1-M^2}\left(4f\frac{dx}{D}+\frac{\cancel{dX}}{\cancel{\frac{1}{2}\gamma pAM^2}}-2y\frac{d\dot{m}}{\dot{m}}\right)$$
$$+\frac{2(1+\gamma M^2)\left(1+\frac{\gamma-1}{2}M^2\right)}{1-M^2}\frac{d\dot{m}}{\dot{m}}$$

$$\frac{dM^2}{M^2} = -\frac{2\left(1+\frac{\gamma-1}{2}M^2\right)}{(1-M^2)}\frac{dA}{A} + \frac{(1+\gamma M^2)\left(1+\frac{\gamma-1}{2}M^2\right)}{1-M^2}\frac{dT_0}{T_0}$$
$$+\frac{(\gamma M^2)\left(1+\frac{\gamma-1}{2}M^2\right)}{1-M^2}\left(4f\frac{dx}{D}+\frac{\cancel{dX}}{\cancel{\frac{1}{2}}\gamma pA\cancel{M^2}}-\cancel{2y\frac{d\dot{m}}{\dot{m}}}\right)$$
$$+\frac{2(1+\gamma M^2)\left(1+\frac{\gamma-1}{2}M^2\right)}{1-M^2}\cancel{\frac{d\dot{m}}{\dot{m}}}$$

$$\frac{dM^2}{M^2} = -\frac{2\left(1+\frac{\gamma-1}{2}M^2\right)}{(1-M^2)}\frac{dA}{A} + \frac{(1+\gamma M^2)\left(1+\frac{\gamma-1}{2}M^2\right)}{1-M^2}\frac{dT_0}{T_0}$$

$$+\frac{(\gamma M^2)\left(1+\frac{\gamma-1}{2}M^2\right)}{1-M^2}\left(4f\frac{dx}{D}\right)$$

$$\frac{dM^2}{M^2} = \frac{2\left(1+\frac{\gamma-1}{2}M^2\right)}{(1-M^2)}\left[-\frac{dA}{A} + (1+\gamma M^2)\frac{dT_0}{2T_0} + \gamma M^2\left(2f\frac{dx}{D}\right)\right]$$

$$\frac{\cancel{2}M dM}{M^{\cancel{2}}} = \frac{\cancel{2}\left(1+\frac{\gamma-1}{2}M^2\right)}{(1-M^2)}\left[-\frac{dA}{A} + (1+\gamma M^2)\frac{dT_0}{2T_0} + \gamma M^2\left(2f\frac{dx}{D}\right)\right]$$

$$\frac{dM}{dx} = \frac{M\left(1+\frac{\gamma-1}{2}M^2\right)}{(1-M^2)}\left[-\frac{1}{A}\frac{dA}{dx} + \frac{(1+\gamma M^2)}{2T_0}\frac{dT_0}{dx} + 2\gamma M^2\frac{f}{D}\right]$$

$$f = 4f_{Darcy}$$

$$f_{Darcy} = \frac{1}{4}f$$

$$\boxed{\frac{dM}{dx} = \frac{M\left(1+\frac{\gamma-1}{2}M^2\right)}{(1-M^2)}\left[-\frac{1}{A}\frac{dA}{dx} + \frac{(1+\gamma M^2)}{2T_0}\frac{dT_0}{dx} + \frac{1}{2}\gamma M^2\frac{f_{Darcy}}{D}\right]}$$

Appendix B: General Testing Procedure

Procedure	Description	Initial	Date
1.0	**Pre-Test Setup**		
1.1	Assemble test apparatus, including nitrogen and hot water supply lines. Ensure that supply valves are closed.	_____	_____
1.2	Verify that 240V power supplies (x2) are shut down. Connect power cords to Port 1 and Port 2 on receptacle plate located at the rear side of test cart.	_____	_____
1.3	Check injector inlet valve and confirm that it is closed.	_____	_____
1.4	Slowly open nitrogen supply valve and regulate system pressure to 200 psi.	_____	_____
1.5	Check all nitrogen line connections between supply tanks and inlet solenoid to ensure that there are no significant leaks.	_____	_____
1.6	Briefly (5 seconds) open inlet valve to purge line of air and fill with nitrogen. Fully close valve once line is purged.	_____	_____
1.7	Turn on hot water supply valve for the gas heat exchanger and run until system is full. Ensure that heat exchanger is purged of air and that no leaks are present.	_____	_____
1.8	Calibrate nozzle pressure transducers to atmospheric pressure (14.2 psi).	_____	_____
1.9	Calibrate thermocouple data system to current room temperature.	_____	_____
2.0	**Test Procedure**		
2.1	Turn heat exchanger hot water supply valve to full-on condition.	_____	_____
2.2	Open inlet valve to 25% of steady-state run flow rate to begin cooling injector test section.	_____	_____
2.3	Command startup of 240V cartridge heaters. Monitor heater temperature to ensure overheating does not occur.	_____	_____
2.4	When heater voltage reaches 90% of run value, fully open inlet valve.	_____	_____

2.5	Initiate data collection of static pressures (transducers) and wall and mean flow temperatures (thermocouples).	_____	_____
2.6	Collect data for roughly one minute, or until steady-state temperatures are occurring along test section.	_____	_____
2.7	Command heater voltage reduction. When voltage reaches zero (0), Turn off 240V power supplies.	_____	_____
2.8	Close inlet valve.	_____	_____
2.9	Shut off nitrogen supply valve.	_____	_____
2.10	Turn off hot water supply valve.		
2.11	Ensure that system equilibrates and is safely shut down.	_____	_____
TEST END		_____	_____

Appendix C: Base Fanno-Rayleigh Model Code Structure

```
%%% SCEPS Injector Model: Fanno-Rayleigh Design Case
%%% Michael E. Crouse, Jr.
%%% 17 March 2017

clear; % clear MATLAB workspace variables
clc; % clear MATLAB command window

%%% Problem Setup

% Iteration, limiter, and convergence criteria
j_max = 1000; % Maximum number of iterations allowed.  Model should converge
prior to reaching this limit
stepchange_M = .02; % Maximum velocity magnitude step change per
iteration.  Limits model's high nonlinearity near sonic point
converge_criteria = .0001; % Convergence criteria.  Maximum velocity change
between current and prior iteration must reduce to this value for model
convergence

% Discretize injector along axial length
i_max = 100; % Number of nodes for discretization [unitless]

% Define physical characteristics
L_in = 8; % Injector length [in]
L = L_in * 0.0254; % Injector length [m]
x = linspace(0,L,i_max); % Define position at each node (linear spacing) [m]
dx = x(2)-x(1); % Axial stepchange, uniform along length
D_in = 0.25; % Injector diameter [in]
Dm = D_in * 0.0254; % Injector diameter [m]

% Create diameter and Area arrays. For later use with plotting.
for i=1:i_max
D(i) = Dm;
A(i)= pi.*((D(i)/2).^2); % injector flow area [m^2]
end

% Define inlet stagnation temperature
To_t_F(1:j_max,1,1) = 40; % Inlet stagnation temperature [degF]
To_t(1:j_max,1,:) = (To_t_F+459.67)*(5/9); % Inlet stagnation temperature [K]
To(1:j_max,1) = To_t(1:j_max,1); % Adjust array for current runtime. Only one
runtime is employed in this code.

% Define inlet stagnation pressure
Po_t_psi(1:j_max,1,1) = 150; % Inlet stagnation pressure [psia]
Po_t(1:j_max,1,:) = Po_t_psi * 6.895; % Inlet stagnation pressure [kPa]
Po(1:j_max,1) = Po_t(1:j_max,1); % Adjust array for current runtime. Only one
runtime is employed in this code.

% Define inlet mass flow
% **Only used for inital guess - subsequent values are calculated using flow
properties
mdot_data_t_lbhr(1) = 836.41 / 4; % Gas mass flow rate[lb/hr]
mdot_data = mdot_data_t_lbhr * .000126; % Gas mass flow rate [kg/s]
```

```
% Prescribe wall heat flux
%q_flux(1:i_max) = 567827; %[W/m^2]

% Define surface roughness along injector wall
Rgh(1:i_max) = 63e-6;

% Define Initial Guesses for First Iteration
% Guess mach number distribution
M(1:i_max) = linspace(.45,1,i_max); % Mach number array [unitless]

% Guess static temperature distribution
T(1:i_max) = linspace(250,800,i_max); % Static temperature array [K]

% Guess static pressure distribution
P(1:i_max) = linspace(700,350,i_max); % Static pressure array [kPa]

% Step through each node to define properties based upon already defined T
and P guesses
i=1;
while i <= i_max
    cp(i) = refpropm('C','T',T(i),'P',P(i),'nitrogen'); % Cp [J/(kg*K)]
    cv(i) = refpropm('O','T',T(i),'P',P(i),'nitrogen'); % Cv [J/(kg*K)]
    k(i) = cp(i)/cv(i); % Ratio of specific heats [unitless]
    Dens(i) = refpropm('D','T',T(i),'P',P(i),'nitrogen'); % Density [kg/m^3]
    C(i) = refpropm('A','T',T(i),'P',P(i),'nitrogen'); % Speed of sound [m/s]
    V(i) = M(i)*C(i); % Velocity [m/s]
    mdot(i) = mdot_data; % Mass flow rate [kg/sec]
    visc_dyn(i) = refpropm('V','T',T(i),'P',P(i),'nitrogen'); % Dynamic
viscosity
    Re(i) = (Dens(i)*V(i)*D(i))/visc_dyn(i); % Reynolds number [unitless]
    Condk(i) = refpropm('L','T',T(i),'P',P(i),'nitrogen');% Gas conductive
coefficient [W/(m*K)].
    Prandtl(i) = refpropm('^','T',T(i),'P',P(i),'nitrogen'); %Prandtl Number
    h(i) = ((0.023*(Prandtl(i)^0.4)*(Re(i)^0.8))*Condk(i))/D(i); % Gas
convective coefficient [w/(m^2*K)].
    T_wall(i) = -174.34*x(i)^2 + 260.11*x(i) + 714.93; % Prescribed wall
temperature. Roughly the same distribution as experimental data.
    convective_deltaT(i) = T_wall(i)-T(i); % Temperature change between wall
and gas for later convective heat tranfer calculation [K].
    i=i+1;
end

%%% Run Iterations
j=2; % Start at iteration 2, where iteration 1 was the initial guesses.
while j < j_max

    % Determine inlet static conditions
    T(j-1,1) = (1/(1+(((k(j-1,1)-1)/2)*M(j-1,1)^2)))*To(j-1,1); % Inlet
static T [K].  Determined from inlet stagnation T and inlet mach number from
previous iteration. See any compressible flows textbook for derivation.
    P(j-1,1) = ((1/(1+(((k(j-1,1)-1)/2)*M(j-1,1)^2)))^(k(j-1,1)/(k(j-1,1)-
1)))*Po(j-1,1); % Inlet static P [kPa]. Determined from inlet stagnation P
and inlet mach number from previous iteration. See any compressible flows
textbook for derivation.
```

```
    % Step through each non-inlet node
    i=1;
    while i <= i_max;

        Ttung_avg(j) = -196.4*log(mdot(j-1,i_max))-250.41;

        % Rayleigh Component
        if i < i_max;
            h(j-1,i) = ((0.023*(Prandtl(j-1,i)^0.4)*(Re(j-1,i)^0.8))*Condk(j-
1,i))/D(i); % Gas convective coefficient [w/(m^2*K)].
            %q(j-1,i) = q_flux(i)*(3.1415*D(i)*(x(i+1)-x(i))); % Convective
heat transfer from injector wall to gas for current element [J/s]
            q(j-1,i) = h(j-1,i)*(3.1415*D(i)*(x(i+1)-
x(i)))*convective_deltaT(j-1,i); % Convective heat transfer from injector
wall to gas for current element [J/s]
            dTodx(j-1,i) = q(j-1,i)/(mdot(j-1,i)*cp(j-1,i)*(x(i+1)-x(i))); %
Change in gas stagnation temperature across current element due to convective
heating [K]
            To(j-1,i+1) = To(j-1,i) + (dTodx(j-1,i)*(x(i+1)-x(i))); % New gas
stagnation temperature at element end node [K]
        end

        % Calculate static T, static P, and stagnation P for each non-inlet
node
        if i > 1;
            T(j-1,i) = ((To(j-1,i)/To(j-1,1))*((1+((k(j-1,i)-1)/2)*(M(j-
1,1)^2))/((1+((k(j-1,i)-1)/2)*(M(j-1,i)^2)))))*T(j-1,1); % Nodal static T
[K].  Derivation from "Modeling of Compressible Flow with Frication and Heat
Transfer", Thermal Fluid Analysis Workshop, Bandyopadhyay, 2007
            P(j-1,i) = (((M(j-1,1))/(M(j-1,i)))*sqrt(T(j-1,i)/T(j-1,1)))*P(j-
1,1); % Nodal static P [kPa].  Derivation from "Modeling of Compressible Flow
with Frication and Heat Transfer", Thermal Fluid Analysis Workshop,
Bandyopadhyay, 2007
            Po(j-1,i) = P(j-1,i) / ((1/(1+((k(j-1,i)-1)/2)*(M(j-
1,1)^2)))^(k(j-1,i)/(k(j-1,i)-1))); % Nodal stagnation P [kPa]. See any
compressible flows textbook for derivation.
        end

        % Use static T and P to determine fluid properties for current node
        cp(j,i) = refpropm('C','T',T(j-1,i),'P',P(j-1,i),'nitrogen'); % Cp
[J/(kg*K)]
        cv(j,i) = refpropm('O','T',T(j-1,i),'P',P(j-1,i),'nitrogen'); % Cv
[J/(kg*K)]
        Dens(j,i) = refpropm('D','T',T(j-1,i),'P',P(j-1,i),'nitrogen'); %
Density [kg/m^3]
        C(j,i) = refpropm('A','T',T(j-1,i),'P',P(j-1,i),'nitrogen'); % Speed
of sound [m/s]
        k(j,i) = cp(j,i)/cv(j,i); % Heat capacity ratio [unitless]
        Condk(j,i) = refpropm('L','T',T(j-1,i),'P',P(j-1,i),'nitrogen');% Gas
conductive coefficient [W/(m*K)].
        Prandtl(j,i) = refpropm('^','T',T(i),'P',P(i),'nitrogen'); %Prandtl
Number
        h(j,i) = ((0.023*(Prandtl(j-1,i)^0.4)*(Re(j-1,i)^0.8))*Condk(j-
1,i))/D(i); % Gas convective coefficient [w/(m^2*K)].
```

```
        T_wall(j,i) = -174.34*x(i)^2 + 260.11*x(i) + 714.93;  % Prescribed
wall temperature. Roughly the same distribution as experimental data.
        convective_deltaT(j,i) = T_wall(j,i)-T(j-1,i); % deltaT between wall
and gas for later convective heat tranfer calculation [K].
        visc_dyn(j,i) = refpropm('V','T',T(j-1,i),'P',P(j-1,i),'nitrogen');
        V(j,i) = M(j-1,i)*C(j,i); % Velocity [m/s]
        mdot(j,i) = Dens(j,i) * V(j,i) * A(i); % Mass flow rate [kg/sec]
        Re(j,i) = (Dens(j-1,i)*V(j-1,i)*D(i))/visc_dyn(j,i); % Reynolds
number [unitless]

        % Fanno Component
        if Re(j,i) <= 2320; % Pure laminar flow
            f(j,i) = 64/Re(j,i); % Darcy friction factor for laminar flow in
circular pipes
        else
            f_swamee(j,i) =
0.25*(log10(Rgh(i)/(3.7*D(i))+5.74/(Re(j,i)^0.9)))^(-2); % Swamee-Jain
approximation of Colebrook equation for darcy friction factor
            f_haaland(j,i) = (-
1.8*log10((((Rgh(i)/D(i))/3.7)^1.11)+6.9/Re(j,i)))^(-2); % Haaland
approximation of Colebrook equation for darcy friction factor
            if abs(f_swamee(j,i)-f_haaland(j,i))/f_haaland(j,i) >= .05 %
Check that Swamme-Jain and Haaland approximations are within 5% of one
another.  if not an error is thrown
                disp('ERROR: Darcy Friction Factor Calculation
Problem.  Check Results Carefully.')
            end
            f(j,i) = (f_swamee(j,i)+f_haaland(j,i))/2; % Average Swamee-Jain
and Haaland darcy friction factor values
        end

        i=i+1; % Progress to next node (toward outlet side)
    end

    % Calculate new dMdx and M values at each node
    M(j,i_max) = 1; % Boundary condition, choked flow at exit.
    i=i_max-1;
    while i >= 1 % Step through each non-outlet node, starting at outlet side
and moving to inlet side
        % Calculate contribution of friction and heat transfer to velocity
change
        dMdx_Term_Fanno(j,i) = k(j,i)*(M(j-1,i)^2)*(f(j,i)/(2*D(i))); % Fanno
(friction) contribution to velocity increase
        dMdx_Term_Rayleigh(j,i) = ((1+k(j,i)*(M(j-1,i)^2))/(2*To(j-
1,i)))*dTodx(j-1,i); % Rayleigh (heat transfer) contribution to velocity
increase
        dMdx_Term_Multiplier(j,i) = (M(j-1,i)*(1+((k(j,i)-1)/2)*(M(j-
1,i)^2)))/(1-M(j-1,i)^2); % Equation multiplier based on mach number from
previous iteration
        dMdx(j,i) =
dMdx_Term_Multiplier(j,i)*(dMdx_Term_Fanno(j,i)+dMdx_Term_Rayleigh(j,i)); %
Rate of change in velocity over current element
        deltaM(j,i) = (dMdx(j,i)*(x(i+1)-x(i))); % Total change in velocity
over current element
        M(j,i) = M(j,i+1) - (dMdx(j,i)*(x(i+1)-x(i))); % Velocity at current
element end node (inlet side)
```

```
        diffM(j,i) = M(j,i)-M(j-1,i); % Change in velocity for current node
from previous iteration

        % Determine if nodal velocity change is larger than prescribed max
step change magnitude.  If so, limit new nodal velocity to only the maximum
step change
        if abs(diffM(j,i)) >= stepchange_M
            if M(j,i) <= M(j-1,i)
                M(j,i) = M(j-1,i) - stepchange_M;
            else
                M(j,i) = M(j-1,i) + stepchange_M;
            end
        end

        i=i-1; % Progress to next node (toward inlet side)
    end

    % Determine convergence
    if max(abs(diffM(j,:))) <= 5*stepchange_M; % Check the max velocity
change for any node in the current iteration.  If the max nodal velocity
change was less than 5 times the maximum step change, reduce the maximum step
change to be 2/3 its current vlaue.
        stepchange_M = stepchange_M * (15/16);
        if max(abs(diffM(j,:))) <= converge_criteria % If the velocity change
is less than the specified convergence value, the model is converged and
iteration can be ended
            disp('Model Converged This Iteration.');
            z1=j;
            j_max = j; % Exit iteration by setting max iteration to current
iteration number
        end
    end

    % output convergence information to user
    userOutputLine1 = sprintf('Iteration For Current Runtime: %d',j); %
Display current iteration
    disp(userOutputLine1)
    userOutputLine2 = sprintf('Convergence Value:
%10.8f',max(abs(diffM(j,:)))); % Display max nodal velocity change between
iterations
    disp(userOutputLine2)
    userOutputLine3 = sprintf('Convergence Criteria:
%10.8f',converge_criteria); % Display max nodal velocity change allowed
before convergence declared
    disp(userOutputLine3)
    disp(' ')

    j=j+1; % Progress to next iteration
end
```